TKK Dissertations 245
Espoo 2010

FINITE ELEMENT ANALYSIS OF EDDY CURRENT LOSSES IN STEEL LAMINATIONS OF INVERTER-FED ELECTRICAL MACHINES

Doctoral Dissertation

Jenni Pippuri

Aalto University
School of Science and Technology
Faculty of Electronics, Communications and Automation
Department of Electrical Engineering

TKK Dissertations 245
Espoo 2010

FINITE ELEMENT ANALYSIS OF EDDY CURRENT LOSSES IN STEEL LAMINATIONS OF INVERTER-FED ELECTRICAL MACHINES

Doctoral Dissertation

Jenni Pippuri

Doctoral dissertation for the degree of Doctor of Science in Technology to be presented with due permission of the Faculty of Electronics, Communications and Automation for public examination and debate in Auditorium S4 at the Aalto University School of Science and Technology (Espoo, Finland) on the 5th of November 2010 at 12 noon.

Aalto University
School of Science and Technology
Faculty of Electronics, Communications and Automation
Department of Electrical Engineering

Aalto-yliopisto
Teknillinen korkeakoulu
Elektroniikan, tietoliikenteen ja automaation tiedekunta
Sähkötekniikan laitos

Distribution:
Aalto University
School of Science and Technology
Faculty of Electronics, Communications and Automation
Department of Electrical Engineering
P.O. Box 13000 (Otakaari 5)
FI - 00076 Aalto
FINLAND
URL: http://sahkotekniikka.tkk.fi/en/
Tel. +358-9-470 22393
Fax +358-9-470 22991
E-mail: jenni.pippuri@tkk.fi

© 2010 Jenni Pippuri

ISBN 978-952-60-3425-6
ISBN 978-952-60-3426-3 (PDF)
ISSN 1795-2239
ISSN 1795-4584 (PDF)
URL: http://lib.tkk.fi/Diss/2010/isbn9789526034263/

TKK-DISS-2822

Multiprint Oy
Espoo 2010

Aalto University

ABSTRACT OF DOCTORAL DISSERTATION	AALTO UNIVERSITY SCHOOL OF SCIENCE AND TECHNOLOGY P.O. BOX 11000, FI-00076 AALTO http://www.aalto.fi

Author Jenni Pippuri

Name of the dissertation
Finite element analysis of eddy current losses in steel laminations of inverter-fed electrical machines

Manuscript submitted	21.6.2010	Manuscript revised	1.10.2010
Date of the defense	5.11.2010		
☒ Monograph		☐ Article dissertation (summary + original articles)	

Faculty	Faculty of Electronics, Communications and Automation
Department	Department of Electrical Engineering
Field of research	Electromechanics
Opponent(s)	Professor João Pedro A. Bastos
Supervisor	Professor Antero Arkkio
Instructor	Docent Anouar Belahcen

Abstract

This thesis investigates the eddy currents and regarding losses in electrical steel sheets. For the purpose, two methods of numerical analysis of electromagnetic fields are developed. Both of those are based on the two-dimensional (2-D) finite element computation of the fields. Since the eddy currents of the sheets are, by definition, excluded from the 2-D formulation they need to be included separately. Within this work, the goal is achieved by modeling the eddy currents via a one-dimensional (1-D) penetration equation in association with the 2-D analysis. Formulations for both, general time variation and sinusoidal time variation are shown.

The coupling of the 2-D and 1-D models is investigated from several perspectives. For representing the 1-D eddy current solution within the time-discretized analysis two approaches are considered. Numerous simulations carried out reveal that inappropriate coupling might not affect the losses to be obtained but other electromagnetic quantities such as input power or power factor. A proper coupling method that accords with the computation results is proposed. The combining of those two field formulations is discussed in the case of the time-harmonic approach as well, for which the concept of complex reluctivity is employed.

The second objective of the work is to study in detail the losses in rotating electrical machines fed by a frequency converter. The higher harmonics associated with the frequency-converter supply are known to increase to losses in comparison with a sinusoidal voltage supply. According to the simulations, (i) the eddy current losses in the rotor sheets are the most sensitive to the distorted input voltage waveforms and (ii) coincidently can be the most reduced by choosing the switching frequency of the frequency converter suitably.

The measurements carried out on the test machine and comparative studies of those and the simulation results verify the methods proposed.

Keywords eddy currents, numerical field analysis, finite element method, electrical machines, losses

ISBN (printed)	978-952-60-3425-6	ISSN (printed)	1795-2239
ISBN (pdf)	978-952-60-3426-3	ISSN (pdf)	1795-4584
Language	English	Number of pages	136
Publisher	Department of Electrical Engineering, Aalto University		
Print distribution	Department of Electrical Engineering, Aalto University		

☒ The dissertation can be read at http://lib.tkk.fi/Diss/2010/isbn9789526034263/

Aalto-yliopisto

VÄITÖSKIRJAN TIIVISTELMÄ	AALTO-YLIOPISTO TEKNILLINEN KORKEAKOULU PL 11000, 00076 AALTO http://www.aalto.fi

Tekijä Jenni Pippuri

Väitöskirjan nimi
Sähkölevyjen pyörrevirtojen numeerinen kenttälaskenta taajuusmuuttajalla syötetyssä sähkökoneessa

Käsikirjoituksen päivämäärä 21.6.2010	Korjatun käsikirjoituksen päivämäärä 1.10.2010
Väitöstilaisuuden ajankohta 5.11.2010	
☒ Monografia	☐ Yhdistelmäväitöskirja (yhteenveto + erillisartikkelit)

Tiedekunta	Elektroniikan, tietoliikenteen ja automaation tiedekunta
Laitos	Sähkötekniikan laitos
Tutkimusala	Sähkömekaniikka
Vastaväittäjä(t)	Professori João Pedro A. Bastos
Työn valvoja	Professori Antero Arkkio
Työn ohjaaja	Dosentti Anouar Belahcen

Tiivistelmä

Tässä työssä tutkitaan sähkölevyissä syntyviä pyörrevirtoja ja niistä aiheutuvia häviöitä. Tutkimuksen aikana on kehitetty kaksi numeerista kenttälaskentamenetelmää, jotka perustuvat kentän kaksiulotteisuusapproksimaatiolle. Tämän tyyppiset menetelmät eivät, määritelmänsä mukaisesti, ota huomioon sähkölevyjen pyörrevirtoja. Tässä työssä ne on sisällytetty kaksiulotteiseen (2-D) numeeriseen analyysiin yksiulotteisen (1-D) sähkölevyssä erikseen suoritettavan kenttäratkaisun keinoin. Menetelmät vapaasti aikariippuvien sekä ajan suhteen sinimuotoisesti vaihtelevien kenttien tarkasteluun esitetään.

Sähkölevyjen pyörrevirtojen 1-D ratkaisun soveltamista 2-D yhtälöissä tutkitaan monista eri näkökulmista. Vapaasti aikariippuvien kenttien tapauksessa tähän tarkoitukseen esitetään kahta menetelmää. Suoritetut simuloinnit osoittavat, että mallien kytkennän onnistuminen tai sen tarkkuus ei välttämättä vaikuta häviöihin, vaan muihin sähkömagneettisiin suureisiin kuten tehokertoimeen. Tutkimuksen tuloksena ehdotetaan optimaalista menetelmää 2-D ja 1-D ratkaisujen kytkentään. Ajasta sinimuotoisesti riippuvien kenttien tapauksessa sähkölevyjen pyörrevirrat esitetään 2-D yhtälöissä kompleksista reluktiivisuutta hyödyntäen.

Työn toinen tavoite on tutkia taajuusmuuttajalla syötetyssä sähkökoneessa syntyviä häviöitä työssä kehitettyjä menetelmiä soveltaen. Testikoneella eri toimintatilanteissa suoritetut simuloinnit osoittavat, että (i) sähkölevyissä syntyvistä häviöistä taajuusmuuttajan yliaallot vaikuttavat eniten roottoripuolen pyörrevirtahäviöihin ja että (ii) siitä syystä niihin voidaan myös vaikuttaa eniten taajuusmuuttajan kytkentätaajuutta muuttamalla.

Testikoneella suoritetut mittaukset ja saadut tulokset todentavat työssä kehitettyjen mallien käyttökelpoisuuden sähkökoneen monissa todellisissa käyttötilanteissa.

Asiasanat pyörrevirrat, numeerinen kenttälaskenta, elementtimenetelmä, sähkökone, häviöt

ISBN (painettu)	978-952-60-3425-6	ISSN (painettu)	1795-2239
ISBN (pdf)	978-952-60-3426-3	ISSN (pdf)	1795-4584
Kieli	Englanti	Sivumäärä	136

Julkaisija Sähkötekniikan laitos, Aalto-yliopisto

Painetun väitöskirjan jakelu Sähkötekniikan laitos, Aalto-yliopisto

☒ Luettavissa verkossa osoitteessa http://lib.tkk.fi/Diss/2010/isbn9789526034263/

Preface

This research was conducted at the Aalto University School of Science and Technology, at the Department of Electrical Engineering (formerly the Helsinki University of Technology, the Laboratory of Electromechanics). The experimental part of the work was carried out utilizing the equipment and the machine hall of the department and the facilities of the Faculty of Engineering and Architecture. When it comes to the numerical analyses performed during the course of the research, it must be stated that the computational resources and the expertise offered by the IT Center for Science Ltd (CSC) have proven to be incredibly valuable. The work was financed by the National Technology Agency of Finland (Tekes), ABB Oy, the Academy of Finland, and the Graduate School, Faculty of Electronics, Communications and Automation. I gratefully acknowledge all these parties as well as the financial support granted by Emil Aaltosen säätiö and Tekniikan edistämissäätiö (TES).

Several people were involved in this thesis project. First, I am very indebted to my supervisor Prof. Antero Arkkio and my instructor Docent Anouar Belahcen for the guidance and expertise that they provided during the years. Special thanks go for the head of the department Asko Niemenmaa for hiring me in the first place in 2002 as a summer employer. I would also like to express my gratitude to the other members of the team of electromechanics. Thank you all for the nice time together. The kindness and support of Mr. Ari Haavisto, Dr. Jarmo Perho, Mrs. Marika Schröder, and my long-time office mate Dr. Mohammad Jahirul Islam are much valued. The pep talks of Mr. Anssi Sinervo, particularly during the writing stage of the thesis, will neither be forgotten. I am also indebted to Mr. Jari Pekola, Mr. Jukka Järvinen, and Mr. Tommi Ryyppö for their valuable advice and co-operation.

Finally, I wish to gratefully acknowledge Prof. Carlo Ragusa and Prof. Katsumi Yamazaki for acting as the pre-examiners of the thesis and for providing constructive comments and criticism. For the language revision, I am indebted to Mr. Simon Gill.

I consider myself very lucky and privileged to have such an amazing mum, dad, sister, and friends. I owe you a great dept and wish to thank you all from the bottom of my heart. Particularly, I wish to express my deepest gratitude to my friend and former colleague Dr. Anna-Kaisa Repo. Her friendship and professional expertise have been invaluable for me during these years. Last but most certainly not least, I wish to address a few words to my beloved Mikko; I could not have made it without you.

Baden, Switzerland, October 2010

Jenni Pippuri

Contents

Symbols and definitions

Vector and matrix quantities are represented in ***bold, italic***, scalar quantities are in *italic*, and complex-valued quantities are *underlined, italic*.

Symbols

a	magnetic vector potential in 1-D
A	magnetic vector potential in 2-D
b	magnetic flux density in 1-D, material parameter related to texture and grain size of material
B	magnetic flux density in 2-D
C	circuit matrix
$\boldsymbol{e}$	unit vector
E	electric field strength in 2-D, vector related to eddy current modeling of steel sheets
f	frequency
G	circuit matrix
h	magnetic field strength in 1-D
H	magnetic field strength in 2-D, circuit matrix
i	current
j	current density in 1-D
J	current density in 2-D, moment of inertia
K	stator-winding connection matrix
l	length
L	inductance
m	number of phases in stator winding
M	magnetization
n	1-D shape function
N	2-D shape function, number of turns
n_f	number of free nodes in 1-D finite element mesh
N_f	number of free nodes in 2-D finite element mesh
n_n	number of nodes in 1-D finite element mesh
N_n	number of nodes in 2-D finite element mesh
N_s	number of symmetry sectors
p	Jacobian in 1-D
P	Jacobian in 2-D, power
Q_b	number of rotor bars in solution region
r	radius, residuals
r_r	inner radii of air gap
r_s	outer radii of air gap
R	resistance

s	short notation in 1-D formulations, slip
S	cross-section area, short notation in 2-D formulations
t	short notation in 1-D formulations, time
T	short notation in 2-D formulations, time period, torque
u	voltage
V	volume
w	weighting function
x, y, and z	Cartesian spatial coordinates
z_i	upper integration bound
α	rotation angle
β	constant related to time-discretization
γ	1-D solution region
Γ	number of harmonics
θ	angle of magnetic flux density vector
μ	permeability
μ_0	permeability of free space
ν	reluctivity
$\lvert\underline{\nu}\rvert$	absolute value of complex reluctivity
σ	electrical conductivity
ϕ	electric scalar potential
χ	relaxation factor
χ_m	magnetic susceptibility
ω	angular frequency of time variation
Ω	2-D solution region
Ω_m	mechanical angular frequency of rotor

Subscripts

ag	air gap
ave	average
b	bar, rotor
c	classical eddy current, cage, laminated core
c	either x or y
cw	coil side of phase winding
e	electromagnetic
ea	excess
eb	end of bar
ef	effective
el	electric
er	short-circuiting ring
f	field
h	hysteresis, alternating hysteresis
p	peak value

r	resistive, rotating component, radial component
s	saturation, shaft, supply, surface
w	phase winding
φ	angular component

Superscripts

Im	imaginary part
k	time-step
n	iteration
Re	real part
T	transpose of a matrix

Abbreviations

1-D	one-dimensional
2-D	two-dimensional
3-D	three-dimensional
PWM	pulse width modulation

Headings

First, second, and third level headings are numbered

Fourth level headings are in Arial, bold, font size 12

Fifth level headings are in Times New Roman, underlined, font size 14

1 Introduction

1.1 Background

The majority of the electrical energy consumed by Finnish industry, over 70%, is spent on various electrical motors that convert electrical energy into its mechanical counterpart. During the process, a great deal of energy is wasted as losses in different parts of the machines, for instance, in their laminated iron cores.

As energy efficiency and environmental issues have become increasingly important, there is a high demand for improving the qualities of electrical machinery and its utilization. To give an example, the standards concerning the energy efficiency of electrical machines have been tightened in the whole European Union and North America. Loss reductions are sought by several means. Machine designs are enhanced to a certain extent by, for instance, material choices and structural modifications. On the other hand, many simple processes, such as pumping and fanning, can be performed in a significantly more efficient manner by the intelligent control of the machines.

Because of their advantageous efficiency profiles, electrical drives consisting of a motor and a supply unit, namely a frequency converter, are being utilized increasingly nowadays. Although savings in the total energy consumption are achieved in this way, the machine itself will be exposed to non-sinusoidal supply conditions that inflict extra losses (Moses and Shirkoohi, 1987). It has been reported in the literature that the loss component that is most affected is the eddy current losses of the laminated iron core. Starting from this observation, this work is motivated to develop computational methods for the accurate modeling of eddy currents in steel laminations and, more importantly, the losses arising from them. In particular, the aim is to incorporate those phenomena directly into the field analysis of an electrical machine and make them accountable for under the complex voltage waveforms produced by a frequency converter. The topic is significant as more complete simulation tools might offer that extra insight which allows one to optimize the machine designs even further.

1.2 Literature review

Whenever an electrical steel sheet of a ferromagnetic material is exposed to a magnetic field, energy losses, so-called iron losses, will emerge in it. The mechanisms behind these losses are generally considered to be separable into the hysteresis, classical eddy current, and excess effects (Bertotti, 1988). Hysteresis refers to the microscopic-scale phenomena of a material that cause the magnetization process to be discontinuous. The classical eddy currents are regarded as macroscopic scale effects occurring in electri-

cally conducting media in the presence of varying magnetic fields. The excess effects are associated with the microscopic structure of the materials, the movements of the domain walls which cause additional local eddy current losses. Many aspects related to the different iron-loss components and their physical interpretations have been addressed, for instance in (Stewart, 1950), (Bertotti and Pasquale, 1992), and (Serpico et al., 2000).

As electrical steel sheets are an essential part of various electromagnetic devices, a vast amount of research has been conducted on them. Even so, the problem is as interesting today as ever because a definitive "standardized" way to cope with it is still lacking. The comprehensive modeling of the electrical steel sheets and the emerging losses necessitates the analysis of three-dimensional (3-D) time-dependent electromagnetic fields, including sophisticated highly non-linear and hysteretic magnetic material properties. The preceding statement encompasses rather challenging aspects. First, the electrical steel sheets have fine geometries and are used to form stacks consisting of tens to thousands of them. As a result, the fully 3-D field computation quickly turns out not to be feasible, even if simplified material modeling is adopted. Furthermore, the consideration of the magneto-dynamic phenomena of the sheets, which are the hysteresis, eddy current, and excess effects introduced above, requires not only feasible models but also powerful numerical methods for coping with the related non-linearities and notable computational resources.

The field analysis of rotating electrical machines has to be simplified in one way or another, for instance for the aforementioned reasons concerning the electrical steel sheets. That holds true despite the fact that the development of modern computers has enabled more and more complicated problems to be solved. In the case of radial flux machines, two-dimensional (2-D) finite element field computation has proven to be highly suitable (Chari and Silvester, 1971). If implemented conventionally, such an approach by definition omits the eddy currents in the sheets. In addition, the modeling of the hysteresis is typically beyond their scope and, as a result, the laminated iron core becomes treated as a non-conducting, non-linear homogenous medium. Consequently, there is only the group of post-processing techniques that are applicable to the evaluation of iron losses. While the losses might still be estimated accurately enough, their effect on the field solution is still missing.

The motivation of this thesis originates from the rapid spread of electric drive units. As the eddy current losses in the sheets appear to be the most sensitive to non-sinusoidal supply waveforms, this thesis targets their accurate analysis and thus their inclusion in the field analysis. The starting point of the research was the in-house software of the Department of Electrical Engineering, which combines the solution of the 2-D fields with the winding equations of electrical machines. The incorporation of the eddy currents of the sheets into that method is extensively investigated. For the other core-loss components a post-processing computation technique (Belahcen and Arkkio, 2008), (Belahcen and Arkkio, 2010) is employed. The following four sections try to summarize and analyze the relevant research pursued on related topics.

1.2.1 Post-processing core-loss models

The laminated iron cores of electrical machinery are nowadays still often modeled as non-conducting, non-linear media in association with numerical field analysis. This, however, implies that the evaluation of the iron losses must be carried out by some a posteriori technique based on the field solution thus obtained. The a posteriori iron-loss computation techniques have been tackled in the literature by countless means. This section tries only to give a short introduction to the topic and the main frames of development.

Bertotti formulated his idea of statistical loss theory in (Bertotti, 1988). It was stated that the total iron losses consist of three components, which are the hysteresis, classical eddy current, and excess losses, the definitions of which are given as (Bertotti, 1988)

$$\begin{aligned} P &= P_\mathrm{h} + P_\mathrm{c} + P_\mathrm{e} \\ &= C_0 B_\mathrm{p}^2 f + \frac{\pi^2 \sigma (2d)^2}{6} \left(B_\mathrm{p} f\right)^2 + C_1 \left(B_\mathrm{p} f\right)^{3/2} \end{aligned} \tag{1.1}$$

in which P_h denotes the static hysteresis loss, P_c the classical eddy current loss, P_e the excess loss, C_0 the hysteresis-loss coefficient, B_p the peak value of the magnetic flux density, f the frequency, d half of the thickness of the sheets, σ the electrical conductivity, and C_1 the excess loss coefficient.

The loss contributions in Equation (1.1) are derived on the basis of the assumption that the magnetic field varies unidirectionally and sinusoidally with respect to time and is uniform, thus neglecting the skin effect. Owing to, for instance, its geometry, material properties, and possibly non-sinusoidal supply conditions, the field of a rotating electrical machine hardly ever varies sinusoidally with time. Additionally, in some parts of the machine geometry, for instance in the yoke of the stator and the roots of the stator teeth, rotating flux patterns occur (Saitz, 2001).

A great deal of research has been done on amending the statistical loss theory and developing more comprehensive post-processing computation methods. The works of Fiorillo and Novikov (1990), Barbisio et al. (2004), and Yamazaki (2001b) address the effects of the non-sinusoidal magnetic flux waveforms on the losses. Fiorillo and Novikov (1990) worked out their widely popular iron-loss formulation by starting from the Fourier series representation of an arbitrary magnetic flux density. Barbisio et al. (2004) developed the statistical loss theory even further by taking into account the minor hysteresis loops. The measuring results of non-oriented sample sheets corresponded well with those from computations.

Attempts towards a more accurate post-processing evaluation of the iron losses in the presence of rotating fields have also been made. Bertotti et al. (1991) proposed a correction to the hysteresis part of the losses and gave the eddy current losses as a sum of the two alternating orthogonal components. Other work investigating the extension to rotating fields has been presented in (Domeki et al., 2004), (Belahcen and Arkkio, 2008), (Belahcen and Arkkio, 2010).

Research on the a posteriori methods of iron losses that might be of interest has also been conducted, for instance by Ali et al. (1997), Štumberger et al. (2003) and Zirka et al. (2010). As further reading on the subject, the Ph.D. thesis of Saitz (2001) is also suggested.

1.2.2 Field formulations of electrical steel sheets

This section focuses on summarizing the different applicable field formulations of the electrical steel sheets presented in the literature. The emphasis in this thesis is on the eddy currents and, furthermore, on their coupling to the 2-D analysis. Thus, although some of their modeling techniques are cited, the hysteresis and excess effects are not dealt with in a comprehensive manner. Excellent literature reviews on the hysteresis models and their identification and other related issues can be found from (Bergqvist, 1994), (Saitz, 2001), (Dlala, 2008b).

Solution of diffusion equation

Perhaps the most common approach to dealing with the problem of a laminated iron core in 3-D analysis is to enforce its structure by anisotropic material properties. Practically, the electrical conductivity in the direction perpendicular to the sheets is set to zero or to a very low value (Silva et al., 1995). The modeling of the hysteresis is omitted and the magnetic material properties in different directions are instead given by a single-valued magnetization curve. The drawback of descriptions such as this is that the phenomena in the lamination thickness are neglected and only the losses resulting from leakage fluxes are encompassed. The formulation can be improved by, for instance, computing the eddy currents within the thickness of the sheets separately (Hollaus and Biro, 2000), (Muramatsu et al., 2004), (Preis et al., 2005). In (Hollaus and Biro, 2000), it was shown that the eddy current losses obtained by the anisotropic approach are heavily dependent on how the value of electrical conductivity normal to the steel sheets is chosen. More importantly, the approach that is presented was found to produce eddy current losses comparable to those from analyses of a model in which each of the steel sheets in the stack is taken into account individually. Muramatsu et al. (2004) founded their method on the anisotropic-material-based 3-D formulation of the laminated core, as Hollaus and Biro (2000), and combined it with a one-dimensional (1-D) eddy current analysis of separate sheets. The eddy current modeling, however, was realized in a post-

processing manner, having no influence on the 3-D fields. The validity of the proposed approach was demonstrated by a comparative study with a complete stack model consisting of individual sheets.

The 3-D modeling of laminated iron cores has also been tackled in, for instance, (Dular et al., 2003), (Gyselinck and Dular, 2004), (Gyselinck et al., 2006), (Gyselinck and Lopez-Fernandez, 2006), and (Kawase et al., 2003). The works presented by Dular et al. and Gyselinck et al. study the homogenization of the laminated media and present it as a continuum. In (Dular et al., 2003), both the low- and high-frequency implementations were shown with linearized magnetic material properties. The high-frequency model was developed with sinusoidal time variation being assumed. The extension of the high-frequency formulae to the general time variation was introduced in (Gyselinck and Dular, 2004). A verification of the proposed method was carried out through a comparative study. In (Gyselinck et al., 2006), time-varying fields were considered together with saturable sheets. The flux patterns from the homogenization technique were compared with those from a complete formulation in a 3-D axisymmetric test geometry.

Kawase et al. (2003) employed a 3-D computation to solve a region of the geometry of an interior permanent magnetic machine that covers 1/8 of its sheet. The eddy current losses in the sheets were calculated from the eddy current density and the hysteresis losses by a post-processing technique presented in (Yamazaki, 2001a). The iron losses in the rotor of the machine were found to be 10% of the total iron losses. The inclusion of the hysteresis of the sheets in the 3-D field equations has been investigated in, for instance, (Leite et al., 2008).

One-dimensional fields

The electromagnetic field problem of electrical steel sheets can often be simplified by taking advantage of their geometrical measurements. Instead of performing a fully 3-D analysis, 2-D cross-sectional fields or 1-D formulations can be considered. Relevant literature addressing these two approaches is discussed next.

The transverse dimensions of electrical steel sheets are often considerably greater than their thickness. This allows one to neglect the edge effects and to develop the field formulation of the sheets in their thickness (Lammeraner and Stafl, 1966). Under an alternating excitation, the electromagnetic field in a sheet thus becomes (Gillott and Calvert 1965), (Del Vecchio, 1980)

$$\frac{\partial^2 H_x(z,t)}{\partial z^2} = \sigma \frac{\partial B_x(z,t)}{\partial t} \tag{1.2}$$

in which σ denotes the electrical conductivity, z the Cartesian coordinate in the direction of the thickness of the sheets, t time, H_x the x-component of the magnetic field strength, and B_x the x-component of the magnetic flux density. The term 'alternating' is generally used to refer to problems for which the variation of the magnetic field is unidirectional with respect to time.

As electrical steel sheets exhibit hysteretic behavior, attaining a complete overview requires the relation between $\boldsymbol{B}$ and $\boldsymbol{H}$ within the diffusion equation (1.2) to be represented by some hysteresis model. This matter has been tackled by several authors. In (Del Vecchio, 1980) the classical or scalar Preisach model (Preisach, 1935) was utilized by means of a simplified mathematical treatment founded on the Everett functions. The iron losses of a test sample measured under sinusoidal supply conditions showed good agreement with the computed losses. Other relevant research addressing the inclusion of the hysteresis through the classical Preisach model can be found from (Del Vecchio, 1982a), (Appino, 1996), (Bottauscio et al., 2000a).

The classical Preisach model omits the excess effects resulting from the movements of the domain walls in ferromagnetic materials. The rate-dependent or dynamic Preisach hysteresis model was developed to overcome this simplification (Bertotti, 1991), (Bertotti, 1992). The solution of the diffusion equation (1.2) by employing the dynamic Preisach model has been investigated in, for instance, (Philips et al., 1994), (Philips and Dupré, 1996), (Basso et al., 1997), (Dupré et al. 1996), (Dupré et al., 1997a), (Dupré et al., 1998), (Dupré et al., 1999), (Bottauscio et al., 2000a). Basso et al. (1997) continued the work started in (Appino et al., 1996) by coupling the 1-D Maxwell's equations of the electrical steel sheets to the dynamic Preisach hysteresis. The excess losses were found to follow the statistical law up to frequencies of 200–400 Hz. Phillips et al. (1994) compared the classical and generalized dynamic approaches of Preisach modeling. As excess effects were significant in the test samples used, the dynamic Preisach technique traced the measured $\boldsymbol{B}$-$\boldsymbol{H}$ loops with a substantially higher accuracy than the classical one. A comparative study of the classical and dynamic Preisach models was also carried out in (Dupré et al., 1997a). The authors came to the same conclusion as Phillips et al.; the dynamic Preisach model estimates the measured characteristics of the test sheets considerably better than the classical one. In (Dupré et al., 1998), the performance of the classical and dynamic Preisach models under arbitrary flux excitation was investigated. The dynamic implementation was reported to provide the best approximations in comparison with the measuring results.

Besides the hugely popular Preisach-type ones, other hysteresis modeling approaches have been investigated as well. Zirka et al. (Zirka et al., 2002), (Zirka et al., 2005), (Zirka et al., 2006), (Marketos et al., 2008), (Zirka et al., 2008a), (Zirka et al., 2008b), (Zirka et al., 2010) have carried out a great deal of research on viscous-type hysteresis models. The first attempts were made in (Zirka et al., 2002). An alternating 1-D field formulation of an electrical steel sheet was considered, giving the relation between $\boldsymbol{B}$ and $\boldsymbol{H}$ by a history-dependent hysteresis model (Zirka and Moroz, 1999) and including the excess losses by a model derived from the Landau-Lifshitz-Gilbert equation. An ad-

vantage of the approach is that the modeling of the excess losses is not an inherent part of the hysteresis model; any static hysteresis model can be applied instead. In (Zirka et al., 2005), the individual loss components were explored more carefully. The total losses in the non-oriented test sheet were the greatest with the dynamic hysteresis model presented. Moreover, a redistribution of the losses was observed as at the same time the classical eddy current losses from the static hysteresis model excluding the excess effects were larger than those from the dynamic one. A verification of the proposed model by measurements was shown in (Zirka et al., 2006).

In many applications, for instance in rotating electrical machinery, the flux density variation is rotating and not purely alternating. If the 1-D approximation is being employed, the electromagnetic field in an electrical steel sheet is then governed by (Lammeraner and Stafl, 1966), (Del Vecchio, 1982b)

$$\frac{\partial^2 H_x(z,t)}{\partial z^2} = \sigma \frac{\partial B_x(z,t)}{\partial t}, \quad \frac{\partial^2 H_y(z,t)}{\partial z^2} = \sigma \frac{\partial B_y(z,t)}{\partial t} \tag{1.3}$$

in which H_y is the y-component of the magnetic field strength and B_y the y-component of the magnetic flux density. The two equations (1.3) describing the field in an electrical steel sheet are coupled through the ***B*-*H*** relations and possibly through the boundary conditions.

Del Vecchio (1982b) utilized a single-valued magnetization curve to represent the constitutive relation between the magnetic flux density and the magnetic field strength. The study revealed that summing the eddy current losses created by two components x and y acting separately yields a result that corresponds well with that evaluable from Equation (1.3) under a rotating flux excitation. This issue was carefully analyzed in (Mayergoyz, 1998). Mayergoyz stated that the rotating eddy current losses correspond exactly to those calculable as a sum of the two individual alternating eddy current loss components x and y if the magnetic flux density over the lamination cross-section is uniform. Other interesting works addressing the modeling of rotational fields appear in (Mayergoyz and Abdel-Kader, 1984) and (Gyselinck et al., 1999).

The incorporation of the hysteretic behavior of ferromagnetic materials into rotating field formulae requires the utilization of a vector hysteresis model (Mayergoyz, 1991). The analysis of the rotating 1-D fields in electrical steel sheets, including hysteresis, has been addressed in relatively few works. Bottauscio and Chiampi (2001) extended their alternating field formulation (Bottauscio et al., 2000a) to rotating fields by applying a vector hysteresis model founded on stop operators. As the hysteresis model utilized was a rate-independent one, the excess effects were omitted from the analysis. Even then, the computed static hysteresis and eddy current losses were in reasonable agreement with the measured ones. More recently, Dlala et al. (2008d) introduced a magneto-dynamic model of laminations that employs the generalized vector hysteresis model of Mayergoyz (2003) in a modified manner. In principle, the directions of the vector hys-

teresis model are represented by a viscosity-based model as a sum of the static hysteresis model and an excess effects term.

Two-dimensional fields

The limitations of the 1-D field formulations of electrical steel sheets have been analyzed in, for instance, (Bottauscio et al., 2000b) and (Chevalier et al., 2000a). Both the works study the alternating cross-sectional fields in the laminations. Bottauscio et al. (2000b) showed that the 1-D approximation overestimates the losses, especially the eddy current losses. Chevalier et al. (2000a) defined a limit for the applicability of the 1-D formulation by means of a qualitative analysis; the ratio of the thickness of the sheets to their width should be more than 10.

The alternating cross-sectional field analysis has also been investigated, for instance, by Rouve et al. (1996), Gyselinck et al. (1999) and Chevalier et al. (2000b). Rouve et al. (1996) carried out a thorough study by employing three different ways to represent the ***B*-*H*** relations: a single-valued magnetization curve and static and dynamic Preisach models. The simulated losses and ***B*-*H*** loops were compared with the measurements. In both respects, the dynamic Preisach model was found to result in the best accuracy. Chevalier et al. (2000b) used a single-valued magnetization curve and a Duhem-type hysteresis model (Potter and Schmulian, 1971) to solve the cross-sectional field in an electrical steel sheet. Similar observations as in Chevalier et al. (2000b) were made; the measured losses agree better with the computed ones if the hysteresis is included. However, as the frequency increases the differences between the two methods of material modeling become smaller.

Matsuo et al. (2000) solved the rotating cross-sectional field in a lamination representing the magnetic constitutive relation by a vector hysteresis model based on play and stop hysterons (Bobbio et al., 1997). The stop hysteron model was proven to be computationally more efficient than the play hysteron one.

Simplified models of electrical steel sheets

This section explores the possibilities discussed in the literature for modeling the magneto-dynamic effects in electrical steel sheets within the 2-D or 3-D analysis without actually having to solve the diffusion equation in them. These sorts of simplified formulations may offer computationally efficient yet accurate enough ways to analyze complicated apparatuses such as rotating electrical machines. In addition, approaches introducing the assumption of sinusoidal time variation are touched on.

Zirka et al. (2008a) investigated several aspects concerning the modeling of electrical steel sheets. First, a finite difference formulation for the 1-D alternating field (penetration equation (1.2)) that utilized the viscous-type hysteresis model (Zirka et al., 2004), (Zirka et al., 2006) was proposed. Second, a solution of the 1-D problem that omitted the excess effects and thus considered only static hysteresis was studied. In addition to the complete ones, simplified approaches were also proposed. The main idea in these is to assume the sheets to be thin with a uniform flux density (or the frequency to be low), in which case the skin effect can be neglected (Jiles, 1994). The magnetic field strength in the sheets is then given as a sum of three components originating from the three iron-loss components. Such a description of $\boldsymbol{H}$ can be used in 2-D and 3-D field analyses to account simply for the magneto-dynamic effects. The simplified thin sheet model was found to perform well up to a frequency of 200 Hz. However, this resulted partly from the estimation error of the component of the classical eddy current loss. Experimental results from a single sheet tester and Epstein frame were used to verify the models. In (Zirka et al., 2008b), the applicability of these in voltage- and current-driven problems was analyzed.

Dlala (2008a) improved the thin sheet model (Jiles, 1994) further by obliging the eddy current and excess terms of the magnetic field strength to be dependent on the magnetization and thus including the skin effect. The simplified formulation of the electrical steel sheets obtained thereby was compared with measurements and with a complete model, i.e., solving the penetration equation with hysteretic material properties. The agreement was found to be good.

Owing, for instance, to its material properties, the time variation of the electromagnetic field in an electrical steel sheet is practically never sinusoidal. Even though the approximation of the sinusoidal time variation is thus not strictly suited for the analysis of electrical machinery, attempts to utilize it have been made (Niemenmaa, 1988), (Arkkio et al., 1998), (Pippuri and Arkkio, 2009), and (Jagiela et al., 2010). Pippuri and Arkkio (2009) developed a computational routine based on the time-harmonic approximation which can still be applied to study the additional electromagnetic losses as a result of the frequency-converter supply. The governing equations were those of the 2-D finite element analysis to which the hysteresis and eddy currents in the sheets were coupled through a complex reluctivity. The measured results of a frequency-converter-fed induction motor were in satisfactory correspondence with those from simulations. Other works related to the time-harmonic modeling of the phenomena in electrical steel sheets have been presented, for instance, in (O'Kelly, 1972), (Hollaus and Biro, 2002).

1.2.3 Incorporation of the magneto-dynamic effects of electrical steel sheets into field analysis of electrical machinery

In this section, the coupling of the magneto-dynamic effects of the electrical steel sheets to the field analysis of electrical machinery is discussed. The aim is, especially, to ad-

dress the relevant literature concerning the 2-D approaches that encompass sophisticated models of the sheets. Some remarks about the numerical techniques are also made.

By far the simplest way to include the eddy currents in the 3-D or 2-D analysis is to neglect the skin effect and define the constitutive relation between $\boldsymbol{B}$ and $\boldsymbol{H}$ by an irreversible law, as in (Stillesjö et al., 1998), (Gyselinck et al., 1999), (Dular et al., 2003)

$$\boldsymbol{H} = \nu\left(\boldsymbol{B}^2\right)\boldsymbol{B} + \frac{1}{12}\sigma\left(2d\right)^2\frac{\partial \boldsymbol{B}}{\partial t} \tag{1.4}$$

in which ν is the reluctivity of the laminations. Gyselinck et al. (1999) carried out a thorough analysis of the limitations of the approach and justified its usability at low frequencies.

Righi et al. (2001) incorporated the eddy currents in electrical steel sheets in 2-D finite element analysis in a rather similar manner to (Gyselinck et al., 1999), (Dular et al., 2003). However, besides the eddy currents, the hysteresis and excess effects were also taken into account and $\boldsymbol{H}$ was defined as a sum of three components. Measurements on a voltage-fed Epstein frame were employed for verification. The measured current showed good correspondence with that computed by the proposed method. On the other hand, when the iron losses were omitted, the prediction of the current did not succeed in an application without an air gap, such as the Epstein frame. In (Sadowski et al., 2002) the technique presented in (Righi et al., 2001) was further developed by introducing an inverse Jiles-Atherton-type hysteresis model (Jiles and Atherton, 1984). A comparative study of the measured and computed currents verified the applicability of the proposed model.

If the actual magnetic properties and skin effect in the sheets need to be taken into account, an approach like that in Equation (1.4) may become insufficient. More complete formulations have been analyzed in (Dupré et al., 1997b), (Bottauscio et al., 2000), (Bottauscio and Chiampi, 2001), (Bottauscio and Chiampi, 2002), (Dlala et al., 2008c). Bottauscio et al. (2000) introduced a 2-D field formulation, the material modeling of which was realized with a 1-D model of the sheets, including hysteresis. Alternating fields employing classical (static) and dynamic Preisach hysteresis models were considered. The resulting non-linear system of equations was solved as a truncated Fourier series with the fixed point technique in association with the finite elements. For the verification, measurements on an eccentric toroid were used. The measured currents and instantaneous powers were found to show good correspondence with the computed ones. The method was extended in (Bottauscio and Chiampi, 2001) for rotating fields. Simulations and experiments were performed on a ferromagnetic disk with a diameter of 90 mm and the losses from these two showed good agreement. In (Bottauscio and Chiampi, 2002a), the 1-D formulation was directly incorporated into the 2-D system matrices in order to avoid nested iteration schemes.

More recently, research on the coupled 2-D–1-D model has been conducted by Dlala et al. (2008c). Thanks to the parallel iteration of the 2-D and 1-D formulae, the method showed good computational efficiency. The numerical form of the equations was produced by the finite element and Crank-Nicolson methods, while the non-linearities were handled by the fixed point technique.

1.2.4 Application of the iron-loss computation methods to electrical machinery

The comprehensive models of electrical steel sheets, by which it is meant that they encompass the hysteresis, eddy current, and excess effects, have been applied in many works to analyze rather simple geometries, such as toroids. The iron losses of complex apparatuses, such as rotating electrical machines, are still commonly evaluated by post-processing techniques. Some works, however, also address their inclusion in the field solution. This section aims at discussing the relevant research conducted on the topic of modeling iron losses in electrical machinery.

Post-processing techniques

The evaluation of iron losses in electrical machines as post-processing has been studied, for instance, in (Atallah et al., 1992), (Sadowski et al., 2000), and (Štumberger et al., 2003). Sadowski et al. (2000) computed the three iron-loss components from the instantaneous values of the magnetic flux density. The main contribution of the research was in defining the losses resulting from the minor hysteresis loops by a rain-flow method. In principle, the hysteresis part of the total losses was formulated in a similar way to, for instance, in (Atallah et al., 1992). A time-stepping finite element analysis was performed on two different electrical machines, from the results of which the iron losses were evaluated with the proposed technique. The computations were verified by measurements.

Štumberger et al. (2003) studied an induction motor by finite elements using six different a posteriori iron-loss computation methods. The eddy current losses were computed traditionally, with the skin effect being neglected, while the original idea was to compare different expressions of hysteresis losses. The authors stated that the sum of the hysteresis losses caused by two alternating orthogonal flux components acting separately is a sufficient approximation of the total hysteresis loss. However, if the rotating nature of the flux patterns is taken into account, the agreement between the measured and computed losses is improved.

The output-voltage waveform produced by a frequency converter is known to increase the losses in electrical machinery in comparison with a purely sinusoidal supply. A

Japanese research group (Yamazaki and Seto, 2006), (Yamazaki and Fukushima, 2010) has studied the iron losses of frequency-converter-fed electrical machines employing different post-processing formulations. Yamazaki and Seto (2006) used 2-D transient non-linear finite element analysis to model an interior permanent magnet machine. It was supplied by a voltage waveform that accords with the one generated by the control methodology of a real pulse width modulation-based (PWM) converter. The iron losses were computed by the well-known statistical model. In the work exhaustive analysis of the different origins, carrier harmonics, slot harmonics etc. and the resultant iron losses was shown. In (Yamazaki and Fukushima, 2010), the computation of the eddy current losses of the sheets was improved by directly solving those from a 1-D penetration equation. Several measurements performed on a frequency-converter-fed test machine proved the validity of the approach.

Other works addressing the iron-loss analysis of PWM-fed electrical machines can be found from (Cester et al., 1997), (Hildebrand and Roehrdanz, 2001), (Green et al., 2003), (Lee et al., 2004), (Sagarduy et al., 2006). Most of these works simply evaluate the iron losses as post-processing with a statistical-like iron-loss model. In (Hildebrand and Roehrdanz, 2001), however, the machine modeling is based on an equivalent circuit, not on numerical field analysis. Hence, the eddy currents arising in the core are determined through an iron impedance. Green et al. (2003), among others, performed an extensive analysis of the iron losses of a test machine under different loading conditions when supplied from a sinusoidal and frequency-converter voltage source. Generally, the iron losses appeared to be independent of the slip. In comparison to the sinusoidal supply, the rotor eddy current losses were the most sensitive to the frequency-converter output voltage. Lee et al. (2004) tackled the problem with a variable-step finite element algorithm.

Comprehensive field formulations

Although the majority of the works study the post-processing techniques, extensive field formulations including the phenomena in the sheets have also been applied to rotating electrical machines. In this connection the 3-D approaches, which commonly encompass either eddy currents or hysteresis, are not considered. Instead, the 2-D and 1-D approaches and combinations of those are discussed.

One of the first studies modeling both the eddy currents and hysteresis in the sheets of a rotating electrical machine was performed by Dupré et al. (1997b). They analyzed the region of one tooth of a test machine by means of a two-level model. The cross-sectional 2-D field in the tooth is first evaluated as a flux-driven problem with suitable boundary conditions. Next, the local 1-D fields are solved using the 2-D field as an excitation. A 3-kW cage-induction motor was utilized as a test motor, and for this the losses computed by the proposed method were in reasonable agreement with those obtained by measurements. The method that is discussed is, in fact, a post-processing one

as there is no feedback from the 1-D model to the 2-D one. However, its loss computation is founded on the actual solution of the field in the lamination depth employing a hysteresis model and can be seen as a first attempt to couple the 2-D and 1-D formulations. In (Gyselinck et al., 1998), a similar approach to that of (Dupré et al., 1997b) was utilized but a more detailed analysis of the 3-kW test machine was shown. Gyselinck et al. (2000) developed their method further, now omitting the solution of the 1-D penetration equation. Instead, a 2-D formulation in which the eddy currents were incorporated as in Equation (1.4) and hysteresis implemented by the Preisach model was proposed. Another work of the group that might be of interest is that of Dupré et al. (2003).

Dlala (2009a) carried out an extensive study of the iron losses in a 37-kW test induction motor. Two types of finite element analyses in which the magneto-dynamic effects in the sheets were incorporated were considered. First, the 2-D finite element formulation of a cross-sectional field was coupled with the 1-D penetration equation of the sheets including dynamic hysteresis. Second, an improved thin sheet formulation (Dlala, 2008a) was used to derive the 2-D equations. The latter method was found to be computationally efficient and stable.

Frequency-converter-fed electrical machines

An Italian research group has conducted a great deal of research into iron losses in devices under distorted supply conditions (Boglietti et al., 1991), (Boglietti et al., 1996), (Boglietti et al., 1998). In (Boglietti et al., 1991), a major increase in the iron losses of a simple test object, i.e., in a steel sheet, as a result of the PWM supply was reported. Later on, the authors analyzed the same problem by a 1-D approach, including hysteresis (Boglietti et al., 1996), (Boglietti et al., 1998). The measured and computed losses were in sufficient accordance with each other and several aspects concerning the switching frequency and modulation index of the PWM supply were investigated. Modeling a single sheet with a PWM supply has also been addressed, for instance in (Leonard et al., 2006).

Lately, some works have appeared that study frequency-converter-fed electrical machines by means of advanced field analysis techniques. Bottauscio et al. (2002b) analyzed a motor model which had a slotless, solid rotor. Three different iron-loss computation methods, two of which were a posteriori ones, were applied. The third one included the hysteresis in the field solution but evaluated the eddy current and excess losses as post-processing. The no-load operation of the motor model was examined under different supply conditions. The hysteresis losses from the comprehensive approach agreed rather well with those from the a posteriori calculations. In (Bottauscio et al., 2003), the authors solved the stator fields in a 7.5-kW test induction motor, including the eddy currents and hysteresis in the sheets (Bottauscio and Chiampi, 2001), (Ragusa and Repetto, 2000). To compare, the same problem was also analyzed with only hysteretic material properties and by employing a single-valued magnetization curve. The au-

thors stated that the flux patterns are not appreciably affected by the comprehensiveness of the material modeling. In addition, the total iron losses from a post-processing technique used by Fiorillo and Novikov (1990) did not differ notably from those obtained directly from the field solution at frequencies below 400 Hz. A comparative study of the iron losses under a sinusoidal and six-step supply was carried out. A moderate increase in those resulting from the frequency-converter supply was observed.

Perhaps the latest work on the topic was conducted by Dlala and Arkkio (2009b). They investigated the losses of a frequency-converter-fed 37-kW induction machine. The field computation was based on 2-D finite element analysis, into which the magneto-dynamic effects in the sheets were incorporated by means of an advanced thin sheet model. Several operating points of the test motor were computed and the total electromagnetic losses obtained were found to correspond with experiments. In the iron losses, an increase of 6–66% as a result of the frequency-converter supply was observed.

1.2.5 Conclusion

The literature survey that was conducted revealed that the iron-loss computation of rotating electrical machines is largely based on post-processing. There is thus a need for more complete formulations of the magnetic fields in which the core losses are included. Attaining such a goal would lead to a better estimation of the flux patterns and the losses themselves. Interesting work on rotating electrical machines has been carried out in (Bottauscio et al., 2003), (Dlala, 2009a), and (Dlala and Arkkio, 2009b). However, it seems that the core losses in a frequency-converter-fed machine have not been analyzed by solving the actual field distribution of the sheet from the diffusion equation.

In addition, there are some works that investigate the coupling of the magneto-dynamic effects in electrical steel sheets to 2-D field analysis. It was observed, however, that not very much attention has been paid to the reliability and accuracy of the coupling. This refers to how the 1-D field solution obtained should be utilized in order to include the associated losses correctly in the 2-D computation scheme. This work aims at producing new information on this topic. Last, the possibilities of linearizing the field problem of the sheets in order to gain better computational efficiency are investigated.

1.3 Aim of the work

This work aims at developing computational methods that are based on the 2-D finite element analysis of the field but still include the eddy currents in electrical steel sheets. Despite the awareness that the phenomena in the sheets are interdependent, only the eddy currents are mostly considered. This is a consequence of the other objective of the thesis, which is to analyze the losses in frequency-converter-fed rotating electrical ma-

chines under practical operating conditions. According to the literature survey, the eddy current contribution of the total iron losses appears to be the aspect which is most affected by the higher harmonics of the frequency-converter supply (Boglietti et al., 1996), (Boglietti et al., 1998). On the basis of this observation, a decision was made to omit the hysteresis and excess effects from the field computation and simply approximate the losses related by a post-processing technique. Last, the development and improvement of techniques for coping with the non-linearity of the problem are beyond the scope of this thesis. Thus, the stability of the computations is ensured by relatively simple means which, on the other hand, might not be the most efficient ones.

1.4 Scientific contribution

The scientific contributions of the thesis can be listed as follows.

1. Within this thesis a time-discretized 2-D finite element model of electrical machines, including the eddy currents in electrical steel sheets through a 1-D diffusion equation, is presented. Particularly, this work contributes by carefully investigating how the 1-D field solution is accurately coupled with the 2-D equations, i.e., how the eddy current loss involved is fully included in the 2-D analysis.

2. The thesis discusses two approaches used to represent the 1-D solution in the 2-D machine model. The effects of the spatial discretization of the 1-D diffusion equation are studied. The results show the importance of the appropriate space-discretization. A proposal for an optimal coupling that accords with the results is given.

3. The linearization of the 1-D model in association with the time-discretized coupled approach is studied. It is found that there is virtually no need to take into account the magnetic non-linearity of the sheets within the 1-D model when the skin depth is greater than one fifth of the sheet thickness.

4. The time-discretized method for encompassing the eddy currents in the sheets is used to model the test machine under different supply and loading conditions. A comparison of the simulation results with experimental ones verifies the applicability of the approach.

5. A simpler method for including the eddy current and hysteretic effects in the electrical steel sheets of electrical machines is presented. It is founded on the approximation of sinusoidal time variation. Owing to its implementation the method is suitable for analyzing the additional electromagnetic losses caused by

the non-sinusoidal voltage waveforms produced by frequency converters. Highly efficient computational performance is attained, slightly at the expense of the accuracy of the results.

1.5 Outline of the thesis

This thesis is organized in the following way.

- Chapter 1 elaborates the background of the research, discusses the relevant literature, and emphasizes the motivations for the work. The scientific contributions are summarized as well.

- In Chapter 2, the computational methods developed are discussed in a detailed manner, starting from the basic equations of the field and windings and ending up with the non-linear system of equations and its solution. The second section of the chapter concentrates on discussing the experimental part of the research.

- Chapter 3 represents the most important results obtained during the course of the work. The general characteristics of the methods are first closely investigated via simple example geometries. Second, a 37-kW cage-induction machine is analyzed under different operating conditions with sinusoidal and frequency-converter supplies.

- Last, in Chapters 4 and 5, the methods, results, and fulfillment of the aims are carefully discussed. Chapter 5 summarizes the content of the thesis.

2 Methods

2.1 Finite element model for cage-induction machines

This section discusses the computational methods that were developed. The 1-D field formulation of electrical steel sheets is dealt with first. Next, the 2-D finite element model of cage-induction machines is presented and the coupling of the eddy currents in electrical steel sheets elaborated. The derivations and solution methods are given for both a general time variation and the approximation of sinusoidal time variation.

2.1.1 One-dimensional eddy current model of electrical steel sheets

The 1-D eddy current formulation of electrical steel sheets is discussed. The fundamental electromagnetic field equations are presented. The solution of the 1-D field problem in both the time-stepping and time-harmonic schemes is shown.

Fundamental equations

The electromagnetic field in an electrical steel sheet is governed by the quasi-static Maxwell's equations

$$\nabla \times \boldsymbol{E} = -\frac{\partial \boldsymbol{B}}{\partial t} \tag{2.1}$$

$$\nabla \times \boldsymbol{H} = \boldsymbol{J} \tag{2.2}$$

$$\nabla \cdot \boldsymbol{B} = 0 \tag{2.3}$$

and constitutive relations

$$\boldsymbol{J} = \sigma \boldsymbol{E} \tag{2.4}$$

$$\boldsymbol{B} = \mu_0 \left(\boldsymbol{H} + \boldsymbol{M} \right) \tag{2.5}$$

where $\boldsymbol{E}$ is the electric field strength, $\boldsymbol{B}$ the magnetic flux density, t time, $\boldsymbol{H}$ the magnetic field strength, $\boldsymbol{J}$ the current density, σ the electrical conductivity, μ_0 the permeability of free space, and $\boldsymbol{M}$ the magnetization.

The term $\partial \boldsymbol{D}/\partial t$, which is related to the polarization and displacement currents, is omitted from the field formulation (Equation (2.2)). Applying the resulting so-called quasi-

static approximation is well justified here, since at the frequencies present in an electrical machine, the emerging conductive currents are substantially greater than the polarization and displacement ones.

The constitutive relation between the magnetic flux density and magnetic field strength is given in its most general form in Equation (2.5). Utilizing this kind of expression is necessary if the hysteretic and even anisotropic characteristics exhibited by the ferromagnetic steel sheets need to be included in the analysis. However, the solution of the eddy current problem in question is simplified substantially if the modeling of these phenomena can be omitted. Then the magnetic properties of the materials can be described with a single-valued magnetization curve. This approach is adopted here. The magnetization can be expressed as

$$\boldsymbol{M} = \chi_{\mathrm{m}} \boldsymbol{H} \tag{2.6}$$

in which χ_{m} is the magnetic susceptibility of a material. Substituting Equation (2.6) in Equation (2.5) yields

$$\boldsymbol{B} = \mu_0 \left(1 + \chi_{\mathrm{m}}\right) \boldsymbol{H} \,. \tag{2.7}$$

Furthermore, by utilizing permeability μ or its inverse reluctivity ν, Equation (2.7) can simply be written as

$$\boldsymbol{B} = \mu \boldsymbol{H} \text{ or as } \boldsymbol{H} = \nu \boldsymbol{B} \,. \tag{2.8}$$

In the case of electrical steel, the permeability (or its inverse reluctivity) is a non-linear function of the magnetic field.

The definition of the magnetic vector potential $\boldsymbol{A}$ is

$$\boldsymbol{B} = \nabla \times \boldsymbol{A} \,. \tag{2.9}$$

Since the curl of the gradient of any scalar function is identically zero, the uniqueness of the magnetic vector potential needs to be ensured by an additional constraint. In the quasi-static field problems, Coulomb's gauge is frequently utilized:

$$\nabla \cdot \boldsymbol{A} = 0 \,. \tag{2.10}$$

In terms of magnetic vector potential, Ampère's circuital law (2.2) fulfils

$$\nabla \times \nu \nabla \times \boldsymbol{A} = \boldsymbol{J} \,. \tag{2.11}$$

The substitution of Equation (2.9) into Equation (2.1) gives

$$\nabla \times \boldsymbol{E} = -\frac{\partial}{\partial t} \nabla \times \boldsymbol{A} . \tag{2.12}$$

By introducing the electric scalar potential ϕ, the electric field strength can be written as

$$\boldsymbol{E} = -\frac{\partial \boldsymbol{A}}{\partial t} - \nabla \phi . \tag{2.13}$$

Taking a curl of the above expression of the electric field strength Equation (2.13) yields Equation (2.12), since the curl of the gradient of the electric scalar potential is identically zero.

Utilizing the Ohm's law (2.4) and the definition of the electric field strength in Equation (2.13), one can express the current density as

$$\boldsymbol{J} = -\sigma \frac{\partial \boldsymbol{A}}{\partial t} - \sigma \nabla \phi . \tag{2.14}$$

The current density (2.14) satisfies the continuity equation

$$\nabla \cdot \boldsymbol{J} = 0 . \tag{2.15}$$

Combining Equation (2.14) with Equations (2.11) and (2.15) results in two partial differential equations from which the vector and scalar potentials can be solved

$$\nabla \times \nu \nabla \times \boldsymbol{A} + \sigma \frac{\partial \boldsymbol{A}}{\partial t} + \sigma \nabla \phi = 0 \tag{2.16}$$

$$\nabla \cdot \left(\sigma \frac{\partial \boldsymbol{A}}{\partial t} + \sigma \nabla \phi \right) = 0 . \tag{2.17}$$

The above derivations are presented in the most general case, i.e., in three dimensions. However, if the width and length of the electrical steel sheets are much greater than their thickness, the edge effects become negligible and the intrinsically 3-D eddy current problem can be reduced to a 1-D one without a great loss of accuracy (Lammeraner and Stafl, 1966). Employing the 1-D approximation of the field, for the sheets positioned in the same way as the one in Figure 2.1, the magnetic vector potential and current density can be formulated as

$$\boldsymbol{a} = a_x(z,t)\boldsymbol{e}_x + a_y(z,t)\boldsymbol{e}_y \tag{2.18}$$

$$\boldsymbol{j} = j_x(z,t)\boldsymbol{e}_x + j_y(z,t)\boldsymbol{e}_y \tag{2.19}$$

in which z is a Cartesian spatial coordinate and $\boldsymbol{e}_x$ and $\boldsymbol{e}_y$ are the unit vectors parallel to the x- and y-axes, respectively. a_x and a_y denote the x- and y-components of the magnetic vector potential, and j_x and j_y the x- and y-components of the current density. The 1-D quantities are throughout the thesis denoted with lower case letters in order to differentiate them from the 2-D ones.

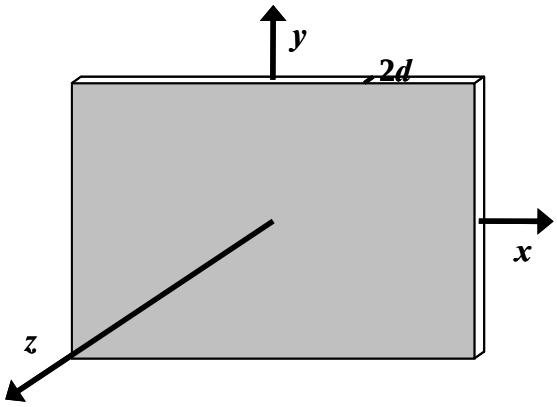

Figure 2.1 Alignment of the electrical steel sheets.

The substitution of Equation (2.18) into Equation (2.16) yields

$$\nabla \cdot \left(\nu \nabla a_x\right) - \sigma \frac{\partial a_x}{\partial t} = 0, \quad \nabla \cdot \left(\nu \nabla a_y\right) - \sigma \frac{\partial a_y}{\partial t} = 0, \quad \nabla = \boldsymbol{e}_z \frac{\partial}{\partial z}. \tag{2.20}$$

The two equivalent equations for the components of the magnetic vector potential in Equation (2.20), which define the field in the electrical steel sheets, are coupled through the reluctivity and boundary conditions. In this work, the sheets are assumed to be magnetically isotropic by giving their reluctivity in both the x- and y-directions with the same non-linear function of a square of magnetic flux density $\boldsymbol{b}^2$ (Belahcen et al., 2010).

Furthermore, the expressions for the components of current density and magnetic flux density are

$$j_x = -\sigma \frac{\partial a_x}{\partial t}, \quad j_y = -\sigma \frac{\partial a_y}{\partial t} \tag{2.21}$$

$$b_x = -\frac{\partial a_y}{\partial z}, \quad b_y = \frac{\partial a_x}{\partial z}. \tag{2.22}$$

Transient time-discretized analysis

The actual time-dependence of the 1-D electromagnetic field quantities has to be worked out numerically. The space-discretization of the 1-D problem is performed by the finite element method, whereas the time-dependence is handled by the backward Euler method. The resulting non-linear system of equations is solved within the Newton-Raphson iterative scheme.

Time-discretization

Solving the field equations of the electrical steel sheets requires the approximation of their time derivatives by some time-discretization technique. For that purpose, the backward Euler method, in association with a constant time-step of length Δt, is employed. If two successive time-steps are denoted by k and $k + 1$, both the components of the magnetic vector potential at a time instant $k + 1$ can be formulated as

$$a_c^{k+1} = a_c^k + \left[\beta \frac{\partial a_c}{\partial t} \Big|^{k+1} + (1-\beta) \frac{\partial a_c}{\partial t} \Big|^{k} \right] \Delta t \tag{2.23}$$

in which c denotes either x or y and β is a constant, depending on the time-discretization technique applied. For the backward Euler method, that constant is 1. Other common techniques include the forward Euler and Crank-Nicolson methods, in the case of which β is 0 and 0.5, respectively. The backward Euler method was chosen to be used because of its good performance with problems coupling external circuits and eddy currents (Tsukerman, 1995), (Islam, 2010).

Since the components of the magnetic vector potential fulfill the equivalent equation (Equation (2.20)), the following derivations are carried out utilizing the notation a_c, where c is either x or y. Let us write the equation for a component of magnetic vector potential at two successive time-steps $k + 1$ and k

$$\nabla \cdot \left(\nu^{k+1} \nabla a_c^{k+1} \right) - \sigma \frac{\partial a_c}{\partial t} \Big|^{k+1} = 0 \tag{2.24}$$

$$\nabla \cdot \left(\nu^{k} \nabla a_c^{k} \right) - \sigma \frac{\partial a_c}{\partial t} \Big|^{k} = 0 \,. \tag{2.25}$$

Multiplying Equation (2.24) by β and Equation (2.25) by $1 - \beta$ gives

$$\beta \nabla \cdot \left(\nu^{k+1} \nabla a_c^{k+1} \right) - \beta \sigma \frac{\partial a_c}{\partial t} \Big|^{k+1} = 0 \tag{2.26}$$

$$(1-\beta)\nabla\cdot\left(\nu^{k}\nabla a_c^{k}\right)-(1-\beta)\sigma\frac{\partial a_c}{\partial t}|^{k}=0\,. \tag{2.27}$$

Summing Equations (2.26) and (2.27) yields

$$\beta\nabla\cdot\left(\nu^{k+1}\nabla a_c^{k+1}\right)-\beta\sigma\frac{\partial a_c}{\partial t}|^{k+1}+(1-\beta)\nabla\cdot\left(\nu^{k}\nabla a_c^{k}\right)-(1-\beta)\sigma\frac{\partial a_c}{\partial t}|^{k}=0\,. \tag{2.28}$$

Utilizing the expression of Equation (2.23), the derivative terms of Equation (2.28) can be eliminated

$$\nabla\cdot\left(\nu^{k+1}\nabla a_c^{k+1}\right)-\frac{\sigma}{\beta\Delta t}a_c^{k+1}+\frac{(1-\beta)}{\beta}\nabla\cdot\left(\nu^{k}\nabla a_c^{k}\right)+\frac{\sigma}{\beta\Delta t}a_c^{k}=0\,. \tag{2.29}$$

Space-discretization

The spatial discretization is accomplished by the finite elements together with the method of weighted residuals. Transforming the governing differential equations into a variational form is done by the weighted residuals method. The finite element method is then used to discretize the solution region of the problem in question into a finite element mesh in which the unknowns are approximated as a linear combination of suitable functions employing appropriate boundary conditions.

According to the method of weighted residuals, the field equation (2.29) is multiplied by a weighting function $w(z)$ and integrated over the whole solution region γ:

$$\int_{\gamma}\left(\nabla\cdot\left(\nu^{k+1}\nabla a_c^{k+1}\right)w-\frac{\sigma}{\beta\Delta t}a_c^{k+1}w+\frac{(1-\beta)}{\beta}\nabla\cdot\left(\nu^{k}\nabla a_c^{k}\right)w+\frac{\sigma}{\beta\Delta t}a_c^{k}w\right)\mathrm{d}\gamma=0\,. \tag{2.30}$$

As the symmetry of the electrical steel sheets is exploited, only half of their thickness needs to be considered (the solution region covers half of the thickness of the sheets).

By applying the identity

$$\nabla\cdot\left(\nu\nabla a_c\right)w=\nabla\cdot\left(w\nu\nabla a_c\right)-\nu\nabla w\cdot\nabla a_c \tag{2.31}$$

Equation (2.30) can be formulated as

$$\int_{\gamma}\left(\begin{array}{l}\nabla\cdot\left(w\nu^{k+1}\nabla a_c^{k+1}\right)-\nu^{k+1}\nabla w\cdot\nabla a_c^{k+1}-\dfrac{\sigma}{\beta\Delta t}a_c^{k+1}w \\ +\dfrac{(1-\beta)}{\beta}\nabla\cdot\left(w\nu^{k}\nabla a_c^{k}\right)-\dfrac{(1-\beta)}{\beta}\nu^{k}\nabla w\cdot\nabla a_c^{k}+\dfrac{\sigma}{\beta\Delta t}a_c^{k}w\end{array}\right)\mathrm{d}\gamma=0\,. \tag{2.32}$$

Furthermore, the finite element method approximates both the components of the magnetic vector potential as

$$a_c\cong\sum_{j=1}^{n_\mathrm{n}}a_{c|j}n_j\left(z\right) \tag{2.33}$$

in which $a_{c|j}$ denotes the component of the magnetic vector potential associated with the node j of the finite element mesh, n_j the shape function associated with the node j of the finite element mesh, and n_n the number of nodes in the finite element mesh.

The nodal values of the magnetic vector potential are fixed at the boundaries of the electrical steel sheet geometry. In the rest of the nodes, i.e., in the free nodes, the solution of the magnetic vector potential is sought. A shape function n_j is a continuous real-valued function that has a non-zero value only in the elements to which the node j belongs. In the node j, the shape function n_j has a value of one and in the other nodes, it is equal to zero. Here, depending on the order of the elements, the shape functions are either first-, second-, or third-order polynomials.

Substituting Equation (2.33) in Equation (2.32) yields

$$\int_{\gamma}\left(\begin{array}{l}\nabla\cdot\left(w\nu^{k+1}\nabla\left(\sum_{j=1}^{n_\mathrm{n}}a_{c|j}^{k+1}n_j\right)\right) \\ \qquad-\nu^{k+1}\nabla w\cdot\nabla\left(\sum_{j=1}^{n_\mathrm{n}}a_{c|j}^{k+1}n_j\right)-\dfrac{\sigma}{\beta\Delta t}\left(\sum_{j=1}^{n_\mathrm{n}}a_{c|j}^{k+1}n_j\right)w \\ +\dfrac{(1-\beta)}{\beta}\nabla\cdot\left(w\nu^{k}\nabla\left(\sum_{j=1}^{n_\mathrm{n}}a_{c|j}^{k}n_j\right)\right) \\ \qquad-\dfrac{(1-\beta)}{\beta}\nu^{k}\nabla w\cdot\nabla\left(\sum_{j=1}^{n_\mathrm{n}}a_{c|j}^{k}n_j\right)+\dfrac{\sigma}{\beta\Delta t}\left(\sum_{j=1}^{n_\mathrm{n}}a_{c|j}^{k}n_j\right)w\end{array}\right)\mathrm{d}\gamma=0\,. \tag{2.34}$$

The weighting functions to be used can be chosen in many ways. Here, Galerkin's method is utilized, implying that the shape functions of the free nodes in the finite element mesh are applied as weighting functions one by one:

$$w_i\left(z\right)=n_i\left(z\right). \tag{2.35}$$

Thus, when the numbering of the free nodes runs from 1 to the total number of free nodes n_f, Equation (2.34) becomes

$$\int_\gamma \left(\begin{array}{l} \nabla \cdot \left(n_i \nu^{k+1} \nabla \left(\sum_{j=1}^{n_\mathrm{n}} a_{c|j}^{k+1} n_j \right) \right) \\ \qquad - \nu^{k+1} \nabla n_i \cdot \nabla \left(\sum_{j=1}^{n_\mathrm{n}} a_{c|j}^{k+1} n_j \right) - \frac{\sigma}{\beta \Delta t} \left(\sum_{j=1}^{n_\mathrm{n}} a_{c|j}^{k+1} n_j \right) n_i \\ + \frac{(1-\beta)}{\beta} \nabla \cdot \left(n_i \nu^{k} \nabla \left(\sum_{j=1}^{n_\mathrm{n}} a_{c|j}^{k} n_j \right) \right) \\ \qquad - \frac{(1-\beta)}{\beta} \nu^{k} \nabla n_i \cdot \nabla \left(\sum_{j=1}^{n_\mathrm{n}} a_{c|j}^{k} n_j \right) + \frac{\sigma}{\beta \Delta t} \left(\sum_{j=1}^{n_\mathrm{n}} a_{c|j}^{k} n_j \right) n_i \end{array} \right) \mathrm{d}\gamma = 0, \qquad . \quad (2.36)$$

$$i = 1, \ldots, n_\mathrm{f}$$

Integrating a derivative of a function yields the function itself:

$$\int_\gamma \nabla \cdot \left(n_i \nu \nabla \left(\sum_{j=1}^{n_\mathrm{n}} a_{c|j} n_j \right) \right) \mathrm{d}\gamma = |_\gamma \left(n_i \nu \nabla \left(\sum_{j=1}^{n_\mathrm{n}} a_{c|j} n_j \right) \right), \qquad i = 1, \ldots, n_\mathrm{f} \,. \quad (2.37)$$

As n_i goes through the free nodes, at the fixed boundary nodes, Equation (2.37) is identical to zero. Thus the divergence terms of Equation (2.36) vanish, resulting in

$$\int_\gamma \left(\begin{array}{l} - \nu^{k+1} \nabla n_i \cdot \nabla \left(\sum_{j=1}^{n_\mathrm{n}} a_{c|j}^{k+1} n_j \right) - \frac{\sigma}{\beta \Delta t} \left(\sum_{j=1}^{n_\mathrm{n}} a_{c|j}^{k+1} n_j \right) n_i \\ - \frac{(1-\beta)}{\beta} \nu^{k} \nabla n_i \cdot \nabla \left(\sum_{j=1}^{n_\mathrm{n}} a_{c|j}^{k} n_j \right) + \frac{\sigma}{\beta \Delta t} \left(\sum_{j=1}^{n_\mathrm{n}} a_{c|j}^{k} n_j \right) n_i \end{array} \right) \mathrm{d}\gamma = 0, \qquad . \quad (2.38)$$

$$i = 1, \ldots, n_\mathrm{f}$$

By rearranging Equation (2.38), Equation (2.39) is obtained.

$$\int_\gamma \left(\begin{array}{l} \sum_{j=1}^{n_\mathrm{n}} \left(\nu^{k+1} \nabla n_i \cdot \nabla n_j + \frac{\sigma}{\beta \Delta t} n_i n_j \right) a_{c|j}^{k+1} \\ \qquad + \sum_{j=1}^{n_\mathrm{n}} \left(\frac{(1-\beta)}{\beta} \nu^{k} \nabla n_i \cdot \nabla n_j - \frac{\sigma}{\beta \Delta t} n_i n_j \right) a_{c|j}^{k} \end{array} \right) \mathrm{d}\gamma = 0, \quad (2.39)$$

$$i = 1, \ldots, n_\mathrm{f}$$

Introducing terms

$$s_{ij} = \int_{\gamma} \nu^{k+1} \nabla n_i \cdot \nabla n_j \mathrm{d}\gamma \qquad \tilde{s}_{ij} = \int_{\gamma} \frac{(1-\beta)}{\beta} \nu^{k} \nabla n_i \cdot \nabla n_j \mathrm{d}\gamma \tag{2.40}$$

$$t_{ij} = \int_{\gamma} \frac{\sigma}{\beta \Delta t} n_i n_j \mathrm{d}\gamma \qquad \tilde{t}_{ij} = -t_{ij} \tag{2.41}$$

Equation (2.39) can be written in a more compact form

$$\sum_{j=1}^{n_\mathrm{n}} \left(s_{ij}\left(\boldsymbol{a}^{k+1}\right) + t_{ij} \right) a_{c|j}^{k+1} + \sum_{j=1}^{n_\mathrm{n}} \left(\tilde{s}_{ij}\left(\boldsymbol{a}^{k}\right) + \tilde{t}_{ij} \right) a_{c|j}^{k} = 0, \qquad i = 1,\ldots,n_\mathrm{f}\,. \tag{2.42}$$

Newton-Raphson solution of the non-linear equations

If the number of unknowns (that are the free nodal values of a component of magnetic vector potential) is n_f, there are now equally many equations for solving these (Equation (2.42)). In general, a finite element problem that has n_f unknowns and is given in terms of a component of magnetic vector potential can be expressed in brief notation as

$$r_{\mathrm{cc}|i}\left(a_{c|1}^{k+1},\ldots,a_{c|n_\mathrm{f}}^{k+1},a_{c|n_\mathrm{f}+1}^{k+1},\ldots,a_{c|n_\mathrm{n}}^{k+1}\right) = 0, \qquad i = 1,\ldots,n_\mathrm{f} \tag{2.43}$$

in which the subscripts from 1 to n_f denote the free nodes and the subscripts from $n_\mathrm{f} + 1$ to n_n the nodes fixed by boundary conditions. The equations $r_{\mathrm{cc}|i}$ in Equation (2.43) are referred to as residual functions.

By defining a column vector of the nodal values of a component of magnetic vector potential $\boldsymbol{a}_c$ as

$$\boldsymbol{a}_c = \left\{ a_{c|j} \right\}, \qquad j = 1,\ldots,n_\mathrm{n}\,, \tag{2.44}$$

the residual vector consisting of the residual functions $r_{\mathrm{cc}|i}$ can be written as

$$\boldsymbol{r}_{\mathrm{cc}}\left(\boldsymbol{a}_c^{k+1}\right) = 0\,. \tag{2.45}$$

If the problem being considered includes the sources of non-linearities, such as materials that have properties depending on the magnetization, the solution of Equation (2.45) needs to be carried out iteratively as a series of sequential linear tasks. Here, the linearization is done by the Newton-Raphson method. At every iteration $n + 1$, a new estimate for the vector of the nodal values of a component of the magnetic vector potential is obtained by correcting the inaccurate result from the previous iteration n

$$\boldsymbol{a}_c^{k+1|n+1} = \boldsymbol{a}_c^{k+1|n} + \Delta\boldsymbol{a}_c^{k+1|n}. \tag{2.46}$$

The incremental adjustment to be made, $\Delta\boldsymbol{a}_c{}^{k+1|n}$, is determined from the following system of equations

$$\boldsymbol{p}_c\left(\boldsymbol{a}_c^{k+1|n}\right)\Delta\boldsymbol{a}_c^{k+1|n} = -\boldsymbol{r}_{\mathrm{cc}}\left(\boldsymbol{a}_c^{k+1|n}\right) \tag{2.47}$$

in which $\boldsymbol{p}_c$ is the n_f-by-n_n Jacobian matrix of the residual vector $\boldsymbol{r}_{\mathrm{cc}}$.

The Jacobian matrix $\boldsymbol{p}_c$ consists of the derivatives of the residual functions. Its elements can be given as

$$p_{c|lm}\left(\boldsymbol{a}_c^{k+1|n}\right) = \frac{\partial r_{\mathrm{cc}|l}\left(a_{c|1}^{k+1|n},\ldots,a_{c|n_\mathrm{f}}^{k+1|n},a_{c|n_\mathrm{f}+1}^{k+1|n},\ldots,a_{c|n_\mathrm{n}}^{k+1|n}\right)}{\partial a_{c|m}^{k+1|n}}. \tag{2.48}$$

The field in the electrical steel sheets is governed by the two components of the magnetic vector potential that are strongly coupled through the boundary conditions and reluctivity. Thus their solution must be carried out simultaneously in the same system of equations. At the same time, the residual vector of a component of the magnetic vector potential has to be differentiated with respect to the other component as well. Applying the Newton-Raphson iteration scheme to the 1-D eddy current problem yields

$$\begin{bmatrix} \boldsymbol{p}_{xx}\left(\boldsymbol{a}^{k+1|n}\right) & \boldsymbol{p}_{xy}\left(\boldsymbol{a}^{k+1|n}\right) \\ \boldsymbol{p}_{yx}\left(\boldsymbol{a}^{k+1|n}\right) & \boldsymbol{p}_{yy}\left(\boldsymbol{a}^{k+1|n}\right) \end{bmatrix}\begin{bmatrix} \Delta\boldsymbol{a}_x^{k+1|n} \\ \Delta\boldsymbol{a}_y^{k+1|n} \end{bmatrix} = -\begin{bmatrix} \boldsymbol{r}_{\mathrm{cx}}\left(\boldsymbol{a}^{k+1|n}\right) \\ \boldsymbol{r}_{\mathrm{cy}}\left(\boldsymbol{a}^{k+1|n}\right) \end{bmatrix}. \tag{2.49}$$

That is the system of equations to be solved at each iteration n of every time-step $k + 1$.

The elements of the residual vectors of the components of the magnetic vector potential satisfy

$$r_{\mathrm{cx}|i}\left(\boldsymbol{a}^{k+1|n}\right) = \sum_{j=1}^{n_\mathrm{n}}\left(s_{ij}\left(\boldsymbol{a}^{k+1|n}\right) + t_{ij}\right)a_{x|j}^{k+1|n} + \sum_{j=1}^{n_\mathrm{n}}\left(\tilde{s}_{ij}\left(\boldsymbol{a}^{k|n}\right) + \tilde{t}_{ij}\right)a_{x|j}^{k|n} \tag{2.50}$$

and

$$r_{\mathrm{cy}|i}\left(\boldsymbol{a}^{k+1|n}\right) = \sum_{j=1}^{n_\mathrm{n}}\left(s_{ij}\left(\boldsymbol{a}^{k+1|n}\right) + t_{ij}\right)a_{y|j}^{k+1|n} + \sum_{j=1}^{n_\mathrm{n}}\left(\tilde{s}_{ij}\left(\boldsymbol{a}^{k|n}\right) + \tilde{t}_{ij}\right)a_{y|j}^{k|n} \tag{2.51}$$

and the elements of the Jacobian matrices resulting from the differentiation of the residual vectors are, according to Equations (2.48), (2.50), and (2.51),

$$p_{xx|lm}\left(\boldsymbol{a}^{k+1|n}\right) = s_{lm}\left(\boldsymbol{a}^{k+1|n}\right) + t_{lm} + \sum_{j=1}^{n_\mathrm{n}} \frac{\partial s_{lj}\left(\boldsymbol{a}^{k+1|n}\right)}{\partial a_{x|m}^{k+1|n}} a_{x|j}^{k+1|n} \tag{2.52}$$

$$p_{xy|lm}\left(\boldsymbol{a}^{k+1|n}\right) = \sum_{j=1}^{n_\mathrm{n}} \left(\frac{\partial s_{lj}\left(\boldsymbol{a}^{k+1|n}\right)}{\partial a_{y|m}^{k+1|n}} a_{x|j}^{k+1|n} \right) \tag{2.53}$$

$$p_{yx|lm}\left(\boldsymbol{a}^{k+1|n}\right) = \sum_{j=1}^{n_\mathrm{n}} \left(\frac{\partial s_{lj}\left(\boldsymbol{a}^{k+1|n}\right)}{\partial a_{x|m}^{k+1|n}} a_{y|j}^{k+1|n} \right) \tag{2.54}$$

and

$$p_{yy|lm}\left(\boldsymbol{a}^{k+1|n}\right) = s_{lm}\left(\boldsymbol{a}^{k+1|n}\right) + t_{lm} + \sum_{j=1}^{n_\mathrm{n}} \frac{\partial s_{lj}\left(\boldsymbol{a}^{k+1|n}\right)}{\partial a_{y|m}^{k+1|n}} a_{y|j}^{k+1|n} \ . \tag{2.55}$$

Time-harmonic analysis

The field in an electrical machine or even in an electrical steel sheet practically never varies sinusoidally with time. This is due to, for instance, the magnetic non-linearity of iron. If the assumption of sinusoidal time variation is, despite that, made, the electromagnetic field quantities can be represented as phasors and consequently the time-dependence eliminated from the equations to be solved. As a result, a substantial reduction in the computation time is achieved. That is the major reason why the utilization of such a rough simplification is investigated. In the time-harmonic approximation, the phasors of magnetic vector potential and current density for the 1-D eddy current model of electrical steel sheets are given as

$$\underline{\boldsymbol{a}} = \underline{a}_x(z)\boldsymbol{e}_x + \underline{a}_y(z)\boldsymbol{e}_y \tag{2.56}$$

$$\underline{\boldsymbol{j}} = \underline{j}_x(z)\boldsymbol{e}_x + \underline{j}_y(z)\boldsymbol{e}_y \tag{2.57}$$

in which $\underline{a}_x$ and $\underline{a}_y$ and $\underline{j}_x$ and $\underline{j}_y$ are the x- and y-components of the magnetic vector potential and current density. The underscore means that the quantities are complex variables.

From the phasors the time-dependent quantities are obtainable as

$$\boldsymbol{a} = \mathrm{Re}\left\{\underline{\boldsymbol{a}}\mathrm{e}^{\mathrm{j}\omega t}\right\} \tag{2.58}$$

in which ω denotes the angular frequency of the time variation.

The components of the magnetic vector potential fulfill

$$\nabla \cdot \left(|\underline{\nu}| \nabla \underline{a}_x \right) - \mathrm{j}\omega\sigma \underline{a}_x = 0, \quad \nabla \cdot \left(|\underline{\nu}| \nabla \underline{a}_y \right) - \mathrm{j}\omega\sigma \underline{a}_y = 0 \tag{2.59}$$

in which $|\underline{\nu}|$ is the absolute value of complex reluctivity.

Here, the absolute value of complex reluctivity is a quantity equal to the effective value of reluctivity. The effective reluctivity is commonly used to describe the magnetic properties within the time-harmonic approximation (Luomi et al., 1986).

Solving the 1-D field equation (2.59) with non-linear magnetic properties requires an iterative computation. Now, in order to reduce the complexity of the combined 2-D–1-D approach, the magnetic properties of the sheets along their thickness are assumed to be linear. Then, in fact, an analytical solution for the components of the magnetic vector potential can be derived

$$\underline{a}_c = c_1 \mathrm{e}^{\lambda_1 z} + c_2 \mathrm{e}^{\lambda_2 z} \tag{2.60}$$

in which

$$\lambda_1 = \sqrt{\frac{\mathrm{j}\omega\sigma}{|\underline{\nu}|}}, \qquad \lambda_2 = -\sqrt{\frac{\mathrm{j}\omega\sigma}{|\underline{\nu}|}} \tag{2.61}$$

and

$$c_1 = \frac{\underline{a}_c(-d)}{\mathrm{e}^{-d\lambda_1} - \mathrm{e}^{-d\lambda_2}}, \qquad c_2 = \frac{\underline{a}_c(-d)}{-\mathrm{e}^{-d\lambda_1} + \mathrm{e}^{-d\lambda_2}} \tag{2.62}$$

where d denotes half of the thickness of a lamination and $\underline{a}_c(-d)$ the value of the component of the magnetic vector potential at the boundary $-d$.

As the magnetic vector potential is known, the magnetic flux density and current density can be estimated

$$\underline{j}_x = -\mathrm{j}\omega\sigma \underline{a}_x, \quad \underline{j}_y = -\mathrm{j}\omega\sigma \underline{a}_y \tag{2.63}$$

$$\underline{b}_x = -\frac{\mathrm{d}\underline{a}_y}{\mathrm{d}z}, \quad \underline{b}_y = \frac{\mathrm{d}\underline{a}_x}{\mathrm{d}z} \tag{2.64}$$

In spite of the fact that the assumptions exploited enabled analytical expressions for the electromagnetic quantities to be derived, not all the integral terms related to the cou-

pling of the 1-D and 2-D models are analytically attainable. Those terms are solved numerically by the finite difference method and trapezoidal rule.

2.1.2 Two-dimensional–one-dimensional finite element model for cage-induction machines

In this section, the 2-D formulations of the machine model are presented. Both the time-discretized and time-harmonic approaches are considered. In particular, the aim is to elaborate the coupling of the eddy currents in the electrical steel sheets to the 2-D field and winding equations.

Fundamental field and winding equations

As this work concentrates on modeling radial flux rotating electrical machines, the consideration of 3-D electromagnetic fields can be avoided and 2-D ones studied instead. Assuming the machine to be infinitely long in the direction of its shaft, the analysis can be reduced to a study of the plane perpendicular to the shaft. The magnetic vector potential and current density can be defined as

$$\boldsymbol{A} = A_z\left(x,y,t\right)\boldsymbol{e}_z \tag{2.65}$$

$$\boldsymbol{J} = J_z\left(x,y,t\right)\boldsymbol{e}_z \tag{2.66}$$

where $\boldsymbol{e}_z$ denotes the unit vector parallel to the z-axis (and at the same time parallel to the shaft of the machine) and A_z and J_z are the z-components of the magnetic vector potential and current density, respectively.

B-*H* relations

The solution region, i.e., the cross-section of an electrical machine, contains materials exhibiting different magnetic properties. A division into magnetically linear, non-linear, and hysteretic ones can be made. The air and stator and rotor winding parts are magnetically linear and have a relative permeability equal to that of free space. The solid shaft of a machine is commonly described with a single-valued magnetization curve. The stator and rotor core are constructed of electrical steel sheets. In a 2-D analysis, such a core structure is typically modeled as a non-conducting medium with a single-valued magnetization curve. Hence, both the hysteresis and eddy currents in the electrical steel sheets are neglected.

The ***B*-*H*** relation for the air and winding parts of the model geometry is given as

$$\boldsymbol{B} = \mu_0 \boldsymbol{H} \quad \text{or} \quad \boldsymbol{H} = \nu_0 \boldsymbol{B} \tag{2.67}$$

in which ν_0 denotes the reluctivity of free space.

For the shaft of the machine, the magnetic constitutive relation is

$$\boldsymbol{B} = \mu \boldsymbol{H} \quad \text{or} \quad \boldsymbol{H} = \nu \boldsymbol{B} \tag{2.68}$$

in which μ or its inverse ν is a single-valued non-linear function of the square of the magnetic flux density.

The eddy currents in electrical steel sheets are now contained in the analysis. As usual, the electrical conductivity of the sheets in the equations of the 2-D plane is set to be equal to zero. The ***B*-*H*** relations are used to couple the 1-D eddy current solution with the 2-D field analysis. As the approach discussed in (Henrotte et al., 1992) is applied, the constitutive law in the electrical steel sheets is defined as

$$\boldsymbol{h} = \nu \boldsymbol{B} + \boldsymbol{H}_\mathrm{c} \tag{2.69}$$

The first term on the right-hand side depicts the dependency of $\boldsymbol{h}$ on $\boldsymbol{B}$ when the eddy currents in the sheets are not included. The reluctivity in Equation (2.69) is given as a single-valued non-linear function of the square of the magnetic flux density. The second term on the right-hand side, $\boldsymbol{H}_\mathrm{c}$, represents the correction to be made to the component $\nu\boldsymbol{B}$ in order to obtain the magnetic field strength $\boldsymbol{h}$ imposed by the 1-D eddy current solution. The section entitled "Definition of H_c" discusses the components of the constitutive law in detail.

Definition of current density in windings

Under the 2-D approximation of the fields, the electric scalar potential in a straight solid conductor parallel to the z-axis must be a linear function of the z-coordinate. Hence, the gradient of the electric scalar potential fulfills

$$\nabla \phi = \frac{\partial \phi}{\partial z} \boldsymbol{e}_z = \frac{\Delta \phi}{l_\mathrm{b}} \boldsymbol{e}_z = -\frac{u_\mathrm{b}}{l_\mathrm{b}} \boldsymbol{e}_z \tag{2.70}$$

in which l_b denotes the length of the conductor and u_b the voltage over the conductor. Substituting Equations (2.65), (2.66), and (2.70) in Equation (2.14) yields

$$J_{zb} = -\sigma \frac{\partial A_z}{\partial t} + \sigma \frac{u_b}{l_b} . \tag{2.71}$$

Equation (2.71) is applied for determining the current density in the bars of the squirrel-cage rotor winding. The same expression could also be used for the coil sides of the stator phase winding. This would, however, lead to computationally very expensive models as a result of the large number of thin conductors in each of the stator slots. In most cases, neglecting the skin effect in the stator-winding conductors is justified, thus enabling the current density in a coil side of a phase winding J_{zcw} to be defined as

$$J_{zcw} = \frac{N_{cw} i_w}{S_{cw}} \tag{2.72}$$

in which N_{cw} denotes the number of turns in series in a coil side of a phase winding, i_w the current in a phase winding, and S_{cw} the cross-section area of a coil side of a phase winding.

Summary of field equations

The field equations in different parts of the solution region can be summarized as follows:

$$-\nabla \cdot \left(\nu \nabla A_z \right) = \left\{ \begin{array}{cc} 0 & \text{in air} \\ \dfrac{N_{cw} i_w}{S_{cw}} & \text{in phase windings} \\ -\sigma \dfrac{\partial A_z}{\partial t} + \sigma \dfrac{u_b}{l_b} & \text{in rotor bars} \\ -\sigma \dfrac{\partial A_z}{\partial t} & \text{in rotor shaft} \\ -\left(\nabla \times \boldsymbol{H}_c \right)_z & \text{in laminated iron} \end{array} \right\} . \tag{2.73}$$

The field in the air is derived from Equations (2.11) and (2.67). In a stator phase winding, Equations (2.11), (2.67), and (2.72) are utilized and in a squirrel-cage rotor winding Equations (2.11), (2.67), and (2.71). The field equation of a rotor shaft is defined from Equations (2.16) and (2.68). In the shaft the electric scalar potential is zero. The equation for the laminated iron is determined on the basis of Equations (2.11) and (2.69).

Winding equations

The computational algorithm that is applied performs a coupled solution of the field and winding equations of the cage-induction machine. The expressions for the circuit equations of the stator and rotor windings of the cage-induction machine are briefly presented next. In the formulation of the stator phase winding, an additional end-winding inductance is included in order to approximate the effects of the end-winding in the machine. For the squirrel-cage rotor winding, the voltage equations of the bars and end-rings are presented.

A stator phase winding consists of several coils that are connected in series and distributed in the stator slots of the machine. Naturally, the formulae to be presented would be valid for a phase winding in the rotor as well. A part of the coil sides of a phase winding is positively oriented and a part negatively oriented. This can be compactly expressed as

$$\beta_{\mathrm{w}|n}(x,y)=\begin{cases}\dfrac{N_{\mathrm{cw}|n}}{S_{\mathrm{cw}|n}} & \text{in positively oriented coil sides of a phase winding } n\\ -\dfrac{N_{\mathrm{cw}|n}}{S_{\mathrm{cw}|n}} & \text{in negatively oriented coil sides of a phase winding } n\\ 0 & \text{otherwise}\end{cases}. \tag{2.74}$$

According to circuit theory, the voltage of a phase winding is the sum of the voltage drop in its resistance and the time derivative of its flux linkage. The flux linkage now consists of two terms. The first term is imposed by the 2-D field solution as a surface integral of the time derivative of the magnetic vector potential over the coil sides of the phase winding. The second term is the one related to the end-winding inductance. Hence, when it is assumed that the number of parallel paths in the phase winding is one and that the number of poles in the solution region is an integer, the voltage equation of a phase winding n in the entire solution region fulfills (Arkkio, 1987)

$$u_{\mathrm{w}|n}=N_{\mathrm{s}}l_{\mathrm{ef}}\int_{\Omega}\beta_{\mathrm{w}|n}\frac{\partial \boldsymbol{A}}{\partial t}\cdot\mathrm{d}\boldsymbol{\Omega}+R_{\mathrm{w}}i_{\mathrm{w}|n}+L_{\mathrm{ew}}\frac{\mathrm{d}i_{\mathrm{w}|n}}{\mathrm{d}t} \tag{2.75}$$

in which $u_{\mathrm{w}|n}$ denotes the voltage over the phase winding n, N_{s} the number of symmetry sectors in the machine being studied, l_{ef} the length of the iron core of the machine, Ω the area of the whole solution region, R_{w} the DC resistance of each of the phase windings, also including the end region, $i_{\mathrm{w}|n}$ the current in a phase winding n, and L_{ew} the end-winding inductance approximating the 3-D effects of the part of the phase winding outside the iron core.

For each of the bars in the squirrel-cage winding, a voltage equation of its own is applied. The voltage equation of a bar can be derived from its current density given by Equation (2.71). Integrating the current density Equation (2.71) of a bar over its cross-section area yields (Arkkio, 1987)

$$i_{\mathrm{b}|n} = -\int_{S_\mathrm{b}} \sigma \frac{\partial \boldsymbol{A}}{\partial t} \cdot \mathrm{d}\boldsymbol{S} + u_{\mathrm{b}|n} \frac{1}{l_\mathrm{b}} \int_{S_\mathrm{b}} \sigma \mathrm{d}S \tag{2.76}$$

in which $i_{\mathrm{b}|n}$ denotes the current in the bar n and S_b the cross-section area of each of the bars.

If the conductivity and cross-section area of the bars are constant, their voltage equations in the entire solution region fulfill (Arkkio, 1987), (Kanerva, 2005)

$$u_{\mathrm{b}|n} = R_\mathrm{b} i_{\mathrm{b}|n} + L_\mathrm{eb} \frac{\mathrm{d}i_{\mathrm{b}|n}}{\mathrm{d}t} + R_\mathrm{b} \int_\Omega \beta_{\mathrm{b}|n} \sigma \frac{\partial \boldsymbol{A}}{\partial t} \cdot \mathrm{d}\boldsymbol{\Omega} \tag{2.77}$$

in which $u_{\mathrm{b}|n}$ is the voltage over a bar n, R_b is the resistance of each of the bars, including the end region outside the iron core of the machine, L_eb is the inductance of the bar ends outside the iron core of the machine, and $\beta_{\mathrm{b}|n}$ is defined as

$$\beta_{\mathrm{b}|n}(x, y) = \begin{cases} 1 & \text{in a bar } n \\ 0 & \text{otherwise} \end{cases}. \tag{2.78}$$

In both the ends of the rotor core, the rotor bars are connected to each other by a short-circuiting ring. The voltage of the short-circuiting ring $u_{\mathrm{er}|n}$ associated with the bar n fulfills (Arkkio, 1987), (Kanerva, 2005)

$$u_{\mathrm{er}|n} = R_{\mathrm{er}|n} i_{\mathrm{er}|n} + L_{\mathrm{er}|n} \frac{\mathrm{d}i_{\mathrm{er}|n}}{\mathrm{d}t} \tag{2.79}$$

where R_er and L_er denote the resistance and inductance and i_er the current of the short-circuiting ring associated with the bar n. A detailed discussion of the model of the cage winding can be found from (Arkkio, 1987).

Transient time-discretized analysis

When all the rotor bars and phases of the stator winding are taken into account, the partial differential equation of the 2-D electromagnetic field in an electrical machine based on Equations (2.73), (2.74), and (2.78) can be written as

$$-\nabla\cdot\left(\nu\nabla A_z\right)+\sigma\frac{\partial A_z}{\partial t}-\frac{1}{l_\mathrm{b}}\sum_{n=1}^{Q_\mathrm{b}}\sigma\beta_{\mathrm{b}|n}u_{\mathrm{b}|n}-\sum_{n=1}^{m}\beta_{\mathrm{w}|n}i_{\mathrm{w}|n}+\left(\nabla\times\boldsymbol{H}_\mathrm{c}\right)_z=0 \tag{2.80}$$

in which Q_b denotes the number of rotor bars in the solution region and m the number of phases in the stator winding.

In the field equation (2.80) there are four unknowns: the magnetic vector potential, the voltages of the rotor bars, the phase currents of the stator winding, and the additional term as a result of the inclusion of the eddy currents in the electrical steel sheets. Defining these unknowns requires a coupled solution of the 2-D field and winding equations and the 1-D eddy current model.

When the true time-dependence of the 2-D quantities is of interest, a time-stepping analysis needs to be performed. The 2-D problem is discretized in a similar way to the 1-D eddy current model by utilizing the backward Euler and finite element method. The linearization of the resulting non-linear equations is accomplished by the Newton-Raphson method.

Time-discretization

The expressions needed for the time-discretization of the 2-D equations are

$$A_z^{k+1}=A_z^k+\left[\beta\frac{\partial A_z}{\partial t}\Big|^{k+1}+\left(1-\beta\right)\frac{\partial A_z}{\partial t}\Big|^{k}\right]\Delta t\,, \tag{2.81}$$

$$i_{\mathrm{w/b}|n}^{k+1}=i_{\mathrm{w/b}|n}^{k}+\left[\beta\frac{\mathrm{d}i_{\mathrm{w/b}|n}}{\mathrm{d}t}\Big|^{k+1}+\left(1-\beta\right)\frac{\mathrm{d}i_{\mathrm{w/b}|n}}{\mathrm{d}t}\Big|^{k}\right]\Delta t\,. \tag{2.82}$$

The field or winding equation of the 2-D model is first written at the time-steps k and $k + 1$. The expression at the time-step k is then multiplied by $1 - \beta$ and at the time-step $k + 1$ by β. Summing the two resultants together yields an expression of which the time derivatives can be approximated by Equations (2.81) and (2.82). The time-discretization of the 2-D electromagnetic field equation (2.80) gives

$$
\begin{aligned}
&-\nabla\cdot\left(\nu^{k+1}\nabla A_z^{k+1}\right)+\frac{\sigma}{\beta\Delta t}A_z^{k+1}\\
&-\frac{1}{l_\mathrm{b}}\sum_{n=1}^{Q_\mathrm{b}}\sigma\beta_{\mathrm{b}|n}u_{\mathrm{b}|n}^{k+1}-\sum_{n=1}^{m}\beta_{\mathrm{w}|n}i_{\mathrm{w}|n}^{k+1}+\left(\nabla\times\boldsymbol{H}_\mathrm{c}^{k+1}\right)_z\\
&-\frac{(1-\beta)}{\beta}\nabla\cdot\left(\nu^{k}\nabla A_z^{k}\right)-\frac{\sigma}{\beta\Delta t}A_z^{k}\\
&-\frac{(1-\beta)}{\beta}\frac{1}{l_\mathrm{b}}\sum_{n=1}^{Q_\mathrm{b}}\sigma\beta_{\mathrm{b}|n}u_{\mathrm{b}|n}^{k}-\frac{(1-\beta)}{\beta}\sum_{n=1}^{m}\beta_{\mathrm{w}|n}i_{\mathrm{w}|n}^{k}+\frac{(1-\beta)}{\beta}\left(\nabla\times\boldsymbol{H}_\mathrm{c}^{k}\right)_z=0
\end{aligned}
\qquad (2.83)
$$

For the sake of simplicity, the derivations concerning the approximation of the time derivatives of the winding equations are not presented here. See (Arkkio, 1987), (Islam, 2010) for these.

Space-discretization

The space-discretized formulation of the 2-D problem is produced by the finite element method in association with Galerkin's method. Only the smallest symmetry sector of the cross-sectional geometry of the application being studied is considered; this is meshed with either first- or second-order triangular elements (Arkkio, 1987). The nodal values of the magnetic vector potential on the symmetry boundaries are enforced by proper periodicity constraints. On the rest of the boundary, the Dirichlet boundary conditions are imposed. The values of the magnetic vector potential of the free nodes need to be solved.

By approximating the 2-D magnetic vector potential as

$$
A_z\cong\sum_{j=1}^{N_\mathrm{n}}A_{z|j}N_j\left(x,y\right) \qquad (2.84)
$$

and repeating the mathematical steps presented in the case of the 1-D model, the 2-D field in the free nodes *i* can be expressed as

$$\int_{\Omega}\left(\begin{array}{l}\displaystyle\sum_{j=1}^{N_\mathrm{n}}\left(\nu^{k+1}\nabla N_i\cdot\nabla N_j+\frac{\sigma}{\beta\Delta t}N_iN_j\right)A_{z|j}^{k+1}\\ \displaystyle-\left(N_i\frac{1}{l_\mathrm{b}}\sum_{n=1}^{Q_\mathrm{b}}\sigma\beta_{\mathrm{b}|n}u_{\mathrm{b}|n}^{k+1}+N_i\sum_{n=1}^{m}\beta_{\mathrm{w}|n}i_{\mathrm{w}|n}^{k+1}\right)\\ \qquad\qquad+\left(\boldsymbol{H}_\mathrm{c}^{k+1}\times\nabla N_i\right)_z\\ \displaystyle+\sum_{j=1}^{N_\mathrm{n}}\left(\frac{(1-\beta)}{\beta}\nu^{k}\nabla N_i\cdot\nabla N_j-\frac{\sigma}{\beta\Delta t}N_iN_j\right)A_{z|j}^{k}\\ \displaystyle-\left(N_i\frac{(1-\beta)}{\beta}\frac{1}{l_\mathrm{b}}\sum_{n=1}^{Q_\mathrm{b}}\sigma\beta_{\mathrm{b}|n}u_{\mathrm{b}|n}^{k}+N_i\frac{(1-\beta)}{\beta}\sum_{n=1}^{m}\beta_{\mathrm{w}|n}i_{\mathrm{w}|n}^{k}\right)\\ \qquad\qquad+\dfrac{(1-\beta)}{\beta}\left(\boldsymbol{H}_\mathrm{c}^{k}\times\nabla N_i\right)_z\end{array}\right)\mathrm{d}\Omega=0,\qquad i=1,\ldots,N_\mathrm{f}\qquad,\qquad(2.85)$$

in which $A_{z|j}$ denotes the component of the magnetic vector potential connected to the node j of the finite element mesh, N_j the shape function of the node j of the finite element mesh, and N_n the number of nodes in the finite element mesh. The shape functions N_j are either first- or second-order polynomials, depending on the degree of the finite elements applied. The index i runs from 1 to the number of free nodes in the 2-D finite element mesh denoted by N_f.

Just as their time-discretization was not, neither is the finite element approximation of the winding equations considered in detail for the sake of clarity. Comprehensive discussion on the topic has been provided in, for instance, (Arkkio, 1987), (Kanerva, 2005), and (Islam, 2010).

Newton-Raphson solution of the non-linear equations

The 2-D machine model is governed by the residual vectors of the field and windings that are connected with each other. When all the possible connections of the phase windings and the cage windings as a whole are taken into consideration, those vectors can be represented as

$$\begin{aligned}\boldsymbol{r}_\mathrm{f}\left(\boldsymbol{A}_z^{k+1},\boldsymbol{u}_\mathrm{b}^{k+1},\boldsymbol{i}_\mathrm{w}^{k+1}\right)&=\left(\boldsymbol{S}\left(\boldsymbol{A}_z^{k+1}\right)+\boldsymbol{T}\right)\boldsymbol{A}_z^{k+1}+\boldsymbol{D}_\mathrm{b}^\mathrm{T}\boldsymbol{u}_\mathrm{b}^{k+1}+\boldsymbol{D}_\mathrm{w}^\mathrm{T}\boldsymbol{K}^\mathrm{T}\boldsymbol{i}_\mathrm{w}^{k+1}\\&\quad+\left\{\left(\tilde{\boldsymbol{S}}\left(\boldsymbol{A}_z^{k}\right)+\tilde{\boldsymbol{T}}\right)\boldsymbol{A}_z^{k}+\tilde{\boldsymbol{D}}_\mathrm{b}^\mathrm{T}\boldsymbol{u}_\mathrm{b}^{k}+\tilde{\boldsymbol{D}}_\mathrm{w}^\mathrm{T}\boldsymbol{K}^\mathrm{T}\boldsymbol{i}_\mathrm{w}^{k}+\boldsymbol{E}_\mathrm{c}^{k+1}+\boldsymbol{E}_\mathrm{c}^{k}\right\}=0\end{aligned}\qquad(2.86)$$

$$\boldsymbol{r}_\mathrm{b}\left(\boldsymbol{A}_z^{k+1},\boldsymbol{u}_\mathrm{b}^{k+1}\right)=\boldsymbol{D}_\mathrm{b}\boldsymbol{A}_z^{k+1}+\boldsymbol{C}_\mathrm{b}\boldsymbol{u}_\mathrm{b}^{k+1}+\left\{-\boldsymbol{D}_\mathrm{b}\boldsymbol{A}_z^{k}+\boldsymbol{C}_\mathrm{b}\boldsymbol{u}_\mathrm{b}^{k}+\boldsymbol{G}_\mathrm{b}\boldsymbol{i}_\mathrm{b}^{k}\right\}=0\qquad(2.87)$$

$$\boldsymbol{r}_{\mathrm{w}}\left(\boldsymbol{A}_z^{k+1},\boldsymbol{i}_{\mathrm{w}}^{k+1}\right)=\boldsymbol{K}\boldsymbol{D}_{\mathrm{w}}\boldsymbol{A}_z^{k+1}+\boldsymbol{G}_{\mathrm{w}}\boldsymbol{i}_{\mathrm{w}}^{k+1}+\left\{-\boldsymbol{K}\boldsymbol{D}_{\mathrm{w}}\boldsymbol{A}_z^{k}+\boldsymbol{H}_{\mathrm{w}}\boldsymbol{i}_{\mathrm{w}}^{k}+\boldsymbol{C}_{\mathrm{w}}\left(\boldsymbol{u}_{\mathrm{w}}^{k+1}+\boldsymbol{u}_{\mathrm{w}}^{k}\right)\right\}=0 \quad (2.88)$$

in which $\boldsymbol{A}_z$ denotes the vector of nodal values of the magnetic vector potential, $\boldsymbol{u}_{\mathrm{b}}$ the vector of the rotor-bar voltages, $\boldsymbol{i}_{\mathrm{b}}$ the vector of the rotor-cage currents, $\boldsymbol{u}_{\mathrm{w}}$ the vector of the stator-phase voltages, and $\boldsymbol{i}_{\mathrm{w}}$ the vector of the stator-phase currents. $\boldsymbol{K}$ is the stator-winding connection matrix, and $\boldsymbol{C}_{\mathrm{b}}$, $\boldsymbol{G}_{\mathrm{b}}$, $\boldsymbol{C}_{\mathrm{w}}$, $\boldsymbol{G}_{\mathrm{w}}$, and $\boldsymbol{H}_{\mathrm{w}}$ denote the circuit matrices of the rotor and stator windings. The definitions of the connection and circuit matrices as well as those of the short notations can be found from (Arkkio, 1987), (Kanerva, 2005), and (Islam, 2010). The superscript T denotes a transpose of a matrix. The elements of the vectors $\boldsymbol{E}_{\mathrm{c}}$ and $\tilde{\boldsymbol{E}}_{\mathrm{c}}$ satisfy

$$E_{\mathrm{c}|i}=\int_{\Omega}\left(\boldsymbol{H}_{\mathrm{c}}^{k+1}\times\nabla N_i\right)_z\,\mathrm{d}\Omega \qquad \tilde{E}_{\mathrm{c}|i}=\frac{(1-\beta)}{\beta}\int_{\Omega}\left(\boldsymbol{H}_{\mathrm{c}}^{k}\times\nabla N_i\right)_z\,\mathrm{d}\Omega\,. \quad (2.89)$$

The solution of the non-linear problem is carried out in the Newton-Raphson iterative scheme. Following the derivations presented for the 1-D model, a system of equations from which the incremental adjustment to be made to the 2-D variables at every iteration step n can be obtained

$$\begin{bmatrix}\boldsymbol{P}\left(\boldsymbol{A}_z^{k+1|n}\right) & \boldsymbol{D}_{\mathrm{b}}^{\mathrm{T}} & \boldsymbol{D}_{\mathrm{w}}^{\mathrm{T}}\boldsymbol{K}^{\mathrm{T}}\\ \boldsymbol{D}_{\mathrm{b}} & \boldsymbol{C}_{\mathrm{b}} & 0\\ \boldsymbol{K}\boldsymbol{D}_{\mathrm{w}} & 0 & \boldsymbol{G}_{\mathrm{w}}\end{bmatrix}\begin{bmatrix}\Delta\boldsymbol{A}_z^{k+1|n}\\ \Delta\boldsymbol{u}_{\mathrm{b}}^{k+1|n}\\ \Delta\boldsymbol{i}_{\mathrm{w}}^{k+1|n}\end{bmatrix}=-\begin{bmatrix}\boldsymbol{r}_{\mathrm{f}}\left(\boldsymbol{A}_z^{k+1|n},\boldsymbol{u}_{\mathrm{b}}^{k+1|n},\boldsymbol{i}_{\mathrm{w}}^{k+1|n}\right)\\ \boldsymbol{r}_{\mathrm{b}}\left(\boldsymbol{A}_z^{k+1|n},\boldsymbol{u}_{\mathrm{b}}^{k+1|n}\right)\\ \boldsymbol{r}_{\mathrm{w}}\left(\boldsymbol{A}_z^{k+1|n},\boldsymbol{i}_{\mathrm{w}}^{k+1|n}\right)\end{bmatrix}. \quad (2.90)$$

The elements of the N_{f}-by-N_{n} Jacobian matrix $\boldsymbol{P}(\boldsymbol{A}_z^{k+1|n})$ satisfy

$$P_{lm}\left(\boldsymbol{A}_z^{k+1|n}\right)=S_{lm}\left(\boldsymbol{A}_z^{k+1|n}\right)+T_{lm}+\sum_{j=1}^{N_{\mathrm{n}}}\frac{\partial S_{lj}\left(\boldsymbol{A}_z^{k+1|n}\right)}{\partial A_{z|m}^{k+1|n}}A_{z|j}^{k+1|n}\,. \quad (2.91)$$

The vector $\boldsymbol{E}_{\mathrm{c}}$ which is associated with the eddy currents in electrical steel sheets depends on the magnetization. The Jacobian matrix, however, is formulated with the terms originating from that being omitted. The Newton-Raphson iterative scheme is thus referred to be applied in an incomplete manner. A complete formulation of the Jacobian matrix in a case similar to this is presented in (Bergqvist, 1994). The convergence of the computation is assured by under-relaxation, meaning that the unknowns from a previous iteration are corrected as (Janicke and Kost, 1998)

$$\boldsymbol{A}_z^{k+1|n+1}=\boldsymbol{A}_z^{k+1|n}+\chi\Delta\boldsymbol{A}_z^{k+1|n} \quad (2.92)$$

in which χ is the relaxation factor.

Definition of H_c

The magnetic constitutive law in the laminated parts of the 2-D cross-section geometry is given by Equation (2.69). The term $\boldsymbol{H}_c$ is used to represent the eddy currents in the steel laminations. An illustration of the components of the magnetic field strength $\boldsymbol{h}$ and their dependencies is presented in Figure 2.2. The actual value of the magnetic field strength $\boldsymbol{h}$ is now the one obtained through the 1-D eddy current modeling at the boundary of the sheets ($z = -d$ or equally $z = d$). The component $\nu\boldsymbol{B}$ corresponds to the value of the magnetic field strength when the eddy currents in the steel sheets are omitted. Last, $\boldsymbol{H}_c$ is the difference between the actual $\boldsymbol{h}$ and $\nu\boldsymbol{B}$. For the inclusion of the eddy currents, the term $\boldsymbol{H}_c$ is required. Its value fulfils

$$\boldsymbol{H}_c(x,y,t) = \boldsymbol{h}(-d,t) - \nu\boldsymbol{B}(x,y,t) \tag{2.93}$$

in which the reluctivity ν is given as a single-valued function of the square of the magnetic flux density $(\boldsymbol{B}(x,y,t))^2$.

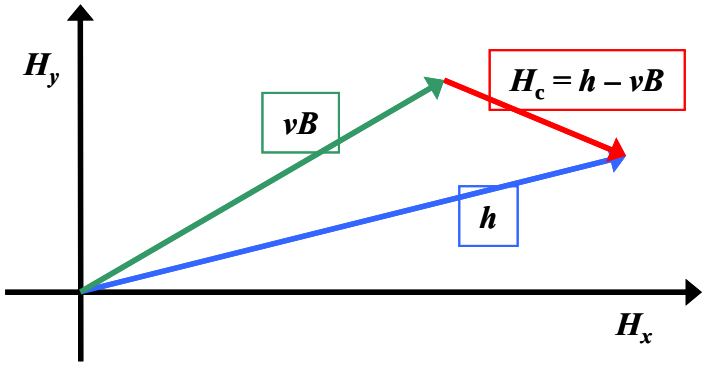

Figure 2.2 Illustration of the magnetic field strength and its components.

Two approaches for the estimation of the magnetic field strength at the boundary of the sheets, $\boldsymbol{h}(-d,t)$, are proposed. First, one can calculate $\boldsymbol{h}(-d,t)$ as a product of the magnetic flux density at the boundary of the sheets $\boldsymbol{b}(-d,t)$ and the corresponding reluctivity $\nu(-d,t)$ (Equation (2.8)). These values of the magnetic flux density and reluctivity are then evaluated from the distribution of the 1-D magnetic vector potential by means of the shape functions. The approach described above is henceforth referred to as *conventional*.

On the other hand, an expression for $\boldsymbol{h}(-d,t)$ can be derived from the Ampère's circuital law (2.2). Then the x- and y-components of $\boldsymbol{h}(-d,t)$ become defined as

$$h_x(-d,t) = -\int_{-d}^{z_i} j_y(z,t)\,\partial z + h_x(z_i,t) \tag{2.94}$$

$$h_y\left(-d,t\right)=\int_{-d}^{z_\mathrm{i}} j_x\left(z,t\right)\partial z+h_y\left(z_\mathrm{i},t\right) \tag{2.95}$$

in which z_i is the upper integration bound, $h_x(z_\mathrm{i},t)$ and $h_y(z_\mathrm{i},t)$ are the values of the components of the magnetic field strength at the upper integration bound. The value of $\boldsymbol{h}(z_\mathrm{i},t)$ is evaluated in the traditional manner as a product of $\boldsymbol{b}(z_\mathrm{i},t)$ and $\nu(z_\mathrm{i},t)$. The choice of a proper upper integration bound is discussed in detail in the section "Choosing a proper upper integration bound for the *integration* approach". The method expressed by Equations (2.94) and (2.95) is henceforth referred to as *integration*.

Analysis of the coupling techniques

This section clarifies the difference between the two coupling techniques that are considered by means of a simple example. As discussed above, there exists an analytical expression for the field in the sheets if their reluctivity is supposed to be independent of the magnetization. Indeed, that solution is given by Equations (2.58) and (2.60). Let us next analyze this linearized problem in one *x*-*y* point of the 2-D space by feeding it with a unidirectional, sinusoidally varying magnetic flux density having a frequency of 50 Hz and an amplitude of 1 T. The relative permeability of the sheets is set to 1000 H/m, with their conductivity and thickness being 2.5 MS/m and 0.65 mm, respectively. Besides analytically, the same problem is solved numerically showing the resulting estimates of the magnetic field strength at the boundary of the sheets for both the *conventional* and *integration* method. The 1-D finite element mesh that covers half of the thickness of the sheets is consisted of nine first-order elements and during each computation, three periods (altogether 1200 time-steps) are completed.

The main results of the investigation are illustrated in Figures 2.3 and 2.4 and in Table I. First, Figure 2.3 and Table I pursue to elaborate the evaluation of $\boldsymbol{h}(-d,t)$ within the *integration* method during one instant. The eddy current density in the half of the lamination thickness is shown in Figure 2.3. Integrating this current density over the whole solution sector, z_i thus being 0, results in the value referred to as "Integral" in Table I. The other part of the definition of $\boldsymbol{h}(-d,t)$, i.e. here $h_y(z_\mathrm{i},t)$, is furthermore referred to as "Value at the upper integration bound" and is calculated traditionally as a product of the magnetic flux density and reluctivity. Last, the result of the *integration* approach that is, according to Equation (2.95) the sum of the two aforementioned components, is simply referred to as "Result" in Table I. Clearly, the term $h_y(z_\mathrm{i},t)$ is the dominant part while the integral of the current density only provides a small correction to the final result.

A comparison of the analytical and numerical solutions of the magnetic field strength in the thickness of the sheets as well as of the associated results from the two coupling approaches is presented in Figure 2.4. These results are again obtained at one instant. As Figure 2.4 shows, the first-order elements produce a rather rough estimate for the distribution of the magnetic field strength in the thickness of the sheets in comparison with the analytical solution; the relative difference between the values at the boundary from

the *conventional* and analytical approaches is on average 2.6%. Besides by means of higher-order elements, the correspondence between the analytical and numerical estimates can, apparently, be notably improved by employing the *integration* approach, the relative difference then being on average 0.1%.

The usefulness of the *integration* approach stems from two factors. First, its integral term is calculated from the current density the solution of which is accurate. Second, by choosing the upper integration bound suitably, the direct consideration of the field strength in the vicinity of the boundary can be avoided. This is rather beneficial since, as seen from Figure 2.4, the changes in the field distribution are not that abrupt in the

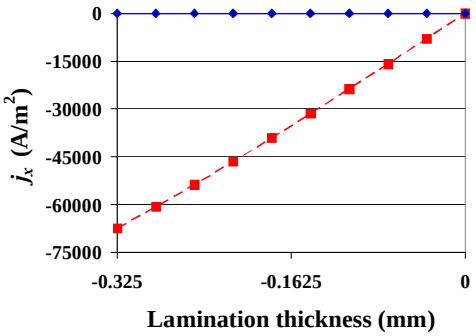

Figure 2.3 Numerical solution of eddy current density in the half of the lamination thickness (red curve) at one instant. Blue curve illustrates the 1-D mesh with its nodes depicted by diamond shapes.

*Table I Example of the magnitudes of the components composing the outcome of the integration approach, **h**(–d,t), at one instant.*

Integral (A/m)	11.6
Value at the upper integration bound (A/m)	763.7
Result, $h_y(-d,t)$ (A/m)	775.3

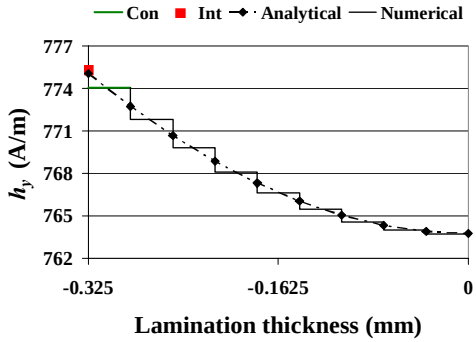

Figure 2.4 Comparison of values of magnetic field strength at one instant. Con and Int refer to the final results of the conventional and integration approaches, respectively. Analytical and numerical results are plotted with a dashed and a solid line, respectively.

middle of the sheets and therefore can be traced even with the first-order elements with sufficient accuracy.

Time-harmonic analysis

The approximation of sinusoidal time variation offers a greatly simplified manner to study electrical machines and hence its utilization is investigated. In the analysis, the stator quantities are assumed to vary with the supply frequency f_s. The actual movement of the rotor cannot be taken into account, but it is approximated by employing the slip frequency sf_s, denoting the slip by s for the rotor-side quantities. Under such assumptions, the 2-D problem can be formulated using phasor variables and the time-dependence eliminated from the equations. The phasors of the magnetic vector potential and current density are

$$\underline{\boldsymbol{A}} = \underline{A}_z\left(x, y\right)\boldsymbol{e}_z \tag{2.96}$$

$$\underline{\boldsymbol{J}} = \underline{J}_z\left(x, y\right)\boldsymbol{e}_z . \tag{2.97}$$

The time-dependence of the quantities can be worked out as

$$\boldsymbol{A} = \mathrm{Re}\left\{\underline{\boldsymbol{A}}_z \mathrm{e}^{\mathrm{j}\omega t}\right\} \tag{2.98}$$

$$\boldsymbol{J} = \mathrm{Re}\left\{\underline{\boldsymbol{J}}_z \mathrm{e}^{\mathrm{j}\omega t}\right\} . \tag{2.99}$$

The magnetic properties of the sheets are modeled by a complex reluctivity. This definition involves both the eddy current and hysteresis of ferromagnetic materials. In the other parts of the machine geometry, the effective reluctivity is employed (Luomi et al., 1986). The equation governing the cross-sectional field in a cage-induction machine under the time-harmonic approximation satisfies

$$-\nabla\cdot\left(\underline{\nu}\nabla\underline{A}_z\right) + \mathrm{j}s\omega\sigma\underline{A}_z - \frac{1}{l_\mathrm{b}}\sum_{n=1}^{\underline{Q}_\mathrm{b}}\sigma\beta_{\mathrm{b}|n}\underline{u}_{\mathrm{b}|n} - \sum_{n=1}^{m}\beta_{\mathrm{w}|n}\underline{i}_{\mathrm{w}|n} = 0 . \tag{2.100}$$

In the stator parts of the machine geometry, the slip equals to 1. For the rest of the parts, except for the steel sheets, the complex reluctivity is replaced by the effective reluctivity.

Space-discretization

Similarly as in the time-discretized approach, the differential equations of the field and windings are converted into a numerical form by means of the finite elements and

Galerkin's method. Utilizing the finite element approximation of the magnetic vector potential

$$\underline{A}_z \cong \sum_{j=1}^{N_\mathrm{n}} \underline{A}_{z|j} N_j(x,y) \tag{2.101}$$

and carrying out some mathematical manipulations yields

$$\int_\Omega \left(\begin{array}{l} \displaystyle\sum_{j=1}^{N_\mathrm{n}} \left(\underline{\nu} \nabla N_i \cdot \nabla N_j + \mathrm{j}s\omega\sigma N_i N_j \right) \underline{A}_{z|j} \\ \displaystyle -\left(N_i \frac{1}{l_\mathrm{b}} \sum_{n=1}^{Q_\mathrm{b}} \sigma\beta_{\mathrm{b}|n} \underline{u}_{\mathrm{b}|n} + N_i \sum_{n=1}^{m} \beta_{\mathrm{w}|n} \underline{i}_{\mathrm{w}|n} \right) \end{array} \right) \mathrm{d}\Omega = 0 \qquad i = 1,\ldots,N_\mathrm{f} \tag{2.102}$$

Newton-Raphson solution of the non-linear equations

The system of equations representing the 2-D machine model with the assumption of sinusoidal time variation is in the form of residual vectors

$$\boldsymbol{r}_\mathrm{f}\left(\underline{\boldsymbol{A}}_z, \underline{\boldsymbol{u}}_\mathrm{b}, \underline{\boldsymbol{i}}_\mathrm{w}\right) = \underline{\boldsymbol{S}}\left(\underline{\boldsymbol{A}}_z\right)\underline{\boldsymbol{A}}_z + \boldsymbol{D}_\mathrm{b}^\mathrm{T}\underline{\boldsymbol{u}}_\mathrm{b} + \boldsymbol{D}_\mathrm{w}^\mathrm{T}\boldsymbol{K}^\mathrm{T}\underline{\boldsymbol{i}}_\mathrm{w} = 0 \tag{2.103}$$

$$\boldsymbol{r}_\mathrm{b}\left(\underline{\boldsymbol{A}}_z, \underline{\boldsymbol{u}}_\mathrm{b}\right) = \boldsymbol{D}_\mathrm{b}\underline{\boldsymbol{A}}_z + \underline{\boldsymbol{C}}_\mathrm{b}\underline{\boldsymbol{u}}_\mathrm{b} = 0 \tag{2.104}$$

$$\boldsymbol{r}_\mathrm{w}\left(\underline{\boldsymbol{A}}_z, \underline{\boldsymbol{i}}_\mathrm{w}\right) = \boldsymbol{K}\boldsymbol{D}_\mathrm{w}\underline{\boldsymbol{A}}_z + \underline{\boldsymbol{G}}_\mathrm{w}\boldsymbol{i}_\mathrm{w}^{k+1} + \underline{\boldsymbol{h}}\left(\underline{\boldsymbol{v}}_\mathrm{w}\right) = 0 \tag{2.105}$$

in which $\underline{\boldsymbol{C}}_\mathrm{b}$, $\underline{\boldsymbol{G}}_\mathrm{w}$, and $\underline{\boldsymbol{h}}$ denote the circuit matrices of the rotor and stator windings, the definitions of which are given in (Arkkio, 1987).

The Newton-Raphson scheme is developed separately for the real and imaginary parts of the variables. The vector of incremental adjustments to be performed at each iteration n is solvable from

$$\begin{bmatrix} \boldsymbol{P}^1 & \boldsymbol{R} & \boldsymbol{D}_\mathrm{b}^\mathrm{T} & 0 & \boldsymbol{D}_\mathrm{w}^\mathrm{T}\boldsymbol{K}^\mathrm{T} & 0 \\ -\boldsymbol{T} & -\boldsymbol{P}^2 & 0 & -\boldsymbol{D}_\mathrm{b}^\mathrm{T} & 0 & -\boldsymbol{D}_\mathrm{w}^\mathrm{T}\boldsymbol{K}^\mathrm{T} \\ \boldsymbol{D}_\mathrm{b} & 0 & \boldsymbol{C}_\mathrm{b}^\mathrm{Re} & -\boldsymbol{C}_\mathrm{b}^\mathrm{Im} & 0 & 0 \\ 0 & -\boldsymbol{D}_\mathrm{b} & -\boldsymbol{C}_\mathrm{b}^\mathrm{Im} & -\boldsymbol{C}_\mathrm{b}^\mathrm{Re} & 0 & 0 \\ \boldsymbol{K}\boldsymbol{D}_\mathrm{w} & 0 & 0 & 0 & \boldsymbol{G}_\mathrm{w}^\mathrm{Re} & -\boldsymbol{G}_\mathrm{w}^\mathrm{Im} \\ 0 & -\boldsymbol{K}\boldsymbol{D}_\mathrm{w} & 0 & 0 & -\boldsymbol{G}_\mathrm{w}^\mathrm{Im} & -\boldsymbol{G}_\mathrm{w}^\mathrm{Re} \end{bmatrix} \begin{bmatrix} \Delta\boldsymbol{A}_z^{\mathrm{Re}|n} \\ \Delta\boldsymbol{A}_z^{\mathrm{Im}|n} \\ \Delta\boldsymbol{u}_\mathrm{b}^{\mathrm{Re}|n} \\ \Delta\boldsymbol{u}_\mathrm{b}^{\mathrm{Im}|n} \\ \Delta\boldsymbol{i}_\mathrm{w}^{\mathrm{Re}|n} \\ \Delta\boldsymbol{i}_\mathrm{w}^{\mathrm{Im}|n} \end{bmatrix} = - \begin{bmatrix} \boldsymbol{r}_\mathrm{f}^\mathrm{Re} \\ -\boldsymbol{r}_\mathrm{f}^\mathrm{Im} \\ \boldsymbol{r}_\mathrm{b}^\mathrm{Re} \\ -\boldsymbol{r}_\mathrm{b}^\mathrm{Im} \\ \boldsymbol{r}_\mathrm{w}^\mathrm{Re} \\ -\boldsymbol{r}_\mathrm{w}^\mathrm{Im} \end{bmatrix} \tag{2.106}$$

The elements of the Jacobians and matrices $\boldsymbol{R}$ and $\boldsymbol{T}$ are

$$P_{lm}^{1}\left(\boldsymbol{A}_z^{\mathrm{Re}|n},\boldsymbol{A}_z^{\mathrm{Im}|n}\right)= \int_{\Omega}\left(\begin{array}{l}\displaystyle\sum_{j=1}^{N_\mathrm{n}}\left(\frac{\partial\left(|\underline{\nu}|\cos\left(\varphi_\mathrm{h}\right)\right)}{\partial A_{z|m}^{\mathrm{Re}|n}}\nabla N_l\cdot\nabla N_j A_{z|j}^{\mathrm{Re}|n}-\frac{\partial\left(|\underline{\nu}|\sin\left(\varphi_\mathrm{h}\right)\right)}{\partial A_{z|m}^{\mathrm{Re}|n}}\nabla N_l\cdot\nabla N_j A_{z|j}^{\mathrm{Im}|n}\right)\\ +\left(|\underline{\nu}|\cos\left(\varphi_\mathrm{h}\right)\right)\nabla N_l\cdot\nabla N_m\end{array}\right)\mathrm{d}\Omega \quad (2.107)$$

$$P_{lm}^{2}\left(\boldsymbol{A}_z^{\mathrm{Re}|n},\boldsymbol{A}_z^{\mathrm{Im}|n}\right)= \int_{\Omega}\left(\begin{array}{l}\displaystyle\sum_{j=1}^{N_\mathrm{n}}\left(\frac{\partial\left(|\underline{\nu}|\cos\left(\varphi_\mathrm{h}\right)\right)}{\partial A_{z|m}^{\mathrm{Im}|n}}\nabla N_l\cdot\nabla N_j A_{z|j}^{\mathrm{Im}|n}+\frac{\partial\left(|\underline{\nu}|\sin\left(\varphi_\mathrm{h}\right)\right)}{\partial A_{z|m}^{\mathrm{Im}|n}}\nabla N_l\cdot\nabla N_j A_{z|j}^{\mathrm{Re}|n}\right)\\ +\left(|\underline{\nu}|\cos\left(\varphi_\mathrm{h}\right)\right)\nabla N_l\cdot\nabla N_m\end{array}\right)\mathrm{d}\Omega \quad (2.108)$$

$$R_{lm}\left(\boldsymbol{A}_z^{\mathrm{Re}|n},\boldsymbol{A}_z^{\mathrm{Im}|n}\right)= \int_{\Omega}\left(\begin{array}{l}\displaystyle\sum_{j=1}^{N_\mathrm{n}}\left(\frac{\partial\left(|\underline{\nu}|\cos\left(\varphi_\mathrm{h}\right)\right)}{\partial A_{z|m}^{\mathrm{Im}|n}}\nabla N_l\cdot\nabla N_j A_{z|j}^{\mathrm{Re}|n}-\frac{\partial\left(|\underline{\nu}|\sin\left(\varphi_\mathrm{h}\right)\right)}{\partial A_{z|m}^{\mathrm{Im}|n}}\nabla N_l\cdot\nabla N_j A_{z|j}^{\mathrm{Im}|n}\right)\\ -\left(|\underline{\nu}|\sin\left(\varphi_\mathrm{h}\right)\right)\nabla N_l\cdot\nabla N_m-s\omega\sigma N_l N_m\end{array}\right)\mathrm{d}\Omega \quad (2.109)$$

$$T_{lm}\left(\boldsymbol{A}_z^{\mathrm{Re}|n},\boldsymbol{A}_z^{\mathrm{Im}|n}\right)= \int_{\Omega}\left(\begin{array}{l}\displaystyle\sum_{j=1}^{N_\mathrm{n}}\left(\frac{\partial\left(|\underline{\nu}|\cos\left(\varphi_\mathrm{h}\right)\right)}{\partial A_{z|m}^{\mathrm{Re}|n}}\nabla N_l\cdot\nabla N_j A_{z|j}^{\mathrm{Im}|n}+\frac{\partial\left(|\underline{\nu}|\sin\left(\varphi_\mathrm{h}\right)\right)}{\partial A_{z|m}^{\mathrm{Re}|n}}\nabla N_l\cdot\nabla N_j A_{z|j}^{\mathrm{Re}|n}\right)\\ \left(|\underline{\nu}|\sin\left(\varphi_\mathrm{h}\right)\right)\nabla N_l\cdot\nabla N_m+s\omega\sigma N_l N_m\end{array}\right)\mathrm{d}\Omega . \quad (2.110)$$

As in the case of the time-discretized model, the Newton-Raphson scheme is implemented in an incomplete manner, as the derivative of the complex reluctivity is not affected by the 1-D eddy current modeling. Instead, it is solved from the values suggested by the 2-D field, as can be seen from Equations (2.107)–(2.110) (Pippuri and Arkkio, 2009).

Complex reluctivity

When the complex phasor formulation is employed, the hysteretic behavior of ferromagnetic materials can be represented by the complex reluctivity (Arkkio et al., 1998). In addition to the hysteresis, in this work, the eddy currents in the electrical steel sheets are incorporated into the 2-D equations through the complex reluctivity. Hence, it is defined as

$$\underline{\nu} = \left|\underline{\nu}\right|_{\mathrm{c}} \mathrm{e}^{\mathrm{j}(\varphi_{\mathrm{h}} + \varphi_{\mathrm{c}})} \tag{2.111}$$

where $|\underline{\nu}|_{\mathrm{c}}$ is the absolute value of the reluctivity imposed by the 1-D eddy current model, φ_{h} the hysteresis part of the argument, and φ_{c} the eddy current part of the argument.

In the time-harmonic approach the 1-D eddy current equations are implemented in a linearized manner only. The absolute value of the reluctivity $|\underline{\nu}|$ needed for their evaluation is determined in each case by the square of the 2-D magnetic flux density from a single-valued reluctivity curve. The values on that curve are defined employing the expression (Luomi et al., 1986)

$$\left|\underline{\nu}\right| = \frac{1}{T}\int_{T} \frac{H(t)}{B_{\mathrm{p}} \sin\left(2\pi t/T\right)} \mathrm{d}t \tag{2.112}$$

Equation (2.112) assumes a sinusoidal and unidirectional time variation for the magnetic flux density, while the magnetic field strength can be taken from a single-valued magnetization curve of the material in question.

The hysteresis of ferromagnetic materials causes phase lag between the magnetic flux density and magnetic field strength, the modeling of which is covered by the hysteresis part of the argument of the complex reluctivity. The method represents the hysteresis part of the argument as a single-valued curve that is a function of the 2-D magnetic flux density. In this work the curves were fitted from measuring data of alternating magnetic fields. The related experiments are discussed in detail in Section 2.3.1.

The absolute value of the reluctivity in the 2-D computation is imposed by the 1-D eddy current distribution. The increase in the phase shift between the magnetic flux density and magnetic field strength is taken into account by an additional argument term, as shown in Equation (2.111). Let us first consider the formulation of the absolute value of the reluctivity $|\underline{\nu}|_{\mathrm{c}}$. First, the effective magnetic flux density is evaluated

$$b_{\mathrm{ef}}(z) = \frac{1}{\sqrt{2}} \sqrt{\left(b_x^{\mathrm{Re}}(z)\right)^2 + \left(b_x^{\mathrm{Im}}(z)\right)^2 + \left(b_y^{\mathrm{Re}}(z)\right)^2 + \left(b_y^{\mathrm{Im}}(z)\right)^2} \,. \tag{2.113}$$

The effective values of the other quantities can be calculated similarly.

The magnetic field strength at the boundary of the sheet is derived as

$$h_{\mathrm{ef}}(-d) = \left|\underline{\nu}\right| b_{\mathrm{ef}}(-d) \tag{2.114}$$

in which $b_{\mathrm{ef}}(-d)$ is the value of the effective magnetic flux density at the boundary of the sheets.

The absolute value of the reluctivity for the 2-D computation is obtainable from the effective magnetic field strength at the boundary and average effective magnetic flux density $b_{\mathrm{ef,\,ave}}$ as

$$|\underline{\nu}|_{\mathrm{c}} = \frac{h_{\mathrm{ef}}(-d)}{b_{\mathrm{ef,\,ave}}}. \tag{2.115}$$

The definition of the eddy current argument of the reluctivity is formulated using two different expressions of the eddy current losses. One can calculate the eddy current losses from the effective eddy current density j_{ef}

$$P_{\mathrm{c}} = \int_V \frac{1}{\sigma} j_{\mathrm{ef}}^2 \mathrm{d}V. \tag{2.116}$$

On the other hand, these can be estimated in a similar manner to the hysteresis losses by integrating the area of an ellipse traced by the 1-D magnetic flux density vector (Niemenmaa, 1988)

$$P_{\mathrm{c}} = \int_V \nu_{\mathrm{c}}^{\mathrm{Im}} \omega b_{\mathrm{ef}}^2 \mathrm{d}V. \tag{2.117}$$

Setting these two formulations to be equal yields an expression from which the imaginary part of the complex reluctivity that is connected to the eddy currents can be solved

$$\nu_{\mathrm{c}}^{\mathrm{Im}} = \frac{j_{\mathrm{ef,\,ave}}^2}{\omega \sigma b_{\mathrm{ef,\,ave}}^2} \tag{2.118}$$

in which $j_{\mathrm{ef}}{}^2{}_{,\,\mathrm{ave}}$ is the average of the second power of the effective eddy current density and $b_{\mathrm{ef}}{}^2{}_{,\,\mathrm{ave}}$ is the average of the second power of the effective magnetic flux density.

As the absolute value of the reluctivity (2.115) and the imaginary part of the reluctivity (2.118) are known, the real part of the reluctivity is easy to solve

$$\nu_{\mathrm{c}}^{\mathrm{Re}} = \sqrt{\left(|\underline{\nu}|_{\mathrm{c}}\right)^2 - \left(\nu_{\mathrm{c}}^{\mathrm{Im}}\right)^2} \tag{2.119}$$

Finally, the eddy current part of the argument is

$$\varphi_{\mathrm{c}} = \arctan\left(\frac{\nu_{\mathrm{c}}^{\mathrm{Im}}}{\nu_{\mathrm{c}}^{\mathrm{Re}}}\right) \tag{2.120}$$

2.2 Computational algorithm of the cage-induction machine model

This section deals with the computational algorithms developed for the time-discretized and time-harmonic implementations of the coupled 2-D–1-D method. The time-discretized implementation is discussed first. Within it, the 1-D eddy current modeling of the sheets can be coped with in two ways. First, the actual magnetic properties of the sheets can be worked out. This results in a computational routine consisting of two nested iterative procedures. Second, the magnetic properties of the sheets in the 1-D model can be linearized. In the second section, the computational algorithm of the time-harmonic implementation is elaborated. That involves the possibility of employing non-sinusoidal supply conditions. In addition to the eddy currents, the hysteresis of the ferromagnetic materials is also included in the field solution. Differently from the time-discretized approach, only the linearized way of dealing with the 1-D eddy current problem is realized.

2.2.1 Transient time-discretized implementation

A flowchart of the computational algorithm of the time-discretized implementation of the coupled 2-D–1-D method is presented in Figure 2.5. As shown in Figure 2.5, the computation starts with the initialization, which includes setting the inputs and structuring the system matrices of the problem. The input data of a time-discretized simulation contain the information on the geometry of the application being studied, the meshing of the geometry, the materials in the different parts of the geometry, the supply conditions, the initial state, and the time-discretization. A field solution obtained by some means besides a zero field can be utilized as an initial state. In this work, the time-harmonic implementation of the 2-D–1-D model is applied to determine the initial states for the time-discretized simulations. In practice, the operating point to be studied is first computed with the time-harmonic 2-D–1-D model. Transforming the real part of the complex-valued time-harmonic solution obtained into a DC field yields the initial condition of a time-discretized simulation (Arkkio, 1987). Applying such an initial condition usually ensures that a steady state is reached after simulating only a few periods of supply voltage.

After the initialization, the solution of the coupled 2-D–1-D equations is worked out iteratively at specified equally spaced time-steps. In the 2-D scheme, at every iteration of each of the time-steps, the element-wise system matrices, i.e., the Jacobian matrix and residual vector, are first constructed and then added one by one to the global matrices.

As pointed out above, the 1-D model is used to couple the eddy currents in electrical steel sheets to the 2-D machine model. At each point at which the 1-D problem fulfilling

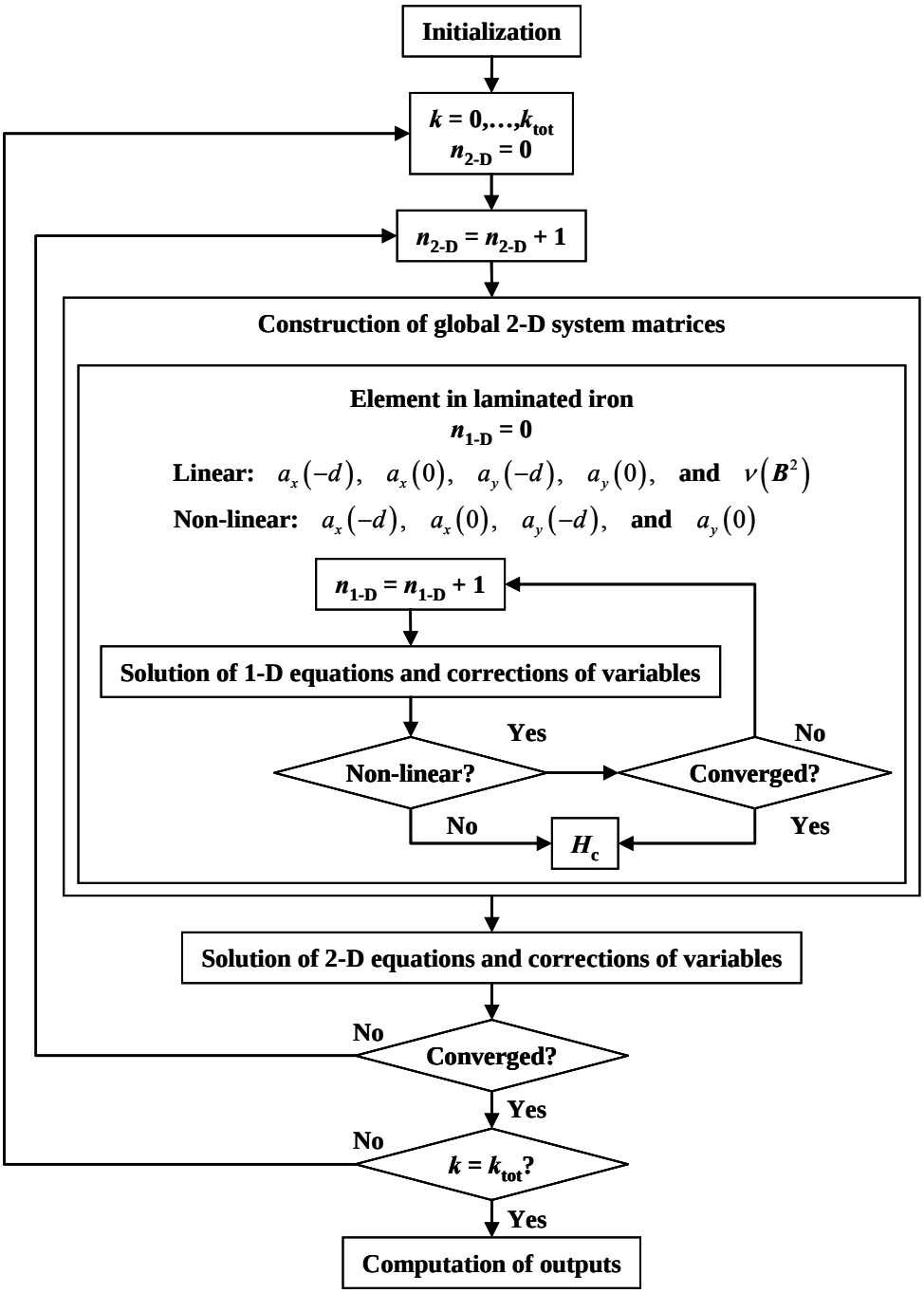

Figure 2.5 Flowchart of the time-stepping model.

Equation (2.49) needs to be solved, its boundary conditions are imposed by the 2-D field as

$$a_x^{k+1|n}\left(-d,t\right)=dB_y^{k+1|n}\left(x,y,t\right) \qquad a_x^{k+1|n}\left(0,t\right)=0 \tag{2.121}$$

$$a_y^{k+1|n}\left(-d,t\right) = -dB_x^{k+1|n}\left(x,y,t\right) \qquad a_y^{k+1|n}\left(0,t\right) = 0 \tag{2.122}$$

in which d is half the thickness of the electrical steel sheets. B_x and B_y are the components of $\boldsymbol{B}$ at an x-y point of the 2-D cross-sectional plane in which the eddy current model is called. To be exact, here the x-y points are the integration points of the elements in the laminated iron. The magnetic flux density $\boldsymbol{B}$ equals the average magnetic flux density in the thickness of the sheets at a certain x-y point. The symmetry of the 1-D problem is exploited by performing the solution only in half of the thickness of the sheets.

The lamination model is here realized in a linear or non-linear manner, as emphasized in Figure 2.5. If a linear implementation is applied, in addition to the boundary conditions given by Equations (2.121) and (2.122), the reluctivity of the sheets is taken as an input from the 2-D scheme. Hence, the reluctivity is then constant throughout the entire thickness of the sheets. Its value is imposed by the square of the 2-D magnetic flux density $\boldsymbol{B}^2$ from a single-valued reluctivity curve. That is the same 2-D magnetic flux density as that associated with the boundary conditions at a certain point. The construction of the 1-D system matrices is performed in the same way as in the 2-D scheme of the element-wise 1-D Jacobian matrices and residual vectors. If the 1-D equations are utilized in a linear manner, no iterative process is required for their solution. The correction of the 1-D magnetic vector potential is performed only once, after which the computation proceeds to the next stage.

If the true magnetic properties of the steel laminations are to be modeled, the non-linear implementation of the 1-D eddy current model has to be employed. Then the reluctivity in the 1-D scheme is defined by the same reluctivity curve as that which is utilized in the 2-D model, and its value at each of the integration points of the 1-D elements is imposed by the square of the 1-D magnetic flux density. The solution of such a formulation must be carried out iteratively. The iterative process continues until the convergence limits are reached. After the convergence, the computation proceeds to the next stage. The output of both the linear and non-linear implementations of the 1-D model is $\boldsymbol{H}_\mathrm{c}$.

As depicted in Figure 2.5, at each iteration, the increment vector showing the correction to be made to the 2-D variables from the previous iteration is solved from the composed 2-D system matrices. In order to achieve better stability for the computation, the increment vector obtained is not utilized in full. Instead, under-relaxation is applied. After the solution of the 2-D equations converges, the time-step is finished by saving the instantaneous values of the magnetic vector potential and other variables.

The time-discretized process is continued until all the predetermined time-steps are completed. The number of time-steps in a simulation must be large enough to model the steady-state operation of the test machine for a couple of periods of supply voltage. After the last time-step, the computation is finalized, including the integration of the aver-

age values of numerous quantities, such as the electromagnetic torque, powers, losses, currents, and voltages, utilizing their stored time-step-specific results.

Electric power and electromagnetic losses

The steady-state average values of different quantities are of great interest. The average electric power, i.e., the input power in the motoring operation and the output power in the generating operation, is calculated from (Arkkio, 1987)

$$P_{\mathrm{el}} = \frac{1}{T}\int_T \left\{ \sum_{n=1}^{m} u_{\mathrm{w}|n} i_{\mathrm{w}|n} \right\} \mathrm{d}t \tag{2.123}$$

in which T is the time period over which the power is integrated. Typically, taking one or two periods of line voltage into account yields appropriate results.

The formulae for the stator phase winding are derived with the skin effect being neglected. Thus, the losses in the winding can be evaluated from (Arkkio, 1987)

$$P_{\mathrm{wr}} = \frac{1}{T}\int_T \left\{ \sum_{n=1}^{m} R_{\mathrm{w}} \left(i_{\mathrm{w}|n} \right)^2 \right\} \mathrm{d}t \tag{2.124}$$

The resistive losses in the squirrel-cage rotor winding are defined as a volume integral of the product of the inverse of the electrical conductivity and the square of the current density. The time average of these losses fulfills (Arkkio, 1987)

$$P_{\mathrm{cr}} = \frac{1}{T}\int_T \left\{ \sum_{n=1}^{Q_{\mathrm{b}}} \int_{V_n} \sigma \left(\left(\frac{\partial A_z}{\partial t} \right)^2 - \frac{u_{\mathrm{b}|n}}{l_{\mathrm{b}}} \frac{\partial A_z}{\partial t} \right) \mathrm{d}V \right\} \mathrm{d}t \tag{2.125}$$

in which V_n is the volume of the nth rotor bar inside the core region of the machine geometry.

The proposed coupled method embraces the modeling of the eddy currents in the electrical steel sheets. Hence, the eddy current losses of the sheets can be worked out from the actual eddy current distribution. Integrating the product of the inverse of the electrical conductivity and the square of the eddy current density over half of the lamination thickness and averaging the result thus obtained yields the eddy current loss density. The average eddy current loss is obtained as a volume integral of the eddy current loss density and by taking a time average. This can be expressed as

$$P_{\mathrm{c}} = \frac{1}{T}\int_{T}\left\{\int_{V_{\mathrm{c}}}\left(\frac{1}{d}\int_{d}\frac{1}{\sigma}|\boldsymbol{j}|^{2}\,\mathrm{d}z\right)\mathrm{d}V\right\}\mathrm{d}t \tag{2.126}$$

where V_{c} denotes the volume of the laminated iron core and $|\boldsymbol{j}|$ the magnitude of the eddy current density given as

$$|\boldsymbol{j}| = \sqrt{j_x^2 + j_y^2}\ . \tag{2.127}$$

The losses in the laminated iron core consist of hysteresis, eddy current, and excess losses. The modeling of the hysteresis and excess effects is omitted from the time-discretized analysis. Hence, the losses resulting from these two phenomena have to be estimated by some post-processing approach. For that purpose, a method proposed by Belahcen and Arkkio (2008) is applied. In that method, the components of the core losses are computed at each time-step by post-processing, utilizing the field solution from the previous and current time-step. The average hysteresis losses can be calculated from the time-specific values as

$$P_{\mathrm{h}} = \frac{1}{T}\int_{T}\left\{\int_{V_{\mathrm{c}}}\left(k_{\mathrm{h}}|\boldsymbol{B}|\frac{\partial|\boldsymbol{B}|}{\partial t} + k_{\mathrm{r}}\frac{1-\dfrac{|\boldsymbol{B}|}{B_{\mathrm{s}}}}{1+b\left(1-\dfrac{|\boldsymbol{B}|}{B_{\mathrm{s}}}\right)^{2}}|\boldsymbol{B}|\left|\frac{\partial\theta}{\partial t}\right|\right)\mathrm{d}V\right\}\mathrm{d}t \tag{2.128}$$

where k_{h} denotes the alternating hysteresis loss coefficient, $|\boldsymbol{B}|$ the magnitude of the 2-D magnetic flux density defined as

$$|\boldsymbol{B}| = \sqrt{B_x^2 + B_y^2}\ , \tag{2.129}$$

k_{r} the rotating hysteresis loss coefficient, B_{s} the saturation magnetic flux density, b a material parameter related to the texture and grain size of the material, and θ the angle of the magnetic flux density vector given as

$$\theta = \arctan\left(B_y / B_x\right). \tag{2.130}$$

Conveniently, the hysteresis loss formulation Equation (2.128) contains both the alternating and rotating parts.

The excess losses in the steel laminations are also worked out at each of the time-steps. According to the approach taken by Belahcen and Arkkio (2008), the average excess losses satisfy

$$P_{\mathrm{e}} = \frac{1}{T}\int_{T}\left\{\int_{V_{\mathrm{c}}}\left(k_{\mathrm{ea}}\left|\frac{\partial|\boldsymbol{B}|}{\partial t}\right|^{\frac{1}{2}}\frac{\partial|\boldsymbol{B}|}{\partial t}\right)\mathrm{d}V\right\}\mathrm{d}t \tag{2.131}$$

where k_{ea} denotes the excess-loss coefficient.

Electromagnetic torque, shaft power, and friction losses

The average electromagnetic torque produced by the machine being studied is computed using a method described by Arkkio (1987):

$$T_{\mathrm{e}} = \frac{1}{T}\int_{T}\left\{\frac{1}{\mu_0\left(r_{\mathrm{s}} - r_{\mathrm{r}}\right)}\int_{S_{\mathrm{ag}}} rB_{\mathrm{r}}B_{\varphi}\mathrm{d}S\right\}\mathrm{d}t \tag{2.132}$$

in which r_{s} denotes the outer radii of the air gap, r_{r} the inner radii of the air gap, S_{ag} the cross-section area of the air gap, r the radius, B_{r} the radial component of the 2-D magnetic flux density, and B_{φ} the angular component of the 2-D magnetic flux density.

The friction losses arising in rotating electrical machinery are omitted from the analysis. Hence, the average shaft power can be evaluated by the following expression:

$$P_{\mathrm{s}} = \Omega_{\mathrm{m}} T_{\mathrm{e}} \tag{2.133}$$

where Ω_{m} denotes the mechanical angular frequency of the rotor of the machine.

During the time-discretized simulation, the rotor of the machine is rotated at an angle corresponding to the mechanical angular frequency. When the rotor rotates at a constant speed, no additional equations are needed. In a more general case, the change to be made to the position of the rotor at each time-step, i.e., the rotation angle has to be solved from

$$\Omega_{\mathrm{m}}^{k+1} = \Omega_{\mathrm{m}}^{k} + \frac{T_{\mathrm{e}}^{k} - T_{\mathrm{s}}^{k}}{J_{\mathrm{m}}}\Delta t\,, \tag{2.134}$$

$$\alpha^{k+1} = \alpha^{k} + \Omega_{\mathrm{m}}^{k}\Delta t\,, \tag{2.135}$$

where T_{s} denotes the shaft torque, J_{m} the moment of inertia of the rotor, and α the angle according to which the rotor is rotated.

Power balance

The correctness of the implementation of the time-discretized algorithm that is developed is assessed by considering the power balance. Generally, if the input power fed to a system is equivalent to the sum of its output power and its losses, the power balance is fulfilled. In a steady state, employing the average powers determined above, the preceding condition can be expressed for the numerical method discussed here as

$$P_{\mathrm{el}} = P_{\mathrm{s}} + P_{\mathrm{wr}} + P_{\mathrm{cr}} + P_{\mathrm{c}}\,. \tag{2.136}$$

The definition of the power balance (2.136) encompasses the components of losses that are incorporated into the 2-D–1-D field and winding equations, the stator-winding DC resistive losses, the rotor-cage losses, and the eddy current losses of the sheets. The hysteresis and excess losses of the sheets and the eddy current losses of the stator winding are also evaluated during the simulations but within the post-processing phase. Hence, these make no contribution to the field computation or to the power balance. In addition, the time interval over which the powers are integrated is supposed to be long enough for the time average of the change in the energy of the magnetic field to vanish.

2.2.2 Time-harmonic implementation

When the approximation of sinusoidal time variation is employed, the source of the electromagnetic field and the other quantities too are supposed to vary at a single frequency, as discussed in the section “Time-harmonic analysis”. In this work, in order to broaden the applicability of the time-harmonic version of the coupled model, it is not implemented in the usual way, but in a manner that enables several frequency components to be handled consecutively during one simulation. In this way, a realization of the model is attained that can be applied to analyze, for instance, frequency-converter-fed electrical machines.

A flowchart of the implementation of the time-harmonic model is given in Figure 2.6. The initialization begins the computation. During that process, the inputs are set and the system matrices are assembled. Among the inputs, the geometry, meshing, materials, and supply conditions for the application being studied are passed. If a non-sinusoidal source voltage or current is to be applied, the inputs must include its time series. The actual supply conditions of a simulation are then determined by performing a Fourier analysis of the waveform provided and by choosing, in addition to the fundamental frequency component, the $\Gamma - 1$ harmonics with the biggest amplitudes.

The coupled 2-D–1-D analysis is first carried out utilizing the fundamental wave of the supply. As shown in Figure 2.6, this is an iterative process. At each iteration, the element-wise matrices are first assembled and then added to the global system matrices. At

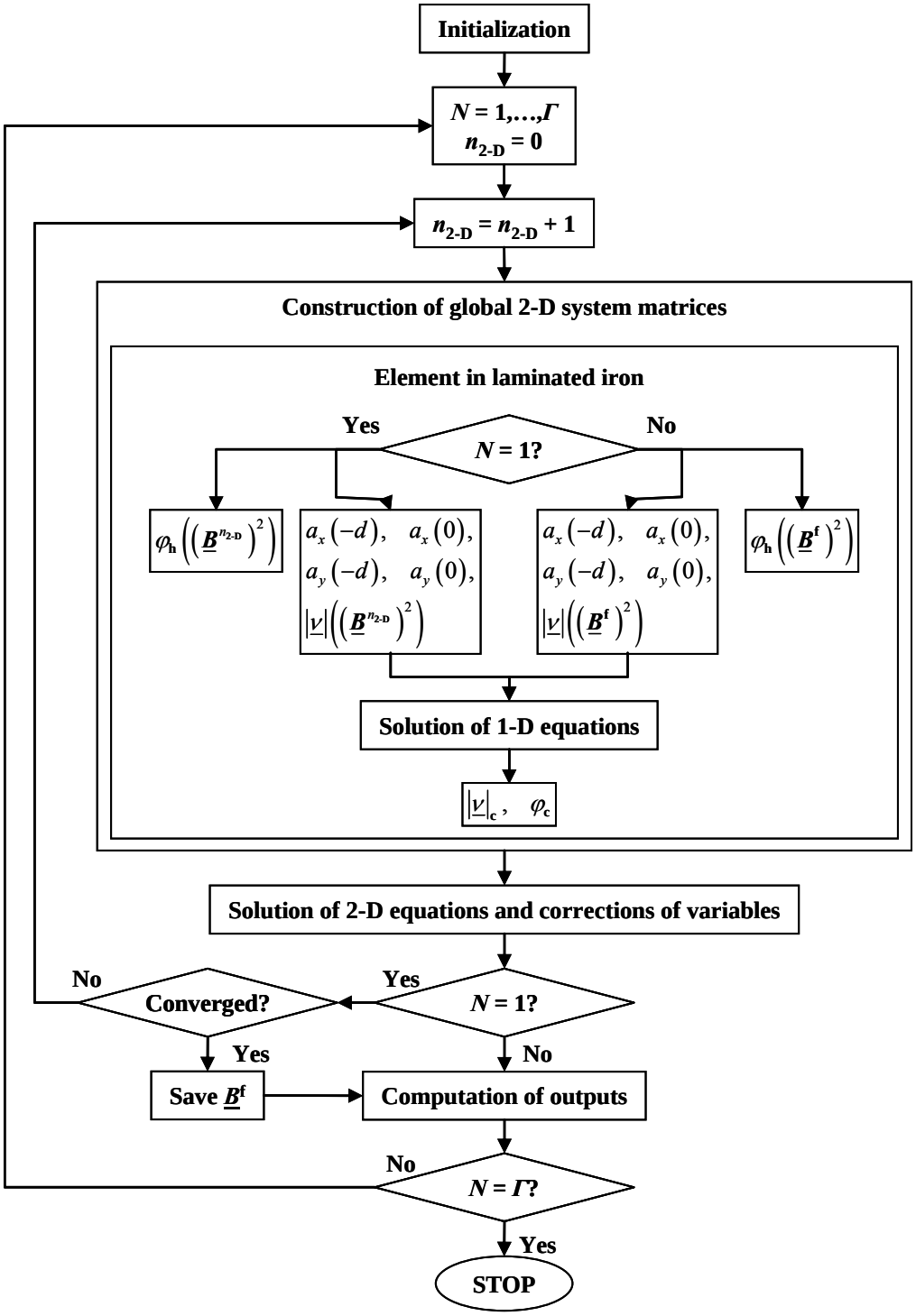

Figure 2.6 Flowchart of the time-harmonic machine model.

the integration points of the 2-D elements in the laminated iron, the 1-D eddy current model is called and used to update the absolute value of the complex reluctivity, $|\underline{\nu}|_c$, and to define the eddy current part of the argument of the complex reluctivity, φ_c. In the

time-harmonic implementation of the coupled method, the 1-D eddy current model is realized only in a linear way. Hence, the reluctivity within the thickness of the sheets is a constant and is imposed from the reluctivity curve by the square of the 2-D magnetic flux density, $\underline{\boldsymbol{B}}^2$. The boundary conditions of the 1-D eddy current problem are also determined by the 2-D magnetic flux density. As the symmetry of the sheets is exploited, these can be written as

$$\underline{a}_x^n\left(-d\right) = d\underline{B}_y^n\left(x,y\right) \qquad \underline{a}_x^n\left(0\right) = 0 \tag{2.137}$$

$$\underline{a}_y^n\left(-d\right) = -d\underline{B}_x\left(x,y\right) \qquad \underline{a}_y^n\left(0\right) = 0 \tag{2.138}$$

where $\underline{B}_x$ and $\underline{B}_y$ are the components of $\underline{\boldsymbol{B}}$ at an x-y point of the 2-D cross-section geometry in which the eddy current model is called. As a result of the simplifying assumptions adopted, the 1-D eddy current problem of the sheets can be solved analytically.

In addition to the eddy currents, the hysteresis in the electrical steel sheets is incorporated into the analysis. The hysteresis part of the argument of the complex reluctivity, φ_h, is imposed from a hysteresis-argument curve at each integration point of the 2-D elements in the laminated iron by the square of the 2-D magnetic flux density, $\underline{\boldsymbol{B}}^2$.

Solving the system of equations that has been constructed yields the increment vector used to correct the 2-D variables from the previous iteration. After each iteration, the convergence test is performed. As the computation converges, the outputs, such as losses, are calculated and the nodal values of the 2-D magnetic vector potential are saved. Then, if an input voltage or current waveform consisting only of a single frequency component is applied, i.e., Γ is equal to 1, the computation is stopped. If not, the computation is continued so that the 2-D–1-D fields generated by the Γ harmonics of the input waveform are solved one by one. In order to sustain the same level of magnetization throughout the entire analysis, the absolute value of reluctivity used in the 1-D model and the hysteresis part of the argument are invariably determined by the 2-D magnetic flux density associated with the fundamental component of the input waveform, and the iterative solution of the 2-D equations is omitted. Otherwise the computation proceeds in the same way as under the fundamental wave.

Electric power and electromagnetic losses

The average values of the electric power and the stator and rotor winding losses can be calculated from Equations (2.123)–(2.125) as phasor operations.

The eddy current losses of the sheets are evaluated from the eddy current density as

$$P_{\mathrm{c}} = \int_{V_{\mathrm{c}}} \left(\frac{1}{d} \int_{d} \frac{1}{\sigma} j_{\mathrm{ef}}^2 \mathrm{d}z \right) \mathrm{d}V \,. \tag{2.139}$$

The hysteresis of the ferromagnetic materials is also contained in the field solution and the losses resulting from it are solvable from

$$P_{\mathrm{h}} = \int_{V_{\mathrm{c}}} \nu_{\mathrm{h}}^{\mathrm{Im}} \omega B_{\mathrm{ef}}^2 \mathrm{d}V \tag{2.140}$$

in which $\nu_{\mathrm{h}}^{\mathrm{Im}}$ denotes the imaginary part of the reluctivity resulting from the hysteresis and B_{ef} the effective value of the 2-D magnetic flux density.

Electromagnetic torque and shaft power

Equations (2.132) and (2.133) are also applied to evaluate the electromagnetic torque and shaft power within the time-harmonic analysis.

Power balance

Besides the eddy currents, the hysteresis of the electrical steel sheets is incorporated into the time-harmonic field equations. The power balance of such a formulation fulfills

$$P_{\mathrm{el}} = P_{\mathrm{s}} + P_{\mathrm{wr}} + P_{\mathrm{cr}} + P_{\mathrm{c}} + P_{\mathrm{h}} \,. \tag{2.141}$$

2.3 Measurements

This section reports the measurements that were performed. First, the wound-ring sample that was manufactured is discussed. The measuring data of this sample are used to define the magnetic material properties and iron-loss parameters of the numerical models. In the second subsection, the experiments carried out on a cage-induction machine are reported. The coupled method is used to simulate that test machine and the results obtained are verified by the measurements.

2.3.1 Experiments on wound-ring sample

The electrical steel sheets of the wound-ring sample were machined out of the rotor of a 30-kW cage-induction motor. Photos of the rotor after the machining are presented in

Figures 2.7 and 2.8. The steel sheets obtained thereby were cut into the form of ellipsoids. Figure 2.9 presents the CAD drawing used in the cutting process. The contours of the ready-made sheets of the sample are depicted in red and all the measures are given in millimeters.

A toroid core without insulating sheets between the steel sheets was assembled and two magnetizing windings and one measuring winding were wound onto it. The main parameters and a photo of the ready sample henceforth referred to as R1382 are presented in Table II and in Figure 2.10.

The wound-ring sample was tested employing the measuring setup presented in Figure 2.11. The measurements were controlled by a computer using a LabVIEW FPGA module. An input voltage produced by an arbitrary voltage generator and amplified by a

Figure 2.7 Half of the rotor of the cage-induction machine.

Figure 2.8 End of the rotor from which the sheets were machined.

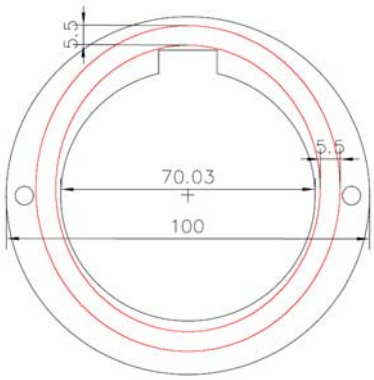

Figure 2.9 Geometry of the sheets of the wound-ring sample cut from the rotor sheets.

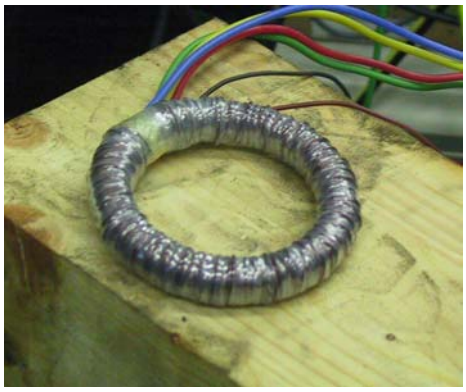

Figure 2.10 Wound-ring sample.

power amplifier was fed to the primary (magnetizing) coils. The results, which are the values of B and H, were collected with a data acquisition card.

Experiments with fundamental frequencies ranging from 20 Hz to 5 kHz were performed. Up to 2.5 kHz, it was possible to magnetize the sample until saturation. At frequencies higher than that, the flux levels reached were somewhat lower. A magnetization curve approximated from the ***B*-*H*** loops measured at an exciting frequency of 30 Hz is shown in Figure 2.12.

The main motivation for the construction of the wound-ring sample was to obtain data for defining the material properties of the test motor used in the work. Due to the age of the test machine, almost 20 years, there were not suitable manufacturer's catalogs at hand for that purpose. The 30-kW cage-induction motor, the rotor of which was exploited, was approximately of the same age and size and had the same sheet thicknesses as the test machine. Thus, it is reasonable to assume that the material characteristics of the cores of these two machines resemble each other closely enough.

Table II Main parameters of the wound-ring sample.

Mass (g)	63.8
Number of the sheets	9
Thickness of the sheets (mm)	0.65
Number of turns, magn.	250
Diameter of the wire, magn. (mm)	1
Number of turns, meas.	850
Diameter of wire, meas. (mm)	0.16

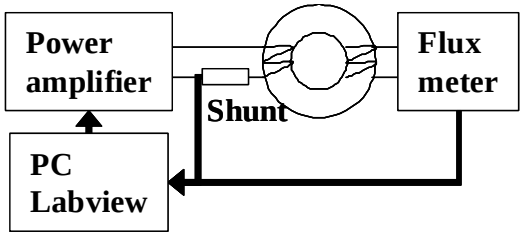

Figure 2.11 Measuring setup for the wound-ring sample.

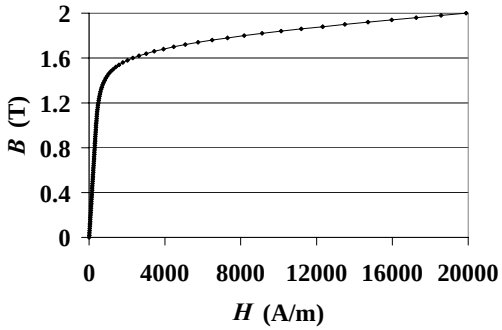

Figure 2.12 Magnetization curve of the steel laminations.

2.3.2 Experiments on electrical machines

This section introduces the test motor of the work and elaborates the measurements that were performed. Two types of no-load tests, slip-control and standard ones, are considered in addition to the loading experiments. The operation of the test motor is explored both with sinusoidal voltage excitation and frequency-converter supply.

Test motor

A 37-kW cage-induction machine is employed as a test motor in this work. Its cross-section area is depicted in Figure 2.13 and the main parameters are given in Table III.

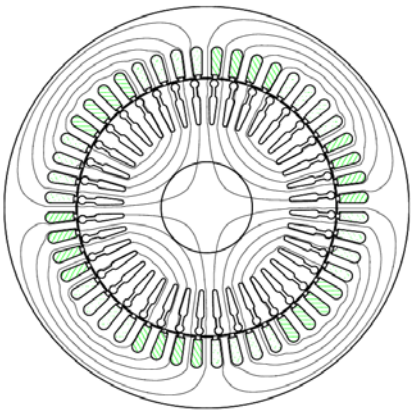

Figure 2.13 Cross-section area of the 37-kW cage-induction motor.

Table III Main parameters of the 37-kW cage-induction motor.

Machine type	Induction motor
Number of pole pairs	2
Number of phases	3
Number of stator slots	48
Outer diameter of the stator core (mm)	310
Inner diameter of the stator core (mm)	200
Outer diameter of the rotor core (mm)	198.4
Core length (mm)	249
Connection	star
Rated voltage (V)	380
Rated frequency (Hz)	50
Rated power (kW)	37
Electrical conductivity of laminations (MS/m)	2.5
Thickness of laminations (mm)	0.65

Standard no-load and load tests

Standard no-load and full-load tests for the 37-kW cage-induction motor were carried out under both sinusoidal and frequency-converter supply conditions (IEEE Std 112-1996, 1996). The devices, setups, and measuring processes applied are briefly discussed in the following four sections.

Measurement setup

The 37-kW test motor was first driven by a frequency converter. The measuring setup of the loading experiments is depicted in Figure 2.14. A photo of the test floor is shown in Figure 2.15. The frequency converter that was employed, illustrated on the left-hand side of Figure 2.14, was of the Vacon 90CX type. That is a relatively new device and has a control methodology based on pulse width modulation and a switching frequency controllable from 1 kHz to 10 kHz. As Figure 2.14 shows, a 40-kW DC generator was mechanically coupled with the test motor and utilized for the loading. The operating speed of this machine was controlled by a thyristor bridge rectifier. The measuring setup of the no-load experiments was otherwise the same as the one presented in Figure 2.14, but the DC generator was naturally uncoupled from the shaft of the test motor.

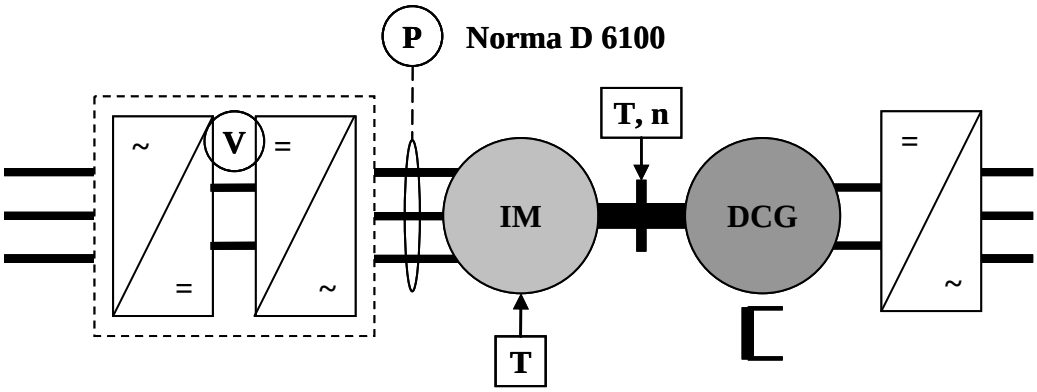

Figure 2.14 Measuring setup for the standard test. IM denotes the induction machine being tested and DCG the DC generator applied as load.

Figure 2.15 Experimental test floor.

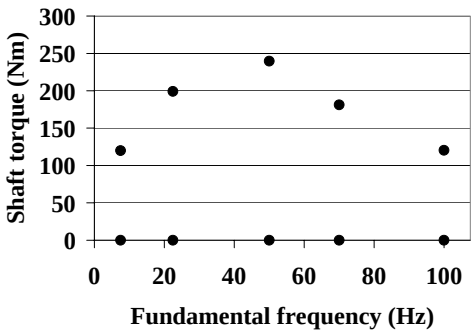

Figure 2.16 Measured operating points of the 37-kW cage-induction motor.

The voltages, currents, powers, and power factors of the test motor were monitored and recorded by a Norma Wide Band Power Analyzer D 6100. Its maximum sampling frequency is 70 kHz and shunts with a bandwidth of 2.2 MHz and accuracy of

±0.03…±0.1% were utilized for the current measurement. The torque was measured by a HBM T30FNA torque transducer and the speed by a tachometer of the Leine & Linde RSI 503 type. Both of these quantities were monitored and recorded through the power analyzer. The output-voltage waveforms of the frequency converter were saved by a computer program called PowerView 6000, with a sampling frequency of 70 kHz. More detailed information on the devices and programs can be found from, for instance, (Saitz, 2001).

The operating points that were studied are depicted in Figure 2.16. Each of these was measured by applying three different switching frequencies for the frequency converter, 1, 3, and 6 kHz, one by one. The intermediate DC link voltage of the frequency converter was monitored and was invariably adjusted to 510 V. Every experiment was carried out similarly by first running the test motor to a thermally steady state and then by recording the electromagnetic quantities together with the speed and torque. The resistance measurement was performed as a last experiment in order to determine the stator-winding temperature (IEC 60034-1).

The operating points shown in Figure 2.16 were also measured under a sinusoidal voltage supply. In each of the experiments, an input voltage equal to the fundamental component of the voltage waveform generated by the frequency converter at a switching frequency of 3 kHz was fed to the test machine. At no load, under the frequency-converter supply and with the switching frequency being 3 kHz, the fundamental frequency-fundamental voltage pairs were (7.5 Hz; 58.3 V), (22.5 Hz; 176.3 V), (50 Hz; 384.2 V), (70 Hz; 383.1 V), and (100 Hz; 383.4 V). The corresponding figures for the sinusoidal supply were (7.5 Hz; 58.5 V), (22.5 Hz; 176.8 V), (50 Hz; 383.6 V), (70 Hz; 382.6 V), and (100 Hz; 383.9 V).

Components of the measured total losses

In order to segregate the electromagnetic losses from the total losses of the standard tests, the friction losses must be known. Friction loss measurements employing the standard no-load test at variable voltage (IEEE Std 112-1996, 1996), (Saitz, 2001), and (Pippuri and Arkkio, 2008) were performed on the test motor at rotating speeds corresponding to the supply frequencies 7.5, 22.5, 50, 70, and 100 Hz. Subtraction of the friction losses from the total losses yields the electromagnetic losses. It must be noted that the observed obscurity concerning the quantity of the friction losses introduces some inaccuracy to the estimates thus obtained (Pippuri and Arkkio, 2008).

The experimental electromagnetic losses can be divided into the DC resistive losses of the stator winding and other electromagnetic losses. The DC resistive losses of the stator winding are evaluated as a product of the DC resistance and the square of the current.

Additional electromagnetic losses resulting from the frequency-converter supply

The RMS value of the sinusoidal voltage supply was adjusted to be in accordance with that of the fundamental component generated by the frequency converter. The additional electromagnetic losses inflicted by the distorted voltage waveform can be obtained by subtracting the total losses from the sinusoidal supply from those at the frequency-converter supply.

Slip-control no-load tests

The slip-control test was developed for measuring the no-load electromagnetic losses of rotating electrical machines. It is, however, also applicable to determining the hysteresis torque (Saitz, 2001), (Dlala, 2008b).

Measurement setup

The same measuring devices and software as in the standard no-load experiments were used (Saitz, 2001). In the slip-control no-load experiment, the test machine is mechanically coupled with a slip-ring machine, as shown in Figure 2.17. The stator windings of both the machines are fed from a sinusoidal voltage source. A three-phase power amplifier is used to supply the rotor of the slip-ring machine. That makes possible the fine

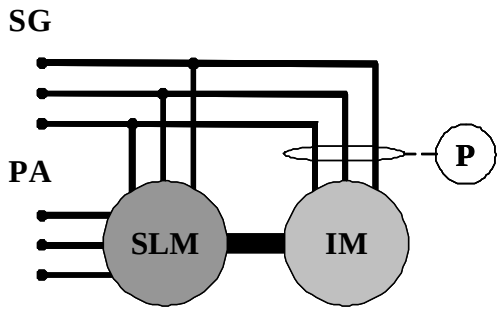

Figure 2.17 Measuring setup for the slip-control test. SG is an abbreviation for synchronous generator, PA for power amplifier, SLM for slip-ring machine, and IM for induction machine.

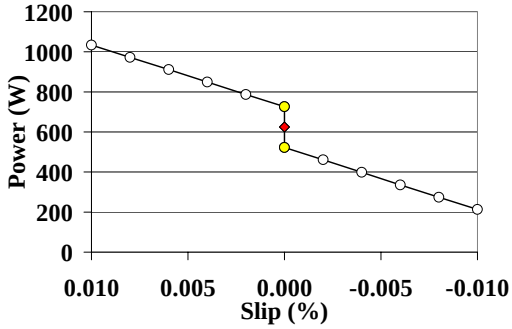

Figure 2.18 Average input power of the 37-kW cage-induction motor as a function of slip. White dots are measured, yellow dots are extrapolated to the zero slip, and the red dot is the result of the slip-control measurement, i.e., the no-load electromagnetic loss.

control of the rotating speed of the machines. Experiments on the test machine are carried out by running it at specific positive and negative slips in the vicinity of its synchronous speed. Employing the results obtained, the electromagnetic losses at a zero slip are estimated. Figure 2.18 illustrates the related extrapolation and averaging at the rated voltage of the test motor. For more detailed information on the slip-control measurement see (Saitz, 2001), (Pippuri and Arkkio, 2008).

The mechanical losses of the test motor, in the slip-control measurement, are compensated by a slip-ring machine mounted on the same shaft. This is a great advantage as it enables the no-load electromagnetic losses to be measured in a direct manner. At the same time, the consideration of the friction losses, the reliable experimenting of which has turned out be challenging, can be avoided. Another advantage of the slip-control test is that it appears to have good repeatability (Pippuri and Arkkio, 2008).

Components of the measured total losses

The total electromagnetic losses from the slip-control test can be separated into two components. The stator-winding DC losses are calculated as a product of the DC resistance and the square of the current. By subtracting these from the total electromagnetic losses, the second component, referred to as the other electromagnetic losses, is obtained.

3 Results

3.1 General properties of the combined 2-D–1-D model

This section aims at investigating various topics related to the computational methods that were developed. A particular goal is to find an optimal coupling for the eddy currents in the sheets to the 2-D field analysis. The power balance of the method is considered to be a useful measure for this assessment. In this section only simple example geometries are utilized, whereas a thorough analysis of the test motor is carried out in Section 3.2.

3.1.1 Simple example geometries employed in the study

The two simple example models or geometries used for examining the general properties of the methods are introduced next. The *x*-*y* plane and main parameters of the one henceforth referred to as *example geometry 1* are shown in Figure 3.1 and in Table IV. In Figure 3.1, the white-colored segments are associated with electrical steel sheets and the gray-colored segments with a coil.

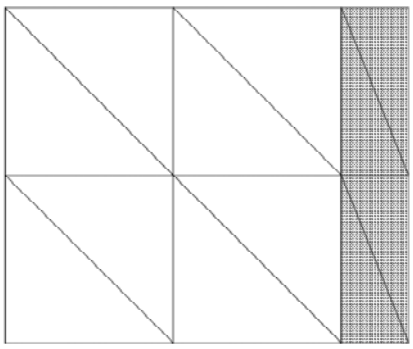

Figure 3.1 Example geometry 1 consisting of a stack of sheets and a coil.

Table IV Parameters of example geometry 1.

Width of the sheets (m)	1
Height of the sheets (m)	1
Width of the coil (m)	0.2
Height of the coil (m)	1
Depth of the whole geometry (m)	1
Resistance of the coil (μΩ)	75
Number of turns in the coil	1
Thickness of the sheets (mm)	0.65
Electrical conductivity of the sheets (MS/m)	2.5

The boundary conditions of the 2-D plane of *example geometry 1* were set in such a way that the resulting magnetic flux density varied unidirectionally and uniformly. In practice, periodicity constraints were applied to the horizontal boundaries, while, on the vertical boundary on the left-hand side, the nodal values were fixed and those on the vertical boundary on the right-hand could change freely. Furthermore, the meshing of the model was performed by 12 second-order elements with three integration points. As shown in Figure 3.1, out of the elements, eight were located in the sheets and four in the

coil. The magnetic properties of the sheets were covered by the reluctivity and hysteresis-argument curves presented in Figures 3.2–3.4. All of these cubic spline representations were fitted from the magnetization curve shown in Figure 2.12.

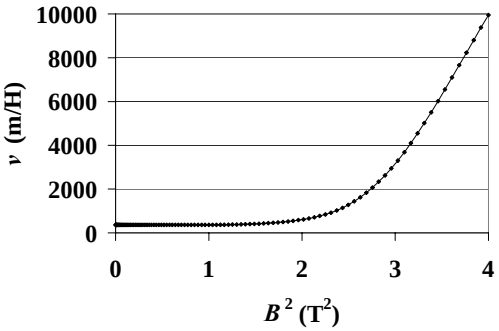

Figure 3.2 Reluctivity as a function of the square of the magnetic flux density. Time-discretized analysis.

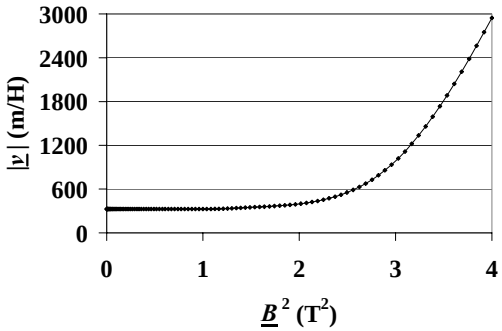

Figure 3.3 Absolute value of reluctivity as a function of the square of the magnetic flux density. Time-harmonic analysis.

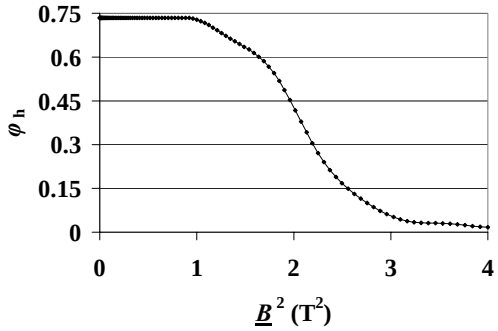

Figure 3.4 Hysteresis part of the argument of the complex reluctivity as a function of the square of the magnetic flux density. Time-harmonic analysis.

The other simple example model, henceforth referred to as *example geometry 2*, was used for the verification of the coupled method. Its 2-D geometry and main parameters are given in Figure 3.5 and in Table V. In order to meet the assumptions of the analytical equations (Vogt, 1983) to which the numerical computations were compared, (i) the reluctivity of the sheets was set to a constant equal to a relative permeability of 1000 and (ii) a uniform, sinusoidally alternating magnetic flux density was created in the stack via the boundary conditions (Pippuri and Arkkio, 2009). The nodal values on the horizontal boundaries of the 2-D geometry were free ones. On the vertical boundaries these were fixed: on the left-hand side to zero and on the right-hand side to the ones of

the driving magnetic flux density. Last, the 2-D mesh comprised eight second-order elements with three integration points.

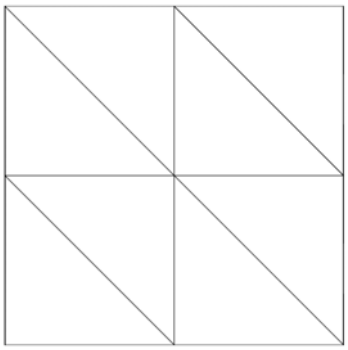

Figure 3.5 Example geometry 2 consisting of a stack of sheets.

Table V Parameters of example geometry 2.

Width of the sheets (m)	1
Height of the sheets (m)	1
Depth of the whole geometry (m)	1
Thickness of the sheets (mm)	0.65
Electrical conductivity of the sheets (MS/m)	2.5

3.1.2 Time-discretized implementation

In this section several issues concerning the accuracy and applicability of the time-discretized implementation of the coupled 2-D–1-D method are addressed. In the first section, the two approaches proposed for representing the 1-D eddy currents in the 2-D model are analyzed and compared. Second, the usability of both the linear and non-linear implementations of the 1-D eddy current modeling is investigated. In particular, the aim is to find suitable areas of application for the linearized approach. In addition, the influence of the magnitude of the magnetic flux density on the accuracy of the coupling of the two models is studied. Last, the correctness of the time-discretized algorithm that was developed is verified by purely analytical derivations of the eddy current losses in a stack of steel laminations.

Conventional and *integration* implementation of the 1-D eddy current solution in the 2-D finite element model

This section is divided into four parts. First, the effect of the upper integration bound of the *integration* approach on the results is investigated. Next, the two coupling techniques are compared in terms of electromagnetic quantities. In the third section, the computational times of the techniques are examined. Finally, the main findings are summarized.

Choosing a proper upper integration bound for the *integration* approach

As is apparent from the section "Definition of H_c", the upper integration bound, z_i, of the *integration* coupling technique is not defined unambiguously. Instead, in principle the bound can be chosen freely within the limits of the solution region of the 1-D problem. Before the two methods of coupling were compared, suitable values for the upper integration bound of the *integration* technique were sought.

The study was carried out by analyzing *example geometry 1*. In order to imitate the distorted flux patterns present in a rotating electrical machine, the system was not fed by a sinusoidal voltage but by the voltage depicted in Figure 3.6. The fundamental component of this is 4000 V (RMS) at 50 Hz. The percentages of the amplitudes of the harmonics from the fundamental component are 8%, 4%, and 2% with frequencies 18, 23, and 36 times the frequency of the fundamental, respectively. Such harmonic components could be involved, for instance, with a frequency-converter supply.

During every simulation, altogether three periods of the supply voltage, 0.06 s, were completed using a time-step of 0.05 ms. The average values of different quantities such as powers were integrated from the results of the last computed period. In order to comprehensively study the influence of the upper integration bound on the results of the *integration* approach, first-, second- and third-order 1-D elements were employed for the space-discretization of the eddy current model of the sheets. The numbers of equally sized elements in the 1-D solution sector (half of the thickness of the sheets, 0.325 mm) were six, three, and two with the first-, second- and third-order elements, respectively. Thus, the number of nodes in the mesh was kept constant. Throughout the study the 1-D model was utilized in the non-linear manner. To ensure the convergence of the computation, a relaxation factor, χ, of 0.3 was used.

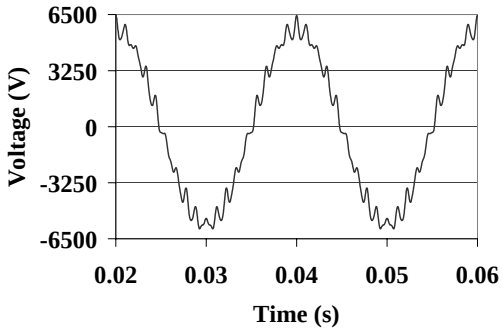

Figure 3.6 Input voltage waveform with a fundamental component of 4000 V (RMS) at 50 Hz.

Three different values of the upper integration bound denoted by z_i were considered. As the lower integration bound, $-d$, was −0.325 mm, the upper integration bounds of (−0.325 + 0.325/3) mm, (−0.325 + 0.325 · 2/3) mm, and 0 mm were chosen to be examined. The results obtained with different orders of 1-D elements are shown in Figures 3.7–3.9 and Tables VI–VIII. The errors in the power balance given in Tables VI–VIII are defined as the difference between the input power and the total losses divided by the input power. In addition, the eddy current losses presented in Tables VI–VIII are calculated from the eddy current density.

As can be observed from Figures 3.7–3.9 and Tables VI–VIII, the upper integration bound does not greatly affect the losses arising in the simple example geometry. The resistive losses in the coil are, according to all the cases that were studied, 3302 W. In the eddy current losses, small deviations are observed. Their largest value, 78007 W, is obtained with the first-order 1-D elements and an upper integration bound of 0 mm. Furthermore, the smallest of these are when the second-order 1-D elements with the upper integration bound are utilized (−0.325 + 0.325/3) mm, 76535 W. Hence, the largest estimate is 1.9% greater than the smallest one.

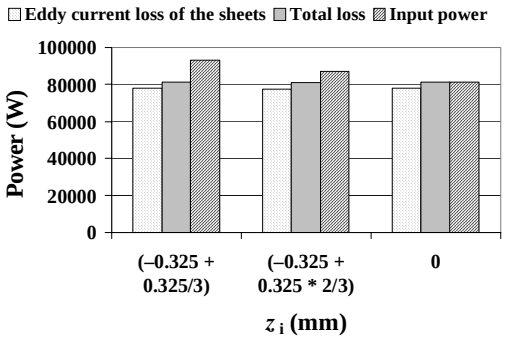

Figure 3.7 Losses and input power with first-order 1-D elements.

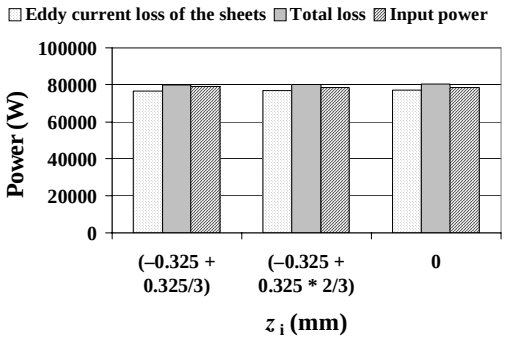

Figure 3.8 Losses and input power with second-order 1-D elements.

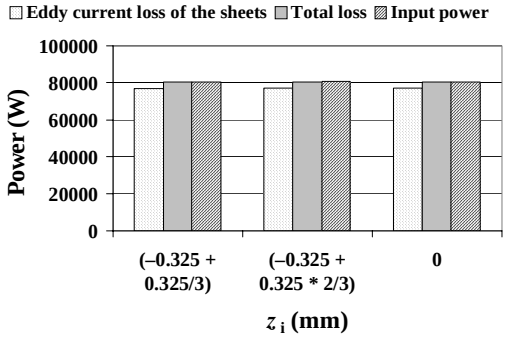

Figure 3.9 Losses and input power with third-order 1-D elements.

Table VI Losses, input power, and power balance with six equally sized first-order 1-D elements.

z_i (mm)	(−0.325 + 0.325/3)	(−0.325 + 0.325 · 2/3)	0
Eddy current loss of the sheets (W)	77939	77587	78007
Resistive loss of the coil (W)	3302	3302	3302
Total loss (W)	81241	80888	81309
Input power (W)	93144	87023	81353
Difference between the input power and total loss (W)	11903	6135	44
Error in the power balance (%)	12.78	7.05	0.05

Table VII Losses, input power, and power balance with three equally sized second-order 1-D elements.

z_i (mm)	(−0.325 + 0.325/3)	(−0.325 + 0.325 · 2/3)	0
Eddy current loss of the sheets (W)	76535	76961	77141
Resistive loss of the coil (W)	3302	3302	3302
Total loss (W)	79836	80262	80442
Input power (W)	79004	78642	78630
Difference between the input power and total loss (W)	−833	−1620	−1812
Error in the power balance (%)	−1.05	−2.06	−2.30

Table VIII Losses, input power, and power balance with two equally sized third-order 1-D elements.

z_i (mm)	(−0.325 + 0.325/3)	(−0.325 + 0.325 · 2/3)	0
Eddy current loss of the sheets (W)	77005	77115	77057
Resistive loss of the coil (W)	3302	3302	3302
Total loss (W)	80306	80417	80359
Input power (W)	80560	80601	80542
Difference between the input power and total loss (W)	254	184	183
Error in the power balance (%)	0.32	0.23	0.23

While the computed losses are not significantly affected by the upper integration bound applied, the input power and, thus, also the power balance of the method are. As can be seen from Figure 3.9 and Table VIII, the coupling of the eddy current phenomena to the 2-D analysis succeeds well in general with the third-order 1-D elements. With all the upper integration bounds considered, the total losses of the system are in agreement with its input power. Thus, the error in the power balance remains small too; it is 0.32% at the most.

On the contrary, if the first-order 1-D elements are applied, a proper selection of the upper integration bound becomes essential. The results obtained with the first-order 1-D elements are shown in Figure 3.7 and Table VI. Obviously, the greater the integration interval is, the better the power balance is fulfilled. With the upper integration bounds (−0.325 + 0.325/3) mm and (−0.325 + 0.325 · 2/3) mm, the input power of the system becomes overestimated, thus resulting in substantial errors in the power balance. By increasing the integration interval by utilizing the upper integration bound of 0 mm, the accuracy of the coupling can be improved and the error in the power balance reduced to 0.05%.

Analyzing the results obtained with the second-order 1-D elements, it is observed that most of these are better in terms of power balance than the ones computed with the first-order 1-D elements. In contrast to the first-order 1-D elements, the accuracy is improved when the integration interval is shortened, as depicted in Figure 3.8 and Table VII. In addition, when the second-order 1-D elements are utilized the input power of the system is slightly underestimated – not overestimated as it is with the other degrees of the 1-D elements. This is also the reason for the negative signs in the errors of the power balance.

Comparison between the *conventional* and *integration* approaches

Besides the *integration* one, the *conventional* approach was proposed for combining the 1-D eddy current solution of the electrical steel sheets with the 2-D finite element analysis. Next, the two techniques are compared. While the *integration* approach is given by Equations (2.94) and (2.95), in the *conventional* coupling, the magnetic field strength at the boundary of the sheets is calculated as a product of the magnetic flux density and reluctivity.

Exactly the same problem of *example geometry 1* as above with the *integration* one was analyzed using the *conventional* technique. All the settings and inputs were the same as above, except that the coupling of the 2-D and 1-D models was performed differently. The eddy current losses in the stack of the sheets, the total losses, and the input powers obtained with the different orders of the 1-D elements are illustrated in Figure 3.10. The numerical values of those quantities with the errors in the power balance are given in Table IX. It can be seen from Figure 3.10 and Table IX that when the first-order 1-D elements are associated with the *conventional* technique the coupling of the eddy current phenomena to the 2-D model fails. The error in the power balance is as much as −30%. The reason for this is that the magnetic field strength at the boundary of the sheets $\boldsymbol{h}(-d,t)$ that is evaluated from a certain 1-D field distribution is not able to represent the total eddy current loss related to the same distribution. The portion of the total eddy current losses included in the 2-D field analysis can be calculated from the ***B*-*H*** loops depicted in Figures 3.11 and 3.12. With the first-order 1-D elements, the losses integrated from the ***B*-*H*** loop are about 75% of those computed from the eddy current

density. It was also found that in the case of the first-order 1-D elements even the tripling of their number from six to 18 does not result in sufficient accuracy. The error in the power balance is still as high as 8.2%. Hence, it is justified to state that the fast changes of the magnetic field strength near the boundaries of the sheets cannot be traced with the linear first-order 1-D elements with sufficient accuracy.

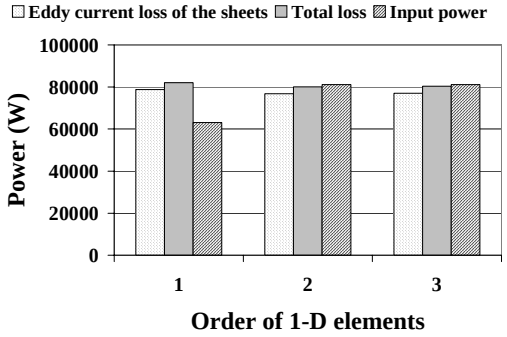

Figure 3.10 Losses and input power utilizing the conventional approach.

Table IX Losses, input power, and power balance when utilizing the conventional approach.

Order of 1-D elements	1	2	3
Number of 1-D elements	6	3	2
Eddy current loss of the sheets (W)	78757	76765	77047
Resistive loss of the coil (W)	3302	3302	3302
Total loss (W)	82059	80067	80349
Input power (W)	63057	81135	81135
Difference between the input power and total loss (W)	−19001	1068	786
Error in the power balance (%)	−30.13	1.32	0.97

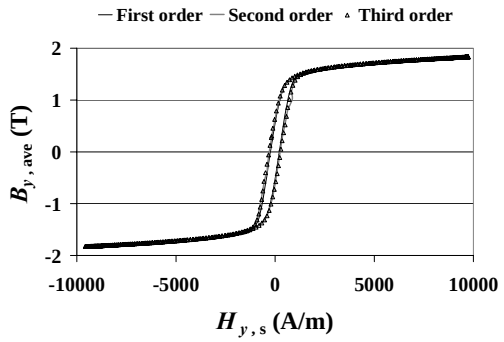

*Figure 3.11 **B**-**H** loops for the conventional approach.*

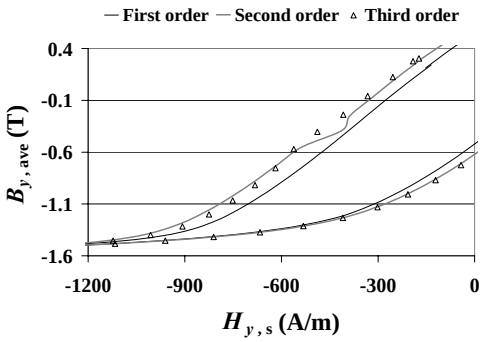

*Figure 3.12 **B**-**H** loops for the conventional approach, a close-up.*

Applying the second-order 1-D elements with the *conventional* approach yields a considerable improvement in the accuracy of the coupling of the 2-D and 1-D formulations. As depicted in Figure 3.10, the input power agrees well with the total losses. Thus the error in the power balance is small, 1.3%. However, some numerical instability occurs during the simulation, leading to the divergence of the computation at eight time-steps out of the total of 1200 time-steps. This can be observed from Figure 3.12. In the ***B*-*H*** loop, a visible deviation from the general trend of the curve is seen, for instance, at −410 A/m. The convergence properties of the computation could have been enhanced by a lower value of the relaxation factor χ. Decreasing χ, however, increases the computational burden. The convergence is slower, i.e., more iterations are required per time-step. As convergence problems were only encountered in the case of the second-order 1-D elements, utilizing a smaller χ was considered to be unnecessary in this connection.

The precision of the coupling can be improved even further by utilizing the third-order 1-D elements in association with the *conventional* technique. The error in the power balance is then reduced to 1%. The stability of the computation improves, too, in comparison with the second-order 1-D elements. Hence the utilization of the third-order 1-D elements is preferable with the *conventional* approach.

Next the characteristics of the *conventional* and *integration* method are compared. With the *integration* approach, the computations were carried out utilizing three different upper integration bounds in association with each of the orders of the 1-D elements. Now, of the results obtained with a certain order of the 1-D elements, those having the smallest error in the power balance are chosen for the comparison. Thus, for the first- and third-order 1-D elements an upper integration bound of 0 mm is used. With the second-order 1-D elements, on the other hand, applying an upper integration bound of −0.325 + 0.325/3 mm results in the best power balance.

The total losses, i.e., the sum of the eddy current losses in the sheets and the DC resistive losses of the coil, and the input powers computed with the *conventional* and *integration* approaches, are depicted in Figure 3.13. As can be seen from Figure 3.13, the higher the order of the 1-D elements is, the better the agreement of the total losses from the two coupling methods is. The differences observed originate fully from the eddy current losses of the sheets as the DC resistive losses of the coil have the same value, regardless of the coupling or the order of the 1-D elements utilized. At the most, the relative difference between the eddy current losses from the *conventional* and *integration* approaches is 1.0%. This discrepancy occurs with the first-order 1-D elements when the accuracy, i.e., the power balance provided by the *conventional* technique, is the poorest and that by the *integration* approach the best. Hence the success of the coupling of the 2-D and 1-D models has only a slight effect on the magnitude of the losses.

While the total losses from the *conventional* and *integration* approaches correspond well throughout the study, the input powers do not, as can be seen from Figure 3.13. When the first-order 1-D elements are applied, the *conventional* approach yields an es-

timate that is 22% less than the one from the *integration* technique. The reason for the difference is the inappropriateness of the *conventional* approach in connection with the first-order elements. As the order of the 1-D elements is increased, the correspondence between the two methods improves. With the second-order elements, the input power of the *conventional* approach is 2.7% greater than that from the *integration* one, whereas in the case of the third-order elements the results are practically equal.

In addition to the total losses and input powers, the input currents and power factors were also compared. The currents are presented in Figure 3.14 and the power factors in Figure 3.15. As Figure 3.14 shows, the currents flowing in the coil are not notably affected by the method of the coupling or the order of the 1-D elements. However, the power factor is. As can be observed from Figure 3.15, the results obtained mostly correspond well. Anyhow, it becomes evident in the power factor if the coupling of the 1-D and 2-D models does not succeed with sufficient accuracy. The greatest difference between the two coupling methods occurs with the first-order 1-D elements, when the *conventional* technique operates the worst.

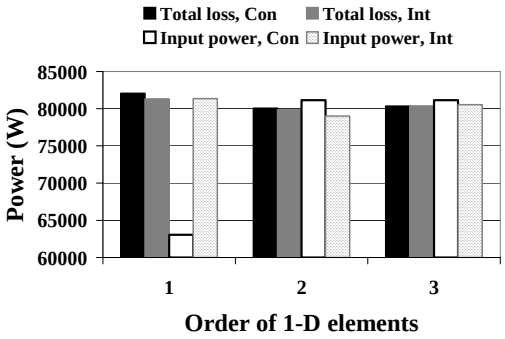

Figure 3.13 Total losses and input powers obtained with the conventional (Con) and integration (Int) approach.

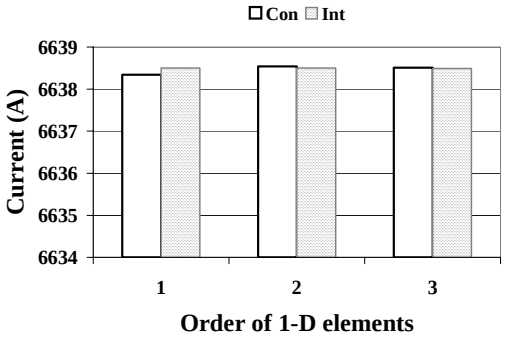

Figure 3.14 Currents in the coil obtained with the conventional (Con) and integration (Int) approach.

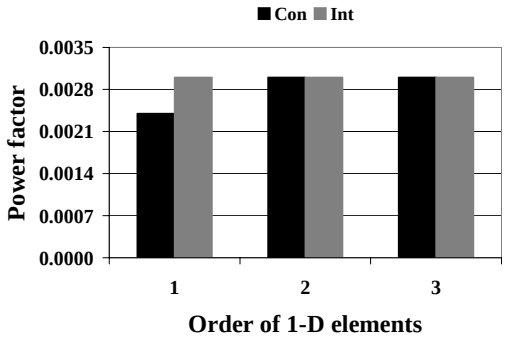

Figure 3.15 Power factors obtained with the conventional (Con) and integration (Int) approach.

Computational efficiency

In addition to the accuracy of the results, the computational efficiency of the two coupling approaches under investigation is of great interest. Next, these two are compared in terms of computational time. The average computing times for one period of line voltage, the average computing times for constructing a 2-D system matrix, and the average numbers of iterations per time-step are collected in Table X. As can be seen from Table X, the comparison was carried out for the same group of results as above. The simulations were run on a PC with a 2.66-GHz processor and 1.95 GB of RAM.

The average computing times for constructing a 2-D system matrix are rather similar, the *integration* approach being slightly slower than the *conventional* one. At the most, the difference is 4%. This, however, does not lead to a better overall performance of the *conventional* approach in all the cases that were studied. With the second-order 1-D elements, when the convergence properties of the *conventional* approach are reduced, the computing times of one period of line voltage are favorable to the *integration* approach.

The numbers of nodes in the 2-D and 1-D meshes were kept constant in each of the simulations. Nevertheless, the computation times of both coupling approaches were observed to increase along with the order of the 1-D elements. For instance, when the third-order 1-D elements are applied instead of the first-order ones, the computation time of one period is increased by approximately 13% with both techniques.

Table X Computation times for the conventional and integration approach.

Order of 1-D elements	1		2		3	
Number of 1-D elements	6		3		2	
Method of coupling	*Conventional*	*Integration*	*Conventional*	*Integration*	*Conventional*	*Integration*
z_i (mm)	-	0	-	(−0.325 + 0.325/3)	-	0
CPU time per period of line voltage (s)	20.58	21.57	25.18	23.27	23.35	24.39
Average CPU time for constructing a 2-D system matrix (ms)	1.444	1.481	1.511	1.560	1.619	1.687
Average number of iterations per time-step	34	34	38	35	34	34

Conclusion

The results of the above comparative study can be concluded as follows.

- When the first-order 1-D elements are applied, the integration interval of the *integration* approach (Equations (2.120) and (2.121)) should be the whole 1-D solution sector (i.e., half of the thickness of the laminations), whereas with the second-order 1-D elements it should be kept as short as possible. With the third-order 1-D elements the reliability of the coupling did not depend heavily on the upper integration bound applied. Hence it can be chosen freely.

- Both methods discussed, the *conventional* and *integration* one, can be used for representing the 1-D eddy current solution of the sheets within the 2-D equations if the order of the 1-D elements is chosen suitably. In the case of the *conventional* approach, the utilization of the second- or third-order 1-D elements provides sufficient accuracy for the power balance. However, better numerical stability of the computation can be achieved with the third-order 1-D elements. Hence their application is recommended. In comparison with the *conventional* approach, the *integration* approach also couples the 1-D solution to the 2-D formulations reliably with the first-order 1-D elements.

- It was found that the order of the 1-D elements applied has a rather important effect on the computation times of the coupled 2-D–1-D method. When the number of nodes in the 1-D mesh is kept unchanged but the third-order elements are utilized instead of the first-order ones, the computing times are lengthened by 13%. This concerns both the coupling techniques investigated. The *integration* approach also yields a satisfactory power balance and computational stability with the first-order 1-D elements and, thus, appears to be preferable.

Linear and non-linear implementation of the 1-D eddy current model

As discussed above, the 1-D eddy current model of the electrical steel sheets was implemented in a linear and non-linear manner in the time-discretized computational scheme. Next, the applicability of those two implementations to different modeling problems is investigated. In the first section, the effects of the implementations on the electromagnetic quantities are studied. The second section discusses their computational efficiency. Last, in the third section, the main findings are summarized.

Comparison between the linear and non-linear implementations

The features of the linear and non-linear implementations of the 1-D eddy current model of the steel sheets are investigated via the model *example geometry 1*, with the exception being that the thickness of the sheets in the stack is altered. The same input voltage waveform, time-discretization, and iterative schemes as above in the sections “Choosing a proper upper integration bound for the *integration* approach” and “Comparison be-

tween the *conventional* and *integration* approaches" are applied, as well as both the coupling techniques, *conventional* and *integration*.

Five different types of electrical steel sheets were included in the study. The electrical conductivity of all of these was 2.5 MS/m but their thicknesses varied from 0.35 to 2 mm. The orders and numbers of the 1-D elements and relaxation factors, χ, used in each of the computations are collected in Table XI. Table XI also shows an estimate for the skin depth of the sheets, which was evaluated at a frequency of 1800 Hz, with a reluctivity of 365 m/H. These two values comprise the "worst-case scenario" for the problem considered here, in terms of skin depth. The space-discretization of the 1-D model was adjusted according to the ratio of the sheet thickness to the skin depth. Those ratios are presented in Table XI. Last, χ in the case of all the sheet types was fixed to the largest possible value that still ensures the convergence of the computation with the non-linear implementation of the 1-D model. Reasonably, the more dominant the eddy current phenomenon, the lower the χ applied is.

Table XI Parameters used in the computations with both implementations of the eddy current model of the sheets, linear and non-linear.

Thickness of the sheets (mm)	0.35	0.50	0.65	1.00	2.00
Order of 1-D elements	3	3	3	3	3
Number of 1-D elements	2	2	2	3	6
Skin depth (mm)			0.1607		
Thickness of the sheets divided by the skin depth	2.18	3.11	4.04	6.22	12.44
χ	0.80	0.40	0.30	0.10	0.03

The main results of the investigation are shown in Figures 3.16–3.20. The eddy current losses obtained with both couplings and eddy current model implementations are plotted in Figure 3.16 as a function of the ratio of the thickness of the sheets to the skin depth. Clearly, the influence of the linearization of the 1-D equations on the eddy current losses is rather exiguous. With both couplings, the losses from the non-linear implementation are slightly larger than those from the linear implementation. The greatest differences occur with the 1-mm sheets. With the *conventional* approach the non-linear implementation results in eddy current losses 4% greater than the linear implementation. For the *integration* coupling, the corresponding figure is 3%.

The DC resistive losses of the coil are plotted in Figure 3.17. Those are practically independent of the implementation of the eddy current model. The greatest discrepancy occurs with the thickest sheet type, where the results obtained with the non-linear implementation are found to be 0.2% greater than those from the linear implementation. This applies to both the coupling methods.

As the 1-D modeling of the sheets is directly coupled to the 2-D formulae, its linearization has an impact on the whole computation, also on the loss components that are obtainable by post-processing. Next, particularly, the dependency of the hysteresis and excess losses (Equations (2.128) and (2.131)) on the linearization is investigated. The sum of the hysteresis and excess losses as a function of the ratio of the sheet thickness to the skin depth is presented in Figure 3.18. The results in Figure 3.18 were computed using values 112.1604 W/m^3 and 1.2995 W/m^3 for the hysteresis and excess-loss coefficients, k_h and k_{ea}, respectively. The fitting of these parameters was carried out in the least-squares sense employing the data of the sample R1382. It can be observed from Figure 3.18 that the linearization of the eddy current model does not have a notable effect on the result if the sheet thickness to skin dept ratio does not exceed 4.5. After that point, the nonlinear implementation starts to slightly differ from the linear one, the greatest

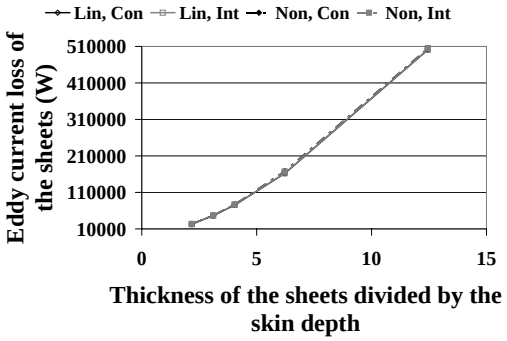

Figure 3.16 Eddy current losses of the sheets obtained with the conventional (Con) and integration (Int) approach employing the linear (Lin) and non-linear (Non) implementation.

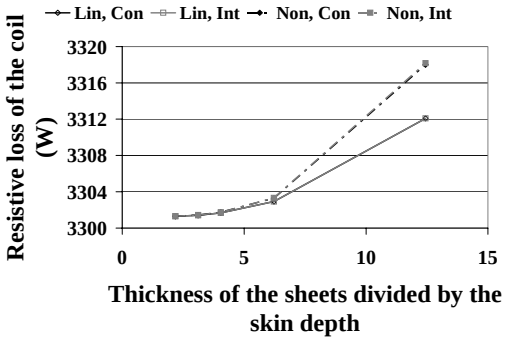

Figure 3.17 DC resistive losses of the coil obtained with the conventional (Con) and integration (Int) approach employing the linear (Lin) and non-linear (Non) implementation.

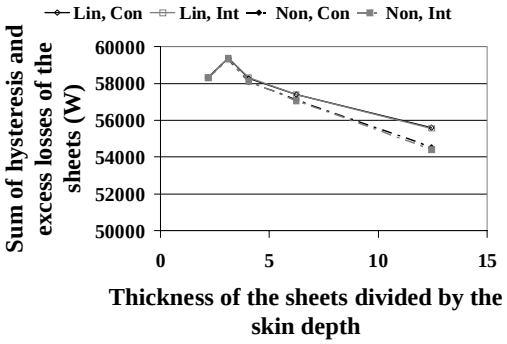

Figure 3.18 Sum of hysteresis and excess losses obtained with the conventional (Con) and integration (Int) approach employing the linear (Lin) and non-linear (Non) implementation.

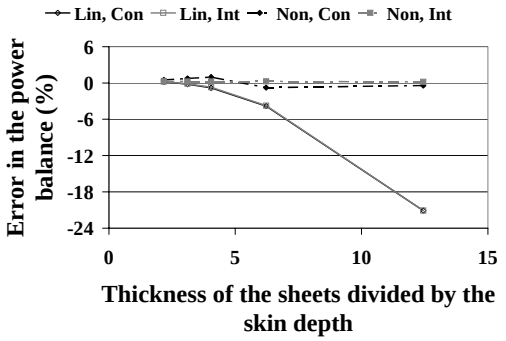

Figure 3.19 Errors in the power balance obtained with the conventional (Con) and integration (Int) approach employing the linear (Lin) and non-linear (Non) implementation.

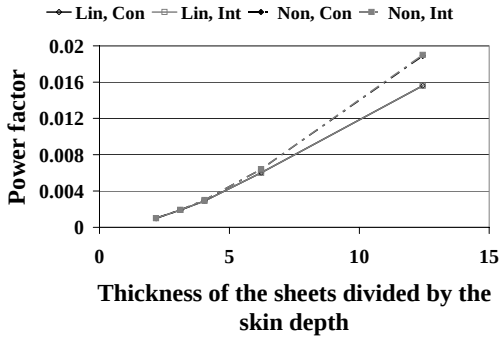

Figure 3.20 Power factors obtained with the conventional (Con) and integration (Int) approach employing the linear (Lin) and non-linear (Non) implementation.

difference with both the coupling techniques at the most being approximately 2%. Clearly, when the eddy current phenomenon of the sheets is more dominant its nonlinear modeling seems to capture its damping effects on the field more efficiently.

Figure 3.19 shows the errors in the power balance from the computations performed. As observed from Figure 3.19, the two coupling methods, *conventional* and *integration*, provide similar results in the case of the linear and non-linear implementations. If the analysis encompasses the modeling of the true magnetic properties of the materials, the coupling of the 1-D and 2-D formulations succeeds well with all the sheet types investigated. The absolute values of the error in the power balance vary from 0.42 to 0.97 with the *conventional* approach and from 0.18 to 0.31 with the *integration* approach. The linearly implemented 1-D model performs with an accuracy comparable to the non-linearly realized one if the ratio of the sheet thickness to the skin depth is below 4.5. After that point, the error in the power balance starts to increase gradually, as can be seen from Figure 3.19. The performance of the linear 1-D model cannot be significantly improved by finer meshing. Considering the *conventional* technique in connection with the linearized eddy current modeling, increasing the number of the 1-D elements from three to six reduces the error in the power balance from 3.81% to 3.76%. The results from the *conventional* and *integration* methods when the linear implementation of the 1-D model is utilized are almost indistinguishable.

The error in the power balance is present in the values of the power factor, which are depicted in Figure 3.20. As for the error in the power balance, an adequate correspondence between the results from the linear and non-linear implementations of the eddy current model is observed if the ratio of the lamination thickness to the skin depth is approximately below 5.

The ***B-H*** loops traced by the magnetic flux density and magnetic field strength are shown for the 0.65-mm sheets in Figure 3.21. Similar results for the 2-mm sheets are plotted in Figure 3.22. As can be seen from Figure 3.21, no differences can be distinguished between the ***B-H*** loops when the suitable operating ranges of the linearized implementation of the 1-D model are met. With the thickest sheets, on the other hand, clear deviations between the curves are observed. The linear implementation of the 1-D model differs from the non-linear one the most when the time derivative of the magnetic flux density gains its highest values.

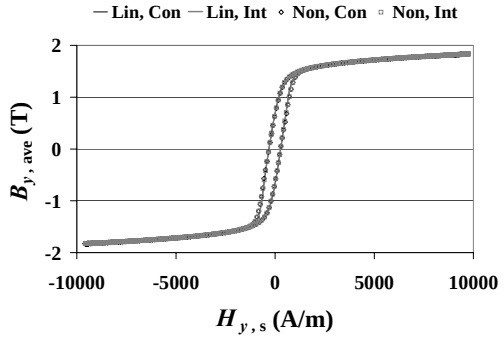

Figure 3.21 ***B-H*** *loops for the conventional (Con) and integration (Int) approach employing the linear (Lin) and non-linear (Non) implementation. Thickness of the sheets 0.65 mm.*

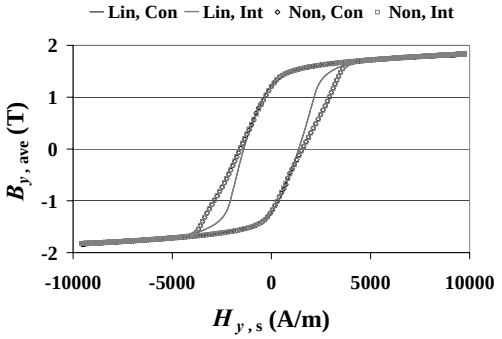

Figure 3.22 ***B-H*** *loops for the conventional (Con) and integration (Int) approach employing the linear (Lin) and non-linear (Non) implementation. Thickness of the sheets 2 mm.*

Computational efficiency

The computational times for the *conventional* and *integration* methods of coupling are collected in Tables XII and XIII. As the space-discretization of the 1-D solution sector

Table XII Computation times for the conventional approach.

Thickness of the sheets divided by the skin depth	CPU time per period of line voltage (s)		Average CPU time for constructing a 2-D system matrix (ms)		Average number of iterations per time-step	
	Linear	Non-linear	Linear	Non-linear	Linear	Non-linear
2.18	2.88	6.61	0.6	1.7	8	8
3.11	7.18	16.64	0.7	1.6	24	24
4.04	10.13	23.50	0.7	1.6	34	34
6.22	49.15	125.32	1.0	2.6	116	117
12.44	421.10	1390.63	2.5	8.3	409	410

Table XIII Computation times for the integration approach.

Thickness of the sheets divided by the skin depth	CPU time per period of line voltage (s)		Average CPU time for constructing a 2-D system matrix (ms)		Average number of iterations per time-step	
	Linear	Non-linear	Linear	Non-linear	Linear	Non-linear
2.18	3.08	6.80	0.7	1.8	8	8
3.11	7.83	17.57	0.7	1.7	24	24
4.04	10.83	24.36	0.7	1.7	34	34
6.22	51.32	127.30	1.1	2.7	116	117
12.44	429.14	1391.94	2.6	8.4	409	410

was the same with both the methods, the results provided by these are practically equivalent. In comparison with the non-linear one, the linear implementation of the 1-D model guarantees significantly lower computational times. The more substantial the eddy current phenomenon in the sheets, the greater the discrepancy between the implementations is. At the most, the computational time of the non-linear implementation is over three times longer than that of the linear implementation. As expected, the decrease of the relaxation factor, χ, substantially affects the number of iterations per time-step. Hence, χ should be kept as high as possible.

Conclusion

The main observations of this section can be summarized as follows.

- When the actual magnetic properties of the sheets are modeled, i.e., the non-linear 1-D model is employed, both the *conventional* and *integration* techniques succeed in the coupling with sufficient accuracy within a wide range of different steel sheet types.

- When the linearly realized 1-D model is utilized, the *conventional* and *integration* techniques provide results that are almost indistinguishable from each other. In addition, it was found that the linearized approach to the eddy current modeling is well suited to problems for which the skin depth is larger than one fifth of the thickness of the sheet. Within a suitable operating range, an accuracy of the coupling which accords with that from the non-linear approach is obtained with the linear implementation.

- The linear and non-linear realizations of the 1-D model provide very similar estimates of the eddy current losses, regardless of the success of the 1-D–2-D coupling.

- Whenever practicable, the linear implementation of the 1-D model should be utilized because of its superior computational efficiency. Moreover, when an application as complex as, for instance, a rotating electrical machine is being studied, the consideration of the true magnetic properties of the sheets may turn out not to be feasible when the linearized 1-D eddy current modeling must be enforced despite its limitations.

- The number of iterations per time-step increases rapidly with the decrease of χ. Thus, it should be adjusted to the largest value possible, according to the requirements of the task in hand.

Effect of the magnitude of the magnetic flux density on the coupling of the 2-D and 1-D models

The magnitude of the magnetic flux density at the boundary of the sheets influences the accuracy of the coupling of the 1-D and 2-D models. This issue is analyzed next in the frame of the example problem *example geometry 1* (Section 3.1.1). The same time-discretization and iterative schemes as previously are used. The solution region of the 1-D eddy current model (half of the sheet thickness, 0.325 mm) is discretized with two third-order 1-D elements. The flux level in the system under study *example geometry 1* is controlled through the input voltage. In this investigation, four input voltages are employed. One of these is that shown in Figure 3.6. The other three are formed similarly but their fundamental components are 100 V (RMS), 500 V (RMS), and 2000 V (RMS), all at 50 Hz.

The computations were carried out with both the linear and non-linear implementations of the eddy current model. As in the preceding investigations, the discrepancies between the losses from the *conventional* and *integration* methods were observed to be small. The results of main interest, the errors in the power balance, are presented in Figure 3.23. The flux patterns provided by the *integration* approach combined with the non-linear implementation of the 1-D model are shown in Figure 3.24. According to Figure 3.23, the reliability of the coupling depends somewhat on the flux levels. The peak values of the magnetic flux density at the voltages 100 V (RMS), 500 V (RMS), 2000 V (RMS), and 4000 V (RMS) are 0.3 T, 1.3 T, 1.7 T, and 1.8 T, respectively. When the input voltage is approximately below 500 V (RMS), the results from the two couplings and eddy current model implementations are in good agreement with each other. As the input voltage is increased, differences begin to appear. The *conventional* and *integration* techniques in connection with the non-linear 1-D model yield nearly equal couplings of the 2-D and 1-D models. In the case of the linearized 1-D model, the agreement between those two methods is notably poorer. However, to summarize, although the error in the power balance increases as the flux levels get higher, even its greatest values are acceptable.

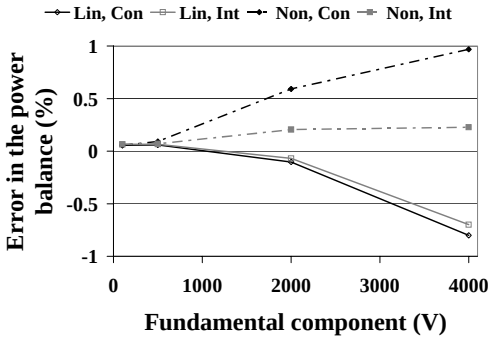

Figure 3.23 Error in the power balance as a function of the fundamental component of the input voltage. Conventional (Con), integration (Int), linear (Lin) and non-linear (Non).

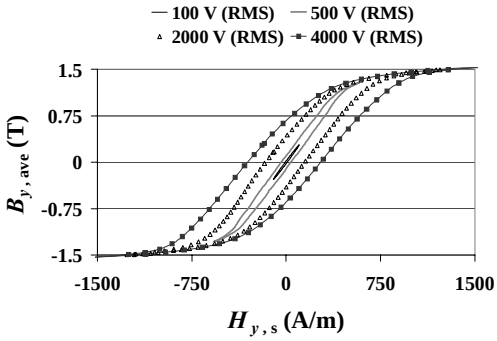

*Figure 3.24 **B**-**H** loops for the integration approach employing the non-linear implementation.*

Verification

A purely analytical formulation of the eddy current losses in a stack of steel sheets (Vogt, 1983) is used to verify the computational algorithm of the time-discretized implementation of the coupled 2-D–1-D method. The eddy current losses in the stack are first evaluated with both the analytical derivations and the proposed numerical method. For the computations, the model *example geometry 2* is employed. A comparative study of the results obtained yields information on the correctness of the implementation of the numerical method.

The computations were conducted using the linear implementation of the 1-D eddy current model and under-relaxation, and with χ having as large a value as was practical. For the space-discretization of the 1-D solution sector (half of the sheet thickness, 0.325 mm), three equally sized third-order elements were applied. The time-discretization was performed with 400 time-steps per period and a total of 1200 time-steps. The average values were integrated over the third period.

The eddy current losses in the stack were calculated at exciting frequencies ranging from 0 to 1000 Hz, applying the analytical equations and both the numerical implementations, *conventional* and *integration*. As the third-order 1-D elements were employed, the upper integration bound of the *integration* approach was set to 0. The amplitude of the driving magnetic flux density was fixed to 1 T. The eddy current losses obtained are shown in Figure 3.25 in W/kg. The value used for the mass density of the sheets was 7800 kg/m^3. The relative differences between the numerical and analytical results are shown in Figure 3.26.

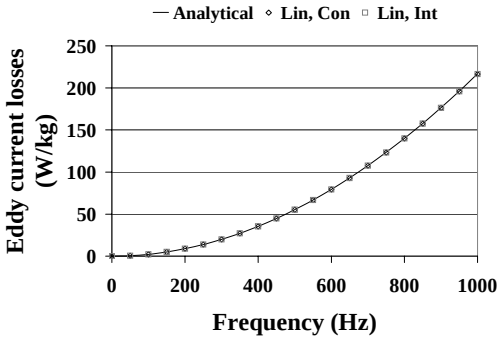

Figure 3.25 Eddy current losses of the stack of the steel laminations in W/kg. Conventional (Con), integration (Int), and linear (Lin).

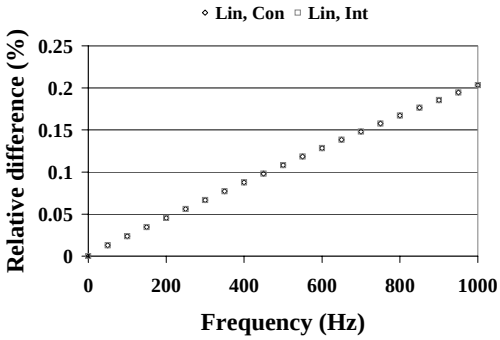

Figure 3.26 Relative differences between the eddy current losses.

Clearly, the eddy current losses from the 2-D–1-D method with both the coupling techniques correspond well with those obtained by the analytical formulations. The relative difference between the results is 0.2% at most. The increase in the relative difference as the frequency increases is related to the utilization of the same time- and space-discretizations throughout the study. For instance, if the operating point of 1000 Hz is computed without changing the space-discretization but by employing 2000 time-steps per period, the value of the relative difference between the numerical and analytical results is reduced to 0.04%. In conclusion, the computational algorithm of the time-stepping approach proved to be appropriately implemented.

3.1.3 Time-harmonic implementation

This section concentrates on examining the time-harmonic implementation of the coupled model. First, the success of the approach in terms of the power balance is discussed and then a verification of its computational algorithm is performed.

Success of the coupling

The time-harmonic 2-D–1-D method includes the eddy currents and hysteresis in the sheets in the 2-D finite element analysis through the complex reluctivity. Next, the reliability of this coupling is studied. The model *example geometry 1* is suitable for this purpose. Altogether, three points are simulated using different input voltages one by one. Hence, the consecutive solution of the different components is omitted and fields varying at a single frequency are considered (Γ is equal to 1). Last, the number of calculation points in the 1-D eddy current model is seven.

The results obtained are collected in Table XIV. As can be seen from Table XIV, the coupling of the hysteresis and eddy current phenomena with the 2-D equations succeeds with reasonable accuracy. Up to 100 Hz, the error in the power balance is below 0.85%. As the frequency increases, higher but still acceptable discrepancies occur.

Table XIV Losses, input power, power factor, and power balance for the time-harmonic approach under different voltage supplies.

Voltage (V)	2000	1000	500
Frequency (Hz)	50	100	200
Current (A)	2981	589	120
Power factor	0.01	0.17	0.47
Hysteresis loss of the sheets (W)	43475	58083	12229
Eddy current loss of the sheets (W)	16211	43138	17563
Resistive loss of the coil (W)	666	26	1
Total loss (W)	60352	101247	29792
Input power (W)	60339	100401	28311
Difference of input power and total loss (W)	−13	−846	−1481
Error in the power balance (%)	−0.02	−0.84	−5.23

Verification

The computational algorithm of the time-harmonic 2-D–1-D method is verified in a manner similar to that of the time-discretized one. The eddy current losses of the stack are first computed by the proposed time-harmonic method, and are then compared with those attainable by the purely analytical formulations (Vogt, 1983).

The model *example geometry 2* was utilized for the investigation. The assumptions of the analytical formulae (Vogt, 1983) were fulfilled in the manner discussed in 3.1.1. The exciting magnetic flux density on one boundary of the 2-D geometry was set to vary at a single frequency, i.e., the number of harmonics Γ during the simulations was 1 (Pippuri and Arkkio, 2009). Within the 1-D solution sector, 10 calculation points were employed (for the space-discretization of the 1-D model in time-harmonic analysis see Section 2.1.1).

The eddy current losses from the numerical time-harmonic approach and from the analytical formulae are depicted in Figure 3.27 in W/kg. The mass density of the sheets was set to 7800 kg/m^3. In all the simulations, the amplitude of the driving magnetic flux density was 1 T but its frequency was varied from 0 Hz to 1000 Hz. The relative differences between the numerical and analytical results are presented in Figure 3.28. As Figure 3.27 shows, the agreement between the eddy current losses obtained by the two formulations is good. The discrepancy between the results increases slightly with the

exciting frequency. This is a result of the space-discretization applied. The correspondence of the numerical and analytical calculations can be further improved by utilizing a greater number of computation points for the 1-D model. Anyhow, the implementation of the time-harmonic approach was proven to be properly performed.

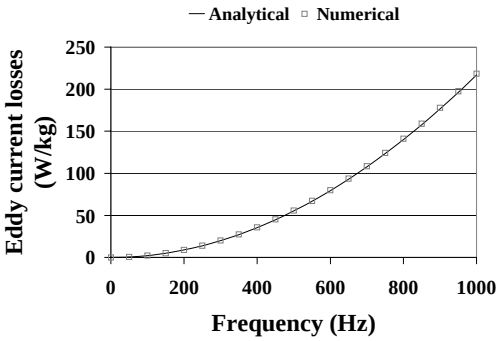

Figure 3.27 Eddy current losses of the stack of the steel laminations in W/kg computed by analytical equations and by the time-harmonic 2-D–1-D model.

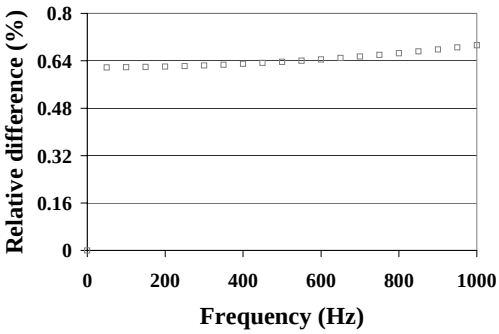

Figure 3.28 Relative differences between the eddy current losses obtained by analytical equations and by the time-harmonic 2-D–1-D model.

3.2 Application to induction motors

In this section, simulations carried out on the test motor are elaborated and analyzed. The slip-control, no-load, and load conditions are investigated. The performance of both the time-discretized and time-harmonic algorithms is dissected. The measurement results verify the applicability of the methods that were developed.

3.2.1 Parameters of the iron-loss models and magnetic material properties of the steel sheets

The reluctivity curve employed in the time-discretized analysis for both the stator and rotor sheets is depicted in Figure 3.2. The function of the absolute value of the reluctivity needed for the time-harmonic analysis and used in the stator and rotor is shown in Figure 3.3. The hysteresis part of the argument of the complex reluctivity as a function of the square of the magnetic flux density is given in Figure 3.4. It was determined from the measuring data of the wound-ring sample R1382. Thus the hysteresis modeling does not contain any information on rotating fields.

The parameters of the hysteresis and excess-loss models Equations (2.128) and (2.131) were fitted in the least-squares sense by a non-linear curve-fitting algorithm. As the data

of the sample R1382 were utilized, the rotating loss part in Equation (2.128) became neglected. The frequency range of the measurements included was 20–320 Hz. The coefficients used in all the simulations are collected in Table XV.

Table XV Hysteresis and excess-loss coefficients. Mass density 7800 kg/m^3.

Hysteresis-loss coefficient k_h (W/m^3)	112.1604
Excess-loss coefficient k_{ea} (W/m^3)	1.2995

3.2.2 Slip-control test

The measurement results from the slip-control no-load tests of the 37-kW cage-induction machine are used to validate the time-discretized implementation of the machine model that has been presented. The second objective of the study is to verify the observations made from the analyses of the simple example geometries in Section 3.1 with respect to a real rotating electrical machine. Hence, computations employing both the *conventional* and *integration* coupling techniques in association with the linear and non-linear implementations are carried out.

Problem setting

The main parameters of the 37-kW test motor are shown in Table III. The 2-D finite element mesh that was utilized covered one fourth of the cross-section of the motor and consisted of 1686 second-order elements with three integration points. The mesh is shown in Figure 3.29. During each of the simulations, a symmetrical sinusoidal

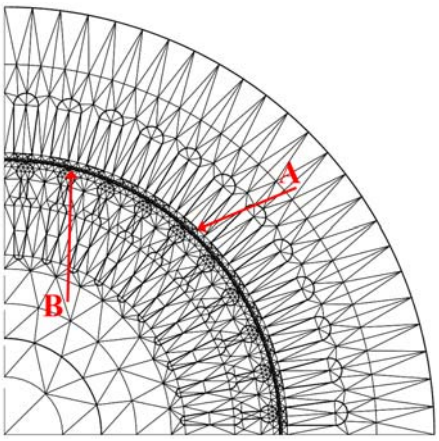

Figure 3.29 Finite element mesh and points A and B where the flux patterns are investigated more closely.

three-phase voltage with a frequency of 50 Hz was fed to the stator winding. The number of time-steps per period was 400 and altogether 4000 steps were computed. The average values of the quantities were integrated over the last computed period. The 1-D geometry was discretized either with six first-order elements or with two third-order elements. The upper integration bound of the *integration* approach was 0 in all simulations as it provides accurate coupling with both the orders of the 1-D elements utilized. The solution of the 2-D equations was performed in the incomplete Newton-Raphson iterative scheme with χ of 0.15. The motor was made to run at zero slip, at synchronous speed with all the supply voltages.

Electromagnetic losses

The total electromagnetic losses attained with the first- and third-order 1-D elements with different implementations are depicted in Figures 3.30 and 3.31. First, let us consider the results obtained with the first-order 1-D elements. As Figure 3.30 shows, the discrepancies between the total electromagnetic losses from the two coupling techniques and eddy current model implementation are very small. The results provided by the non-linear implementation of the eddy current model are at most 0.52% greater than those from the linear implementation. This applies to both the coupling techniques. Importantly, the simulated estimates of the total electromagnetic losses are in sufficient agreement with the measured ones. The greatest discrepancy occurs at 100 V, when the computed losses are 24% lower than the measured ones. At the higher supply voltages the correspondence is much better. For instance, at 300 V, the relative difference between the simulated and measured losses is only 3%. On average, the relative difference between the simulations and measurements is 7.7%.

Similar observations as with the first-order 1-D elements were made in the case of the third-order ones. The simulated total electromagnetic losses are not significantly

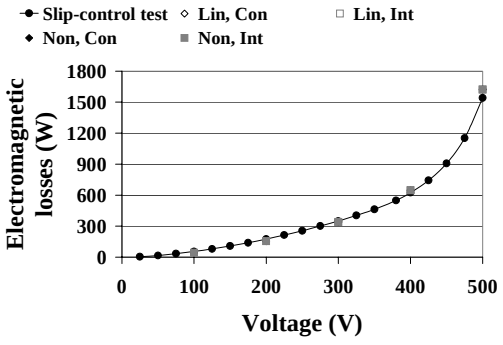

Figure 3.30 Electromagnetic losses with six first-order 1-D elements. Conventional (Con), integration (Int), linear (Lin) and non-linear (Non).

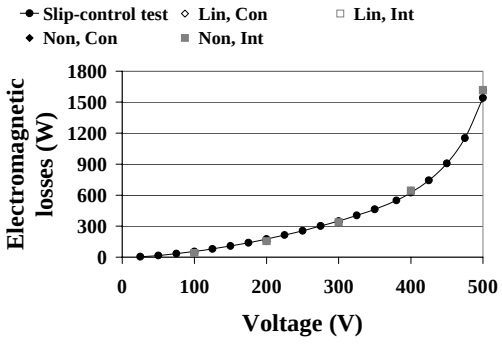

Figure 3.31 Electromagnetic losses with two third-order 1-D elements.

dependent on the coupling technique or on the implementation of the eddy current model. In addition, the results from the non-linear implementation of the 1-D model are consistently slightly larger than those from the linearized one with both the coupling techniques. The agreement between the simulated and measured results from the third-order 1-D elements corresponds with that attained by using the first-order 1-D elements. The relative difference between the computations and experiments is 8.1% on average.

As discussed in Section 2.3.2, the measured total electromagnetic losses can be separated into two components. The DC resistive losses of the stator winding and the loss component referred to as the other electromagnetic losses are depicted in Figures 3.32–3.35. According to Figures 3.32 and 3.33, the first- and third-order 1-D elements provide similar estimates of the other electromagnetic losses. In addition, the simulated

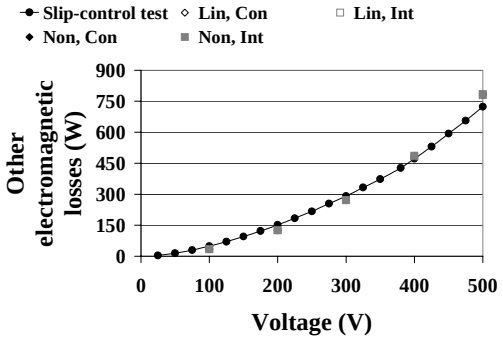

Figure 3.32 Other electromagnetic losses with six first-order 1-D elements. Conventional (Con), integration (Int), linear (Lin) and non-linear (Non).

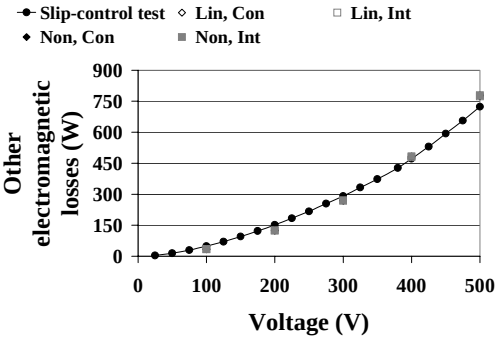

Figure 3.33 Other electromagnetic losses with two third-order 1-D elements.

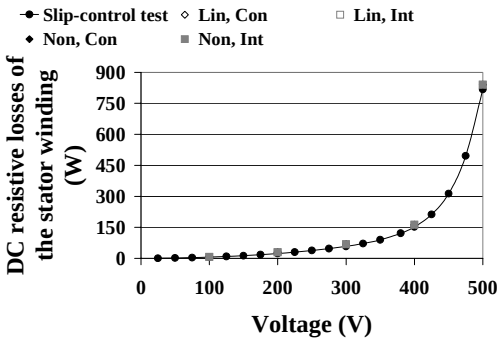

Figure 3.34 DC resistive losses of the stator winding with six first-order 1-D elements. Conventional (Con), integration (Int), linear (Lin) and non-linear (Non).

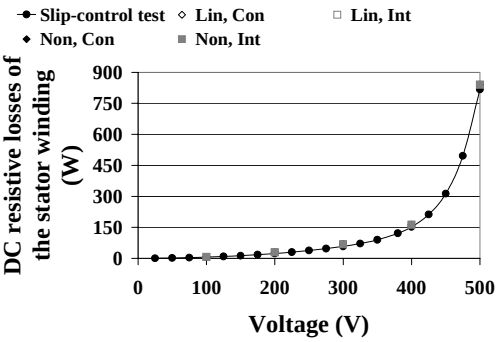

Figure 3.35 DC resistive losses of the stator winding with two third-order 1-D elements.

results agree with reasonable accuracy with the measured ones. When the first-order 1-D elements are applied, the average relative difference between the simulations and experiments is 12.8%. For the third-order 1-D elements, the corresponding figure is 12.9%. As Figures 3.32 and 3.33 show, the other electromagnetic losses are somewhat underestimated when the supply voltage is at most 300 V, while above that limit, they are slightly overestimated.

As can be seen from Figures 3.34 and 3.35, the agreement between the computed and measured DC resistive losses of the stator winding is sufficient. An average of 13.8% for the relative difference between the computations and experiments is attained with both the orders of the 1-D elements. Particularly at lower supply voltages (up to 300 V), the DC resistive losses of the stator winding are overestimated.

The eddy current losses of the sheets from the first- and third-order 1-D elements are compared in Figures 3.36 and 3.37. The results shown were obtained using the *integration* method for the coupling and taking the true magnetic properties of the steel sheets into account. According to Figures 3.36 and 3.37, when the number of nodes in the 1-D mesh is kept constant, changing the order of the elements does not significantly affect the results. Anyhow, the first-order 1-D elements consistently provide larger estimates. The stator eddy current losses from the first-order 1-D elements are at most 1.4% greater than those from the third-order ones. For the rotor side, the corresponding figure is 4.6%. Comparable results were achieved with the other coupling and 1-D model implementation combinations as well.

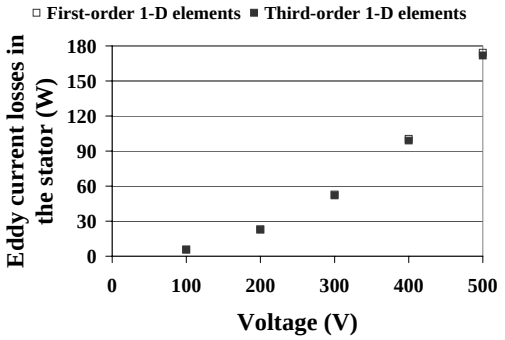

Figure 3.36 Eddy current losses in the stator obtained with first- and third-order elements (integration method, non-linear 1-D model).

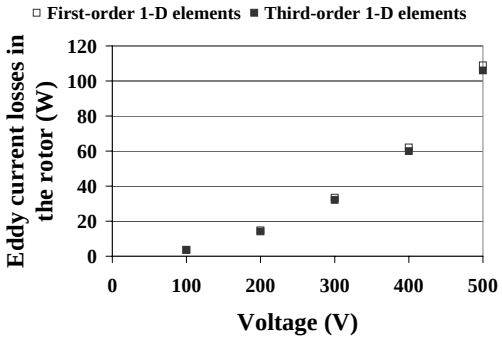

Figure 3.37 Eddy current losses in the rotor obtained with first- and third-order elements (integration method, non-linear 1-D model).

Flux patterns

The ***B-H*** loop and magnetic flux density in the stator tooth tip at point A depicted in Figure 3.29 are shown in Figures 3.38 and 3.39. Similar curves for the rotor side at point B in Figure 3.29 are given in Figures 3.40 and 3.41. The magnetic flux density values are averaged over the thickness of the sheets, whereas the magnetic field strength is from the surface of the sheets. The results shown were obtained with a rated voltage of 400 V, using the first-order elements for 1-D equations in connection with the *integration* technique. As is evident in Figures 3.38 and 3.39, in the stator tooth tips, the flux patterns calculated with the linearized 1-D model are indistinguishable from those from the non-linear one. Similar observations were also made in other parts of the stator. On the rotor side, the ***B-H*** loops from the linear and non-linear modeling were found to be slightly different at higher flux densities. The B_x-B_y patterns also showed minor discrepancies. The difference between the field solutions obtained with the two

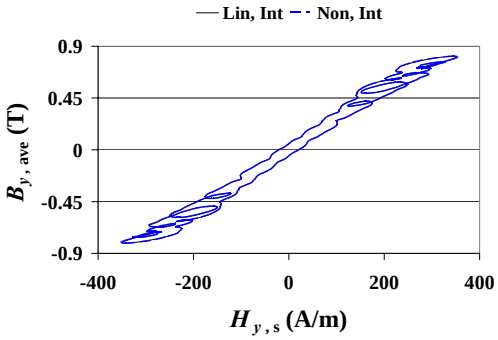

Figure 3.38 ***B-H*** *loop in stator at point A at a voltage of 400 V. 1-D model discretized with first-order elements.*

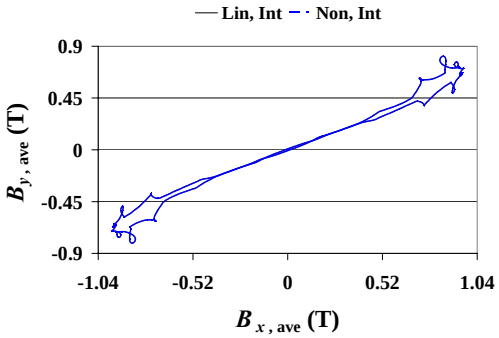

Figure 3.39 B_x-B_y *loop in stator at point A at a voltage of 400 V. 1-D model discretized with first-order elements.*

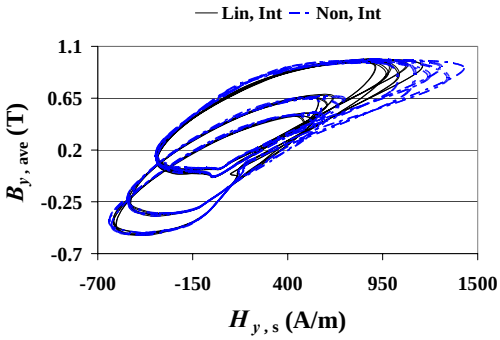

Figure 3.40 ***B-H*** *loop in rotor at point B at a voltage of 400 V. 1-D model discretized with first-order elements.*

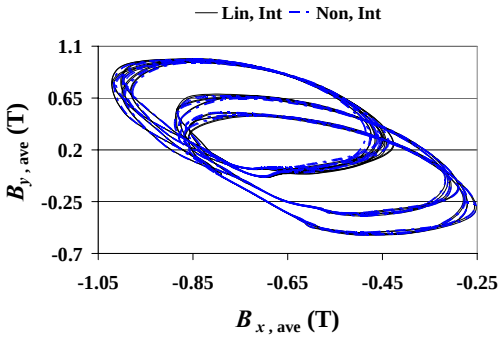

Figure 3.41 B_x-B_y *loop in rotor at point B at a voltage of 400 V. 1-D model discretized with first-order elements.*

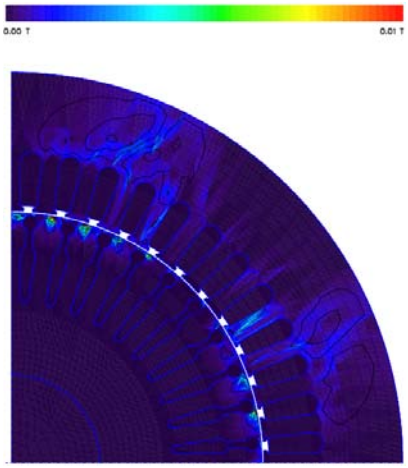

Figure 3.42 Difference of the field solutions from the linear and non-linear eddy current models. Magnetic flux density shading.

implementations of the eddy current model of the sheets at the time instant 200 ms is illustrated in Figure 3.42. According to the results in Figure 3.42 the rotor slot closings and stator teeth are the parts most affected by the non-linear eddy current modeling. However, for the problem being studied the differences are insignificant; the maximum value of the magnetic flux density in Figure 3.42 is 0.01 T.

Stator current

Comparisons of the computed and measured stator phase currents are presented in

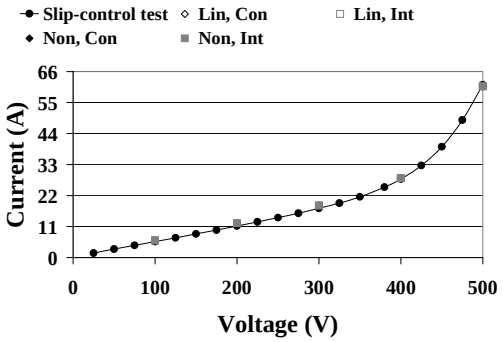

Figure 3.43 Current with six first-order 1-D elements. Conventional (Con), integration (Int), linear (Lin) and non-linear (Non).

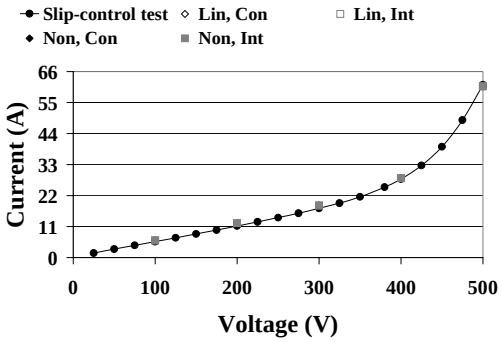

Figure 3.44 Current with two third-order 1-D elements.

Figures 3.43 and 3.44. The computed currents agree well with the measured ones with both the orders of the 1-D elements. In addition, the effect of the coupling or implementation of the 1-D model on the results is minor. The average relative difference between the simulations and experiments is 4.6% for both the orders of the 1-D elements.

Power balance

A study of the errors in the power balance reveals the importance of choosing the 1-D elements in accordance with the coupling approach. The errors in the power balance from the first-order 1-D elements are depicted in Figure 3.45, whereas Figure 3.46 shows similar results for the third-order 1-D elements. Clearly, as was observed in the investigations of the model *example geometry 1*, the first-order 1-D elements in connection with the *conventional* coupling technique do not represent the eddy currents with sufficient accuracy. The error in the power balance is as much as −17% at 100 V. As the voltage increases, the accuracy of the coupling is improved. This is related to the increase in the portion of the total losses of the stator-winding DC resistive losses. As opposed to the *conventional* approach, the *integration* approach provides a reliable coupling even with the first-order 1-D elements. The errors in the power balance range from −1.55% to −0.83%.

When the third-order 1-D elements are employed, both the coupling approaches perform well enough. The *integration* technique improves fairly well, the errors in the power balance being between −0.95% and −0.12%. For the *conventional* technique the enhancement is much more notable. For instance, at 100 V, the error in the power balance changes from −17% to −0.6%, depending slightly on the implementation of the eddy current model.

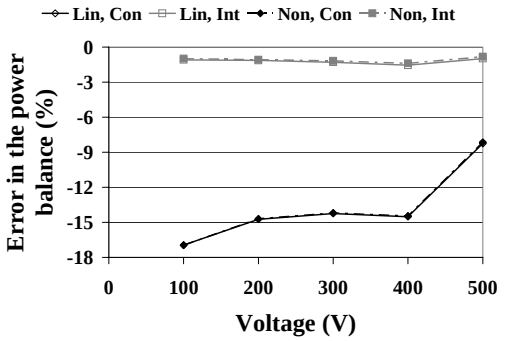

Figure 3.45 Errors in the power balance with six first-order 1-D elements. Conventional (Con), integration (Int), linear (Lin) and non-linear (Non).

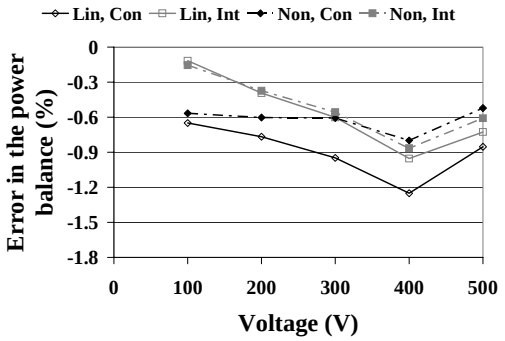

Figure 3.46 Errors in the power balance with two third-order 1-D elements.

According to the errors obtained in the power balance, linearizing the 1-D eddy current problem does not lead to a great loss of accuracy. With the first-order 1-D elements, the linear and non-linear implementations of the 1-D model yield similar results in the case of both the coupling methods. When the third-order elements are applied the discrepancies between the two implementations are somewhat greater but not remarkable.

Computational efficiency

The computer employed was equipped with a 2.66-GHz processor and 1.95 GB of RAM. Comparisons of the computation times of the slip-control tests are shown in Tables XVI and XVII. The tabulated figures were obtained with a rated voltage of 400 V. It is observed that the utilization of the third-order 1-D elements results in slightly higher computation times in most cases. With the *integration* coupling and linear implementation of the 1-D model, for instance, the computation time of one period of line voltage is 6% greater for the third- than for the first-order 1-D elements. It is worth noting that the number of nodes in the 1-D mesh was constant throughout the study.

Modeling the true magnetic properties of electrical steel sheets is computationally expensive. The increase in the computation time of a period of line voltage is, on average, 81% when the non-linear eddy current model is employed instead of the linear one.

Table XVI Computation times with an input voltage of 400 V utilizing six first-order 1-D elements.

Method of coupling	Lin, Con	Non, Con	Lin, Int	Non, Int
CPU time per period of line voltage (s)	3467	4914	3048	5774
Average CPU time for constructing a 2-D system matrix (s)	0.0597	0.0945	0.0509	0.1093
Average number of iterations per period of line voltage	106	106	106	106

Table XVII Computation times with an input voltage of 400 V utilizing two third-order 1-D elements.

Method of coupling	Lin, Con	Non, Con	Lin, Int	Non, Int
CPU time per period of line voltage (s)	3605	8067	3246	5528
Average CPU time for constructing a 2-D system matrix (s)	0.0614	0.1026	0.0559	0.1064
Average number of iterations per period of line voltage	106	164	106	106

Combining the *conventional* technique and third-order 1-D elements with the non-linear implementation of the 1-D model is particularly inefficient. This inefficiency is due to the convergence problems faced. Overcoming these requires a smaller value for χ, 0.1, than in other computations.

Conclusion

The most important findings of the above no-load simulations of the 37-kW test motor can be summarized as follows.

- The conclusions drawn from the analyses of the simple example geometry were found also to hold true for a rotating electrical machine. Both the *conventional* and *integration* techniques couple the lamination eddy currents to the 2-D model accurately enough if the order of the 1-D elements is suitably selected. Importantly, the linearized approach is also valid for complicated apparatuses such as electrical machines, provided the ratio of the sheet thickness to the skin depth is low enough.

- The order of the 1-D elements does not affect the losses heavily. However, the utilization of the first-order 1-D elements is preferable from the computational efficiency point of view.

- The measured total electromagnetic losses and their separate components match well with the corresponding computed ones. The computed currents are in good correspondence with the measured ones.

- On the basis of the study, it is proposed that the *integration* method, together with the first-order 1-D elements, should be used for the coupling. Such a combination provides an adequate power balance with the lowest computational cost in comparison with the other approaches. In addition, whenever justified, the 1-D eddy current modeling should be dealt with in a linearized manner.

3.2.3 No-load and full-load operation with frequency-converter supply

This section aims to analyze the test motor and, particularly, its losses under a frequency-converter supply. First, the no-load operation is investigated and, especially, the effects of the switching frequency are elaborated. Both the time-discretized and time-harmonic implementations of the method are used to compute the additional electromagnetic losses resulting from the higher harmonics and a comparison with the measurements is shown. Next, the simulations performed under loading are elaborated.

Those studies aim at investigating the change in the losses in comparison with the no-load condition. Last, the possibilities of employing the 1-D sheet model purely as a post-processing tool are discussed.

Problem setting

In order to model the high frequencies present in the frequency-converter supply, denser meshing and short time-steps were employed (Pippuri and Arkkio, 2009). The 2-D geometry was meshed with 3046 second-order elements with three integration points, while the 1-D mesh covering half of the lamination thickness consisted of 13 equally sized first-order elements. The 2-D mesh is shown in Figure 3.47 together with a close-up of a rotor bar. The measured output-voltage waveforms were used as inputs in the simulations. The main voltages at no load at a fundamental frequency of 50 Hz, the switching frequency being 3 kHz, are depicted in Figure 3.48. At the operating points for which the fundamental frequency was 7.5 or 22.5 Hz, the number of time-steps per period was 2000 and for the rest it was 1000. Altogether 10 periods of line voltage were computed. The 2-D and 1-D models were coupled in a linearized manner with the *integration* method and χ was 0.15.

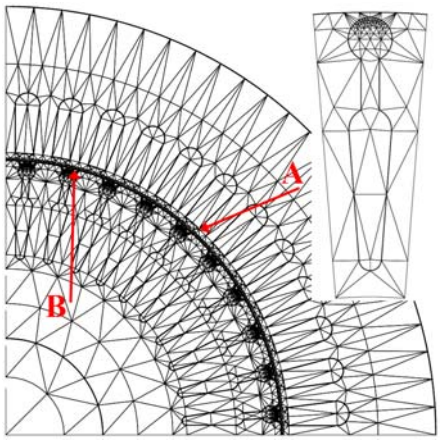

Figure 3.47 Finite element mesh and points A and B where the flux patterns are investigated more closely.

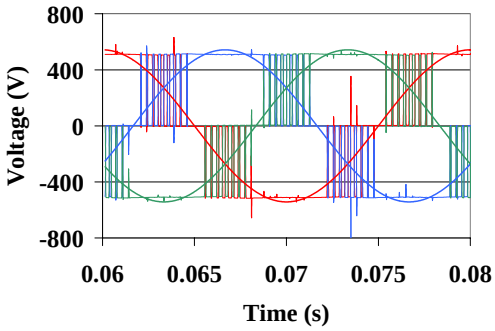

Figure 3.48 Main voltages and related fundamental components at no load at 50 Hz, switching frequency 3 kHz.

Standard no-load test

During a standard no-load experiment the machine is not running exactly at zero slip at synchronous speed. A slip at which the motor can produce the power that is consumed as friction losses was used in the simulations. The measured and computed total electromagnetic losses at different switching frequencies are compared in Figures 3.49–3.51. Clearly, the time-discretized method provides accurate enough results, especially

when the fundamental supply frequency is between 22.5 and 70 Hz. The greatest relative difference between the simulated and measured losses is 37% at 7.5 Hz, with the switching frequency being 6 kHz. However, on average the difference is significantly lower, about 9%. The stator currents are depicted in Figure 3.52. Figure 3.52 shows that in comparison with the measured ones, the computed stator currents are somewhat overestimated, on average by 8%. Particularly at 100 Hz, with a switching frequency of 1 kHz, the difference is significant, which, in part, causes the overestimation of the electromagnetic losses.

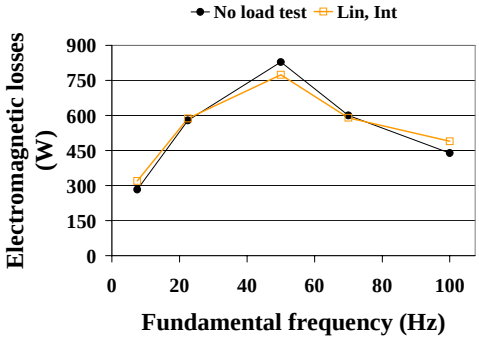

Figure 3.49 Electromagnetic losses as a function of fundamental frequency, at a switching frequency of 1 kHz.

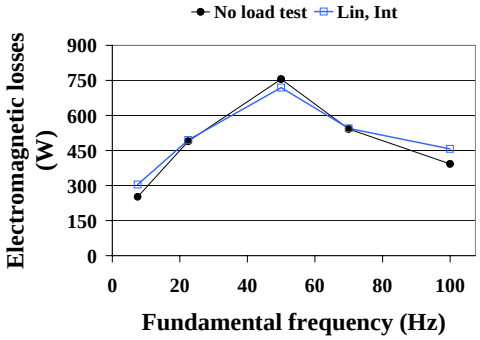

Figure 3.50 Electromagnetic losses as a function of fundamental frequency, at a switching frequency of 3 kHz.

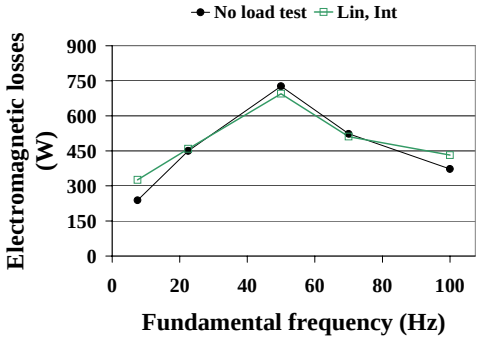

Figure 3.51 Electromagnetic losses as a function of fundamental frequency, at a switching frequency of 6 kHz.

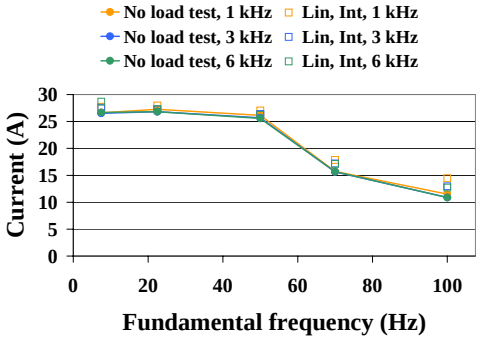

Figure 3.52 Stator current as a function of fundamental frequency.

The computed electromagnetic losses are collected in Figure 3.53 and compared. It can be seen from Figure 3.53 that the results are mainly in accordance with the theory, i.e., the losses in the motor decrease as the switching frequency of the supplying frequency converter increases. As can be seen from Figure 3.52 the deviation at 7.5 Hz, 6 kHz, is partly associated with the overestimated DC resistive losses of the stator winding. A closer look at the results revealed that the eddy current losses of the sheets and the rotor-cage losses are most notably affected by the switching frequency. The different loss

components at 50 Hz are shown in Figure 3.54. The core losses at the same operating point are separated for the stator and rotor parts in Figure 3.55. These are the rotor eddy current losses that are the most dependent on the switching frequency.

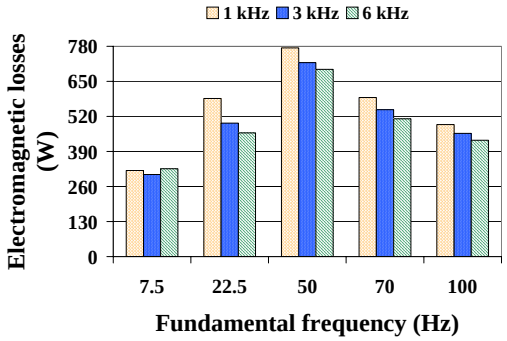

Figure 3.53 Computed electromagnetic losses as a function of fundamental frequency.

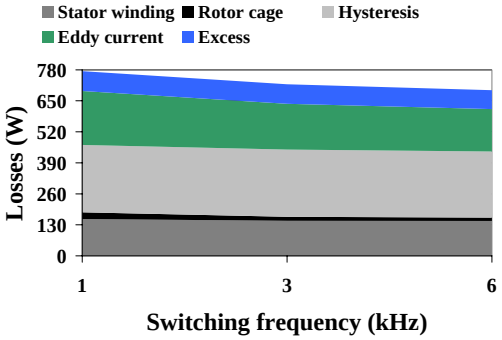

Figure 3.54 Computed electromagnetic losses at fundamental frequency 50 Hz as a function of switching frequency.

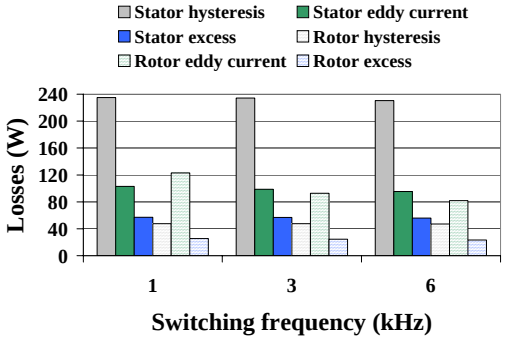

Figure 3.55 Computed iron losses at fundamental frequency 50 Hz as a function of switching frequency.

Additional losses caused by the frequency-converter supply

In order to study the additional losses caused by the harmonic content of the frequency-converter supply, the operating point for which the switching frequency is 3 kHz was also simulated under sinusoidal supply conditions. The input voltage was adjusted to accord with the fundamental component of the frequency-converter output-voltage waveform. In addition to the time-discretized analyses, the time-harmonic implementation of the coupled 2-D–1-D model was also employed in the investigation. Within the simulations that were performed, the number of harmonic components taken into account was 500. Such an amount provided a sufficient coverage of the measured wave-

forms. The same space-discretization as in the time-discretized computations was utilized.

The additional electromagnetic losses obtained with both the computational methods and experiments with a switching frequency of 3 kHz are shown in Figure 3.56. It is observed that the results from the time-discretized simulations mostly agree well with the experiments. The greatest difference occurs at a fundamental frequency of 7.5 Hz. The time-harmonic model is able to predict the trend of the additional losses measured with reasonable accuracy. The differences in the quantities of the results are largely explainable by the neglect of the excess losses. On the other hand, omitting the phase shifts and considering solely the amplitudes of the voltage components in the construction of the supply conditions of a simulation is not expected to cause great errors. According to previous research (Repo and Arkkio, 2006), the phase shifts of the harmonics or disturbances are important only if their frequencies are low compared to the fundamental frequency, for instance below 200 Hz with a fundamental of 50 Hz. In the operating points studied, only very few of all the harmonics (0.8%) fell into that category.

The main motivation for applying a method as rough as the time-harmonic one presented here is its computational efficiency. While the total computation time of one operating point in Figure 3.56 with the time-discretized method is 90 hours, the time-harmonic one solves the same problem in approximately 15 minutes. The rather long computation times of the time-discretized simulations originate from the following reasons: (i) in order to obtain one operation point, two simulations, one with frequency-converter supply and another with sinusoidal supply, need to performed, (ii) during both the aforementioned simulations, 10 periods of line voltage are completed, and (iii) rather fine space- and time-discretizations are employed for capturing the high-frequency phenomena with a sufficient accuracy.

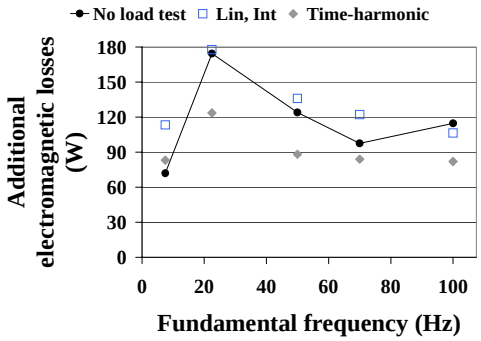

Figure 3.56 Additional electromagnetic losses resulting from the frequency-converter supply with a switching frequency of 3 kHz.

The increases in the different loss components according to the time-discretized analyses are illustrated in Figures 3.57 and 3.58. Figure 3.57 shows the difference of the loss components evaluated by subtracting the results with a sinusoidal supply from those with a frequency-converter supply. In Figure 3.58, the increase in the iron-loss components obtained in a similar manner is elaborated. Up to the operating point of 50 Hz, the absolute change in the hysteresis losses is the greatest. At 70 and 100 Hz the eddy current losses dominate. A closer look at the changes in the iron-loss components reveals that except at the operating point of 50 Hz, the eddy current losses of the rotor are the losses that are most affected by the higher harmonics of the frequency converter. On the stator side, the difference in the eddy current losses is small. On the other hand, the increase in the hysteresis losses of the stator is rather significant.

The flux patterns of the test motor with a sinusoidal voltage waveform and

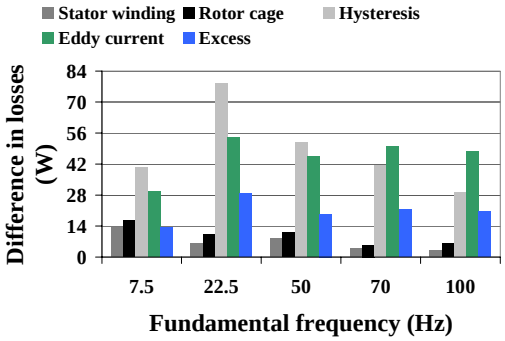

Figure 3.57 Increase in loss components resulting from the frequency-converter supply with a switching frequency of 3 kHz. Time-discretized analysis.

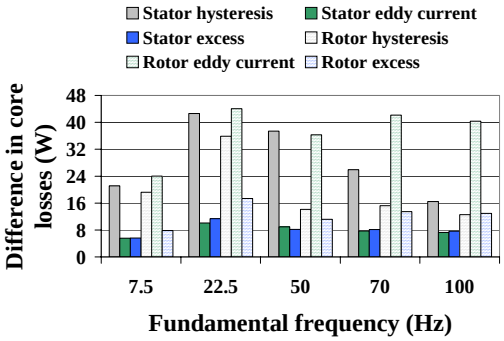

Figure 3.58 Increase in iron-loss components resulting from the frequency-converter supply with a switching frequency of 3 kHz. Time-discretized analysis.

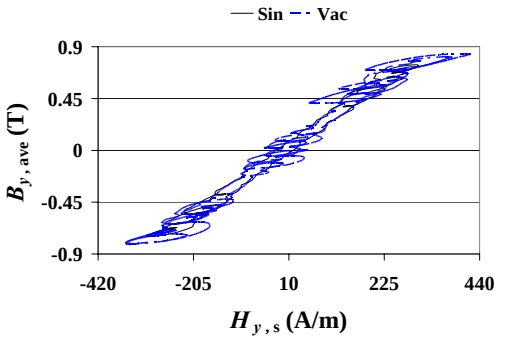

*Figure 3.59 **B**-**H** loop in stator at point A at a fundamental frequency of 50 Hz. Sin sinusoidal supply, Vac frequency-converter supply.*

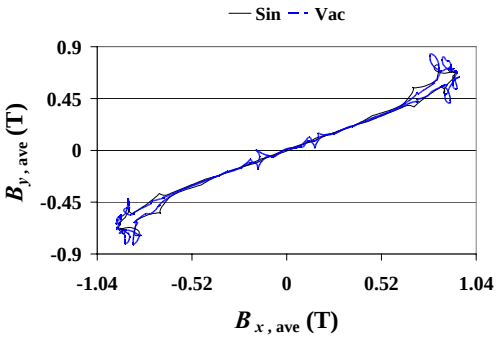

Figure 3.60 B_x-B_y loop in stator at point A at a fundamental frequency of 50 Hz. Sin sinusoidal supply, Vac frequency-converter supply.

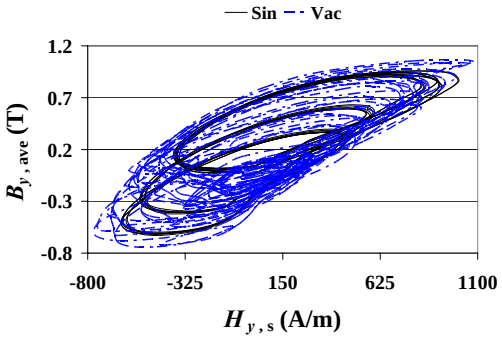

Figure 3.61 ***B*-*H*** *loop in rotor at point B at a fundamental frequency of 50 Hz. Sin sinusoidal supply, Vac frequency-converter supply.*

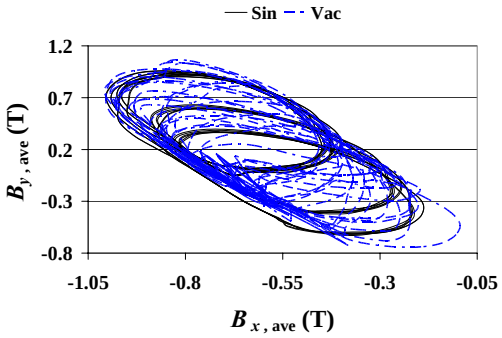

Figure 3.62 B_x-B_y *loop in rotor at point B at a fundamental frequency of 50 Hz. Sin sinusoidal supply, Vac frequency-converter supply.*

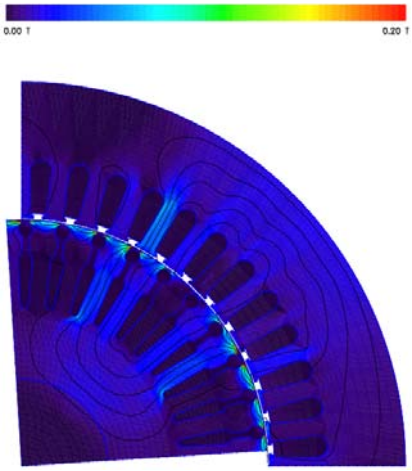

Figure 3.63 High-frequency magnetic flux density associated with the frequency-converter supply at a fundamental frequency of 50 Hz.

frequency-converter supply are compared in Figures 3.59–3.62. The ***B*-*H*** loop and B_x-B_y patters in the stator tooth tip at point A are shown in Figures 3.59 and 3.60 as Figures 3.61 and 3.62 are from the rotor slot closure at point B. The computation results that are used are from the 50-Hz operating points. The rotor-side loop patterns are particularly altered by the higher harmonics. A field solution obtained by subtracting the sinusoidal supply result from the frequency-converter one at a time instant 200.4 ms is given in Figure 3.63. Clearly, the magnetic field density in the rotor parts close to the air gap is changed the most.

Standard full-load test

The full-load operation of the 37-kW test motor was simulated using the output-voltage waveforms recorded at the switching frequency 3 kHz. The slip was set to a value with which the motor produces an electromagnetic torque that corresponds to the sum of the measured shaft torque and the torque resulting from the friction losses. The increase in the total electromagnetic losses from the loading is shown in Figure 3.64. The differences in the loss components obtained by subtracting the results at no load from those at full load are depicted in Figure 3.65. As can be seen from Figure 3.64, the total electromagnetic losses change substantially under the loading. At the fundamental frequency of 100 Hz these are almost nine times as large as at no load. The major increase is mainly due to the loading currents, which result in considerable losses in the windings of the machine, as shown in Figure 3.65. Of those in the core, the eddy current losses are the most altered. At the operating points 7.5 and 22.5 Hz, the core losses are slightly greater at no load than at full load. The reason for this is the drop in the flux level in the motor as a result of the loading.

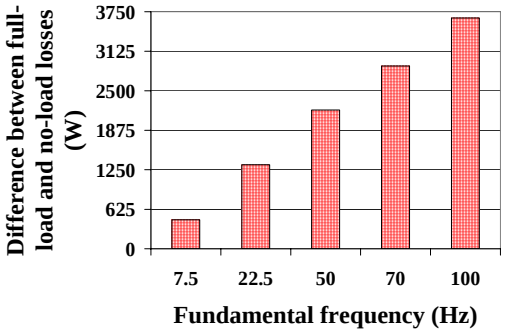

Figure 3.64 Increase in the total electromagnetic losses caused by the loading.

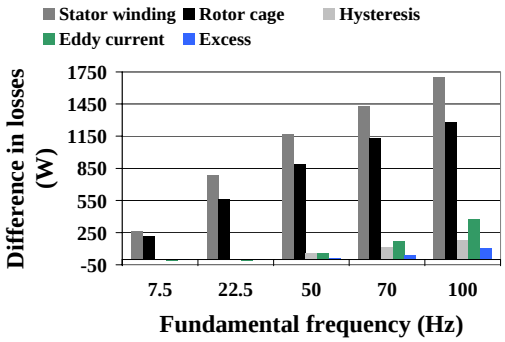

Figure 3.65 Losses at no load subtracted from those at full load. Different loss components.

Utilization of the eddy current model of the sheets for post-processing

The full-load operation of the test motor was also investigated by omitting the eddy currents in the sheets from the field solution and instead utilizing the 1-D model purely for the post-processing of the related losses. The results of the comparative study carried out with the 3-kHz output-voltage waveforms are illustrated in Figures 3.66–3.70. The total measured and simulated electromagnetic losses are shown in Figure 3.66. The correspondence between these is good, the relative difference being 7.7% on average for the complete approach with the eddy currents of the sheets included in the field solution and 8.3% for the a posteriori analysis. The differences in the separate loss components between the two computation models are illustrated in Figure 3.67. It was found that the

coupled model produces larger winding losses than the a posteriori one, while for the core losses the opposite is true. When the eddy currents in the sheets are included in the analysis, they damp the field, resulting in smaller core losses. In the frame of the total electromagnetic losses, however, the discrepancies seem to be rather insignificant.

Besides the electromagnetic losses, the stator currents, electromagnetic torque, and input power were also examined. As Figure 3.68 shows, the simulated stator currents are in satisfactory agreement with the measured ones. The coupled model produces estimates that are, on average, 3.5% too large, while for the a posteriori technique the corresponding figure is 2.8%. The computation of the input power can be slightly enhanced by including the eddy currents of the sheets in the field analysis. The relative difference between the coupled model and measurements is 1.3% on average. The application of the 1-D model merely as post-processing yields an average relative difference of 2%. The values of the electromagnetic torque evaluated from the measurements and

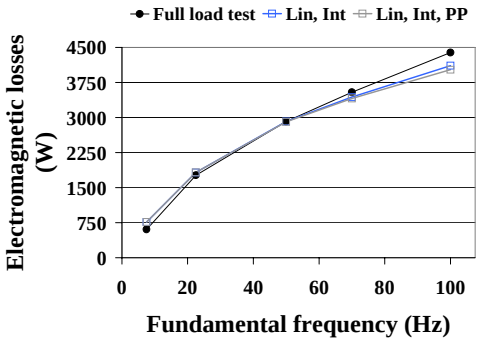

Figure 3.66 Electromagnetic losses as a function of fundamental frequency; PP denotes post-processing.

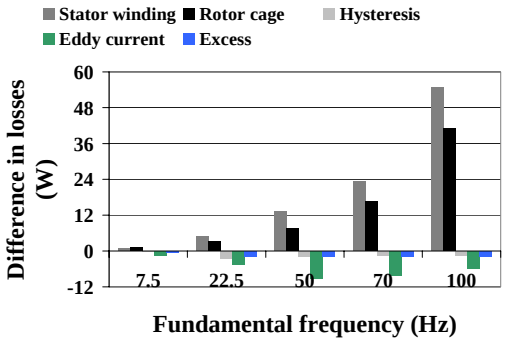

Figure 3.67 Loss differences. Results of post-processing subtracted from those of the coupled model.

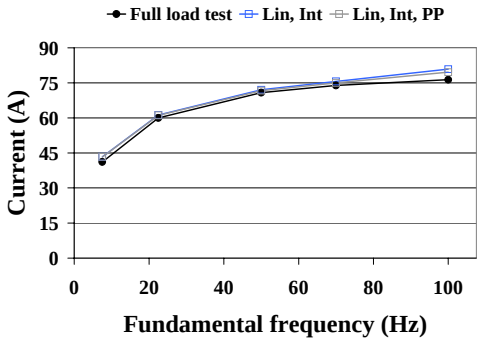

Figure 3.68 Stator current as a function of fundamental frequency; PP denotes post-processing.

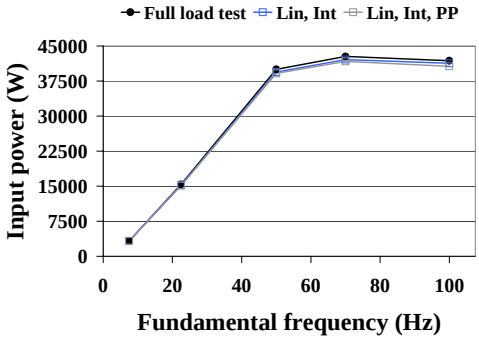

Figure 3.69 Input power as a function of fundamental frequency; PP denotes post-processing.

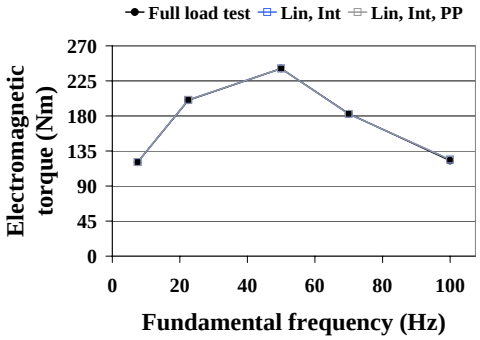

Figure 3.70 Electromagnetic torque as a function of fundamental frequency; PP denotes post-processing.

obtained by simulations are shown in Figure 3.70. Clearly, the correspondence between the results is good and there is practically no difference between the two computation approaches.

Conclusion

The most important results of the analysis of the test motor under the frequency-converter supply are given below.

- Time-discretized analyses of the no-load operation of the test motor were carried out employing three different input voltages with switching frequencies 1 kHz, 3 kHz, and 6 kHz. The computed total electromagnetic losses were in satisfactory agreement with the measurements; the average relative difference was 9%.

- The additional electromagnetic losses caused by the harmonic content of a frequency-converter supply were examined by both the time-harmonic and time-discretized implementation of the coupled method. The correspondence between the simulations and experiments was found to be reasonable. In the case of the time-discretized model the relative difference was 20% on average, while for the time-harmonic one the corresponding figure was 23%. The value presented for the time-discretized method would be notably better if the 7.5 Hz point was not taken into consideration. The eddy current losses of the rotor were revealed to be the losses that were most influenced by the higher harmonics. However, the total hysteresis losses rose notably, too.

- The performance of the test motor was also investigated under loading. The increase in the electromagnetic losses in comparison with no load is substantial and is mainly caused by the winding losses. The eddy current losses are the most

altered of the core-loss components. The simulated full-load losses agreed well with the experimental ones.

- Last, the possibility of applying the 1-D model solely for the loss computation was considered. According to the study, the total electromagnetic losses of the test machine could be estimated at full load almost as accurately as when the eddy currents of the sheets were included in the field solution. Furthermore, the simulated values of the electromagnetic torque were practically indistinguishable from those that were measured. Clearly, the eddy current phenomenon of the sheets is not dominant in the test motor, at least not at full load.

4 Discussion

4.1 Summary and significance of the work

In this thesis, the eddy current phenomenon in electrical steel sheets is carefully investigated. For this purpose two methods have been developed: a time-discretized and a time-harmonic one. Both the methods incorporate the eddy currents in the sheets into the 2-D finite element analysis of electrical machines through a 1-D penetration equation. The work especially concentrates on the applicability and proper implementation of such coupled methods and on the analysis of frequency-converter-fed electrical machines.

Let us first consider the time-discretized approach and the results obtained with it. The original idea of including the magneto-dynamic effects of steel sheets in a 2-D field formulation through a 1-D penetration equation was presented by Bottauscio et al. (2000a). This thesis contributes to the topic by studying the utilization of the 1-D field solution in 2-D equations in detail. The hysteresis and excess effects, however, are neglected and the magnetic properties covered by a single-valued magnetization curve. In principle, the two models are coupled by obliging the magnetic field strength in the 2-D analysis to correspond with the surface magnetic field strength of the sheets from the 1-D modeling. For determining the surface magnetic field strength, i.e., $\boldsymbol{h}(-d,t)$, two approaches are proposed, the *conventional* and *integration* techniques.

In the *conventional* technique, the magnetic field strength is solved traditionally as a product of the magnetic flux density and reluctivity, while the *integration* one is based on Ampère's circuital law. Analyses of simple example geometries and of an electrical machine show that the space-discretization of the 1-D geometry greatly affects the reliability of the coupling in certain cases. In particular, associating the first-order 1-D elements with the *conventional* technique is inappropriate. By doing this the eddy current losses represented by the 1-D field solution become only partly included in the 2-D equations. This is seen in the power balance of the method if the eddy current density is used to evaluate the related losses. On the other hand, if the eddy current losses are integrated from the ***B*-*H*** loops, the values obtained are considerably underestimated. On the contrary, the *integration* approach also performs well in terms of the power balance with the first-order 1-D elements. This can be justified by the fact that the approach solves the magnetic field strength on the surface from the eddy current distribution. The aspects concerning the accuracy of the inclusion of the eddy currents in the 2-D analysis and its effects on the different electromagnetic quantities have only rarely been addressed in the literature (Dupré et al., 1999), (Dlala, 2009a). Within this thesis, the coupling of the 1-D and 2-D formulations is investigated in a systematic and thorough manner, with the space-discretization being considered carefully. Thus it contributes by providing new information on the suitable use of methods such as the one in question.

In addition to the success of the inclusion of the eddy current effects in the 2-D finite element analysis, the computational cost at which it is achieved is of great importance. The computations that were carried out revealed that even if the number of nodes in the 1-D mesh is kept constant, changing the order of the elements might result in a notable increase in the computation time. Basically, the higher the order, the longer the computation time is. The magnetic linearization of the 1-D model was also studied in order to gain better computational efficiency. When the non-linear magnetic properties of the steel sheets are being considered, the computational algorithm of the 2-D–1-D approach that was developed copes with two nested iterative schemes. Obviously, it would be beneficial to avoid that. It was discovered that the iterative solution of the 1-D equations can be omitted and instead the reluctivity taken as an input from the 2-D computation scheme if the ratio of the sheet thickness to the skin depth is approximately below five. Within these limits, the linearized 1-D implementation provides results comparable to those obtained with the non-linear one, not only in respect of the losses but in respect of other electromagnetic quantities as well.

On the basis of the observations above, from the viewpoint of both accuracy and computational efficiency, the *integration* method together with the first-order 1-D elements couples the 2-D and 1-D models in an optimal way. In addition, the complexity of the computational scheme should be reduced, whenever practicable, by magnetically linearizing the 1-D eddy current problem. The idea of the linearization of the 1-D equations within the coupled approach and its implementation are original.

The time-discretized 2-D–1-D method was used to compute a 37-kW test induction motor under different supply and loading conditions. First, the no-load operation with a sinusoidal voltage supply was simulated. The slip-control measurements performed verify the simulation results obtained; the relative difference between the computed and experimental electromagnetic losses is 8% on average. For the stator currents, the corresponding figure is 5%. Second, the operation of the test motor with a frequency-converter supply was analyzed. At no load, computations in which the switching frequency of the frequency converter was varied were carried out. The electromagnetic losses obtained agree reasonably well with the measurements, the relative difference being 9% on average.

The biggest differences between the simulations and experiments occur at the operating points with the lowest and highest fundamental frequencies. This is partly due to the overestimation of the stator currents by the method. One of the findings of the no-load simulations is that the eddy current losses of the sheets are the core-loss component which is most affected by the switching frequency. In the rotor, these losses decrease by 36% on average when the switching frequency is raised from 1 kHz to 6 kHz. The additional losses caused by the higher harmonics of the frequency-converter supply were also studied. Of the core-loss components, the rotor eddy current losses of the sheets change the most in comparison with the case of the sinusoidal voltage supply. Besides the no-load condition, loaded operating points of the test motor were investigated. The method was found to provide reasonable estimates of the electromagnetic losses at load-

ing, too. The simulated values differ from the measured ones by 8% on average. Last, the application of the 1-D eddy current model merely for the loss computation without its inclusion in the 2-D equations was analyzed. According to the examination, the simulated losses and input powers agree slightly better with those from the measurements when the eddy current phenomena in the sheets are actually taken into account. However, the increase in the accuracy is low in comparison with its computational cost.

By neglecting the eddy currents from the field solution, the computation time can be reduced by 93% on average. Thus, it appears that in applications such as the test machine in question it may be more beneficial to omit the eddy currents in the sheets from the 2-D analysis and simply post-process the related losses by the 1-D model. In particular, in this thesis, the test machine was investigated with a frequency-converter supply in a manner which comprehensively models the eddy currents in the sheets. To conclude, the various simulations conducted on the 37-kW test motor clarify the usability of the time-discretized method that was developed. The correspondence between the computed and measured losses and other electromagnetic quantities is satisfactory.

The time-harmonic method that was developed is, owing to its implementation, applicable for analyzing problems for which supply conditions might be non-sinusoidal. Like the time-discretized one, it was used to model the 37-kW test machine. The additional electromagnetic losses at no load as a result of the frequency-converter supply were computed. The results that were obtained agree with the measurements with reasonable accuracy. The most significant single factor explaining the differences between the simulations and measurements is the neglect of the excess losses. Because of its superior computational efficiency, the time-harmonic approach that was proposed is seen to hold opportunities for qualitative analysis.

4.2 Shortcomings and further research

Although the 2-D–1-D models that were presented were able to predict the losses and other electromagnetic quantities of the test motor under various operating conditions with reasonable accuracy, they also involve some shortcomings. These are discussed next. In addition, this section points out some topics and themes for further research.

Perhaps the most obvious shortcoming of the time-discretized method is the neglect of the hysteresis and excess effects. Their inclusion in the analysis would require, particularly in the case of rotating electrical machines, either utilization of more powerful methodologies for coping with the non-linearities, e.g. the fixed point method (Dlala, 2008b), or derivation of the equations of the sheets in a mesh-free frame (Rasilo and Arkkio, 2010). As pointed out above, however, the consideration of all the magnetodynamic effects of the sheets was beyond the scope of this thesis.

In principle, the separation of the truly interdependent phenomena of the sheets is a rather substantial simplification. According to the literature review, however, in an apparatus with an air gap, such as an electrical machine, it is mostly expected to cause the contributions of the iron-loss components to be somewhat inaccurate. For instance, Dlala et al. (2010) analyzed a test induction motor by post-processing its losses with a comprehensive sheet formulation, i.e., solving the 1-D penetration equations encompassing dynamic hysteresis modeling. Their study revealed that the total amount of the iron losses does not change greatly, regardless of whether or not the eddy current and hysteresis phenomena are interdependently taken into account. If they are, the total losses are 577 W, while, if not, the corresponding figure is 567 W. The contributions of the iron-loss components, on the other hand, are quite notably affected since, for instance, the eddy current losses computed with a single-valued magnetization curve are 21% greater than those obtained with the hysteresis included. Thus, the methods developed within this thesis are expected to produce somewhat overestimated values of the eddy current losses of the sheets. Regarding the modeling of the sheets, it must also be noted that both the coupled methods presented in this thesis omit the rotating components of the hysteresis and the time-discretized method the rotating components of the excess losses, too. This naturally partly explains the differences between the simulations and measurements. The iron-loss computation of the time-discretized approach could be enhanced by fitting the hysteresis and excess-loss coefficients from 2-D measuring data. The same also applies to the hysteresis modeling of the time-harmonic method. Another future topic is the inclusion of the excess effects in the time-harmonic method.

Other shortcomings of the methods concerning the modeling of the fields and windings are the neglect of the losses in the frame of the machines and the exclusion of the eddy currents in the conductors of the stator windings. Both of these simplifications, however, are typically justified for machines like the one studied in this work. Including the eddy currents of the phase windings in the field analysis becomes necessary with machines equipped with form-wound windings (Islam, 2010). In addition, the reduction of the intrinsically 3-D problem to a coupled 2-D–1-D one in the first place introduces sources of inaccuracy. The end fields of rotating electrical machines tend to be strongly 3-D, implying that the losses and their distribution in a real machine are different from the assumed ones. Finally, electrical steel sheets always exhibit anisotropy to some extent, the consideration of which has been beyond the scope of the research (Tumanski, 2003).

Finally, within this thesis, the non-linearities of the problems were handled by an incomplete Newton-Raphson method, possibly in association with under-relaxation. Although such means ensure sufficient convergence properties, they might not be the most efficient ones. An attractive topic for future research is the enhancement of the computation times, particularly of the time-discretized method. Interesting works on the improvement of the Newton-Raphson iterative scheme have been produced, for instance by Bastos et al. (1995) and Fujiwara et al. (2005). The findings of these might be applicable to speed up the convergence of the time-discretized simulations.

5 Conclusion

This work aimed at developing methods that comprehensively model the eddy currents in electrical steel sheets and the losses inflicted by these. The second objective was to employ such methods in the analysis of frequency-converter-fed rotating electrical machines under practical working conditions. To meet these objectives, two methods were developed, one of which is founded on the assumption of the sinusoidal time variation of the electromagnetic quantities, whereas the other is suitable for studying the actual time variation. In order to test their applicability, a 37-kW cage-induction motor was examined under different operating conditions by means of experiments and simulations and the results were compared.

Both the computational methods that were developed are based on the finite element solution of the two-dimensional (2-D) field and winding equations of electrical machines. The eddy currents flowing in the sheets are modeled by a one-dimensional (1-D) diffusion equation and incorporated into the 2-D formulations. The time-discretized method couples the 1-D solution through the surface magnetic field of the sheets, while the time-harmonic model employs the complex reluctivity.

This work contributes to the methodology of coupled, time-discretized 2-D–1-D models by carefully analyzing how the 1-D solution is properly utilized in the 2-D formulation. Two means for the coupling of the models, i.e., for defining the surface magnetic field, were presented and investigated. The results revealed that relatively great errors might occur in the input powers, losses, or power balance of the method if the inclusion of the eddy currents is realized improperly. The study resulted in a proposal for the optimal coupling. Second, the linearization of the 1-D model within the coupled method was analyzed. It was found that the modeling of the true magnetic properties of the sheets, i.e., here representing the magnetic properties of the sheets with a single-valued reluctivity curve, is not necessary if the ratio of the sheet thickness to the skin depth is below five. The time-harmonic version of the coupled model encompasses the eddy current but also the hysteresis of the sheets through a complex reluctivity. One of its innovations concerns the implementation; the method can be applied to compute a machine fed from a non-sinusoidal voltage source.

The methods proposed were applied to the test machine under different supply and loading conditions. The time-discretized approach provided sufficiently accurate estimates of the electromagnetic losses throughout the study, the errors being below 10%. In addition, it was found that out of the iron-loss components, the eddy current losses of the rotor are the most sensitive to the switching frequency of the frequency converter. These losses were also observed to increase the most in comparison with the sinusoidal supply. The hysteresis losses of the stator, however, changed remarkably, too. Partly because of its neglect of excess losses, the time-harmonic implementation of the method resulted in somewhat rough results. However, it modeled the trends of the additional

losses accurately enough with high computational efficiency. Its utilization for problems for which the definite quantity of the losses is not a key issue but the relative changes are could thus be proper. To conclude, the comparative investigations of the measurements and simulations emphasized the suitability of the methods developed for coping with the real operating conditions and properties of rotating electrical machines.

References

Ali, K., Atallah, K., and Howe, D. 1997. Prediction of mechanical stress effects on the iron loss in electrical machines. *Journal of Applied Physics*, vol. 81, no. 8, pp. 4119–4121.

Appino, C., Bertotti, G., Bottauscio, O., Fiorillo, F., Tiberto, P., Binesti, D., Ducreux, J. P., Chiampi, M., and Repetto, M. 1996. Power losses in thick steel laminations with hysteresis. *Journal of Applied Physics*, vol. 79, no. 8, pp. 4575–4577.

Arkkio, A. 1987. Analysis of Induction Motors Based on the Numerical Solution of the Magnetic Field and Circuit Equations. Acta Polytechnica Scandinavica, Electrical Engineering Series, no. 59, 97 p., available online:
http://lib.tkk.fi/Diss/198X/isbn951226076X/

Arkkio, A., Niemenmaa, A., and Saitz, J. 1998. Hysteresis torque in a cage induction motor. *Proceedings of the International Conference on Electrical Machines*, Istanbul, Turkey, vol. 3, pp. 1494–1499.

Atallah, K., Zhu, Z. Q., and Howe, D. 1992. An improved method for predicting iron losses in brushless permanent magnet DC drives. *IEEE Transactions on Magnetics*, vol. 28, no. 5, pp. 2997–2998.

Barbisio, E., Fiorillo, F., and Ragusa, C. 2004. Predicting loss in magnetic steels under arbitrary induction waveform and with minor hysteresis loops. *IEEE Transactions on Magnetics*, vol. 40, no. 4, pp. 1810–1819.

Basso, V., Bertotti, G., Bottauscio, O., Fiorillo, F., Pasquale, M., Chiampi, M., and Repetto, M. 1997. Power losses in magnetic laminations with hysteresis: Finite element modeling and experimental validation. *Journal of Applied Physics*, vol. 81, no. 8, pp. 5606–5608.

Bastos, J. P. A., Ida, N., and Mesquita, R. C. 1995. A variable local relaxation technique in nonlinear problems. *IEEE Transactions on Magnetics*, vol. 31, no. 3, pp. 1733–1736.

Belahcen, A. and Arkkio, A. 2008. Comprehensive Dynamic Loss-Model of Electrical Steel Applied to FE Simulation of Electrical Machines. *IEEE Transactions on Magnetics*, vol. 44, no. 6, pp. 886–889.

Belahcen, A. and Arkkio, A. 2010. Computation of additional losses due to rotor eccentricity in electrical machines. *IET Electric Power Applications*, vol. 4, no. 4, pp. 259–266.

Belahcen, A., Dlala, E., and Pippuri, J. 2010. Modelling eddy currents in laminated nonlinear magnetic circuits. Presented at the *Symposium on Electromagnetic Phenomena in Nonlinear Circuits (EPNC)*, Dortmund and Essen, Germany.

Bergqvist, A. 1994. On magnetic hysteresis modeling. Ph.D. thesis, Royal Institute of Technology, Stockholm, Sweden, 209 p.

Bertotti, G. 1988. General properties of power losses in soft ferromagnetic materials. *IEEE Transactions on Magnetics*, vol. 24, no. 1, pp. 621–630.

Bertotti, G. 1991. Generalized Preisach model for the description of the hysteresis and eddy current effects in metallic ferromagnetic materials. *Journal of Applied Physics*, vol. 69, no. 8, pp. 4608–4610.

Bertotti, G. 1992. Dynamic generalization of the scalar Preisach model of hysteresis. *IEEE Transactions on Magnetics*, vol. 28, no. 5, pp. 2599–2601.

Bertotti, G. and Pasquale, M. 1992. Physical interpretation of induction and frequency dependence of power losses in soft magnetic materials. *IEEE Transactions on Magnetics*, vol. 28, no. 5, pp. 2787–2789.

Bertotti, G., Boglietti, A., Chiampi, M., Chiarabaglio, D., Fiorillo, F., and Lazzari, M. 1991. An improved estimation of iron losses in rotating electrical machines. *IEEE Transactions on Magnetics*, vol. 27, no. 6, pp. 5007–5009.

Bobbio, S., Miano, G., Serpico, C., and Visone, C. 1997. Models of magnetic hysteresis based on play and stop hysterons. *IEEE Transactions on Magnetics*, vol. 33, no. 6, pp. 4417–4426.

Boglietti, A., Bottauscio, O., Chiampi, M., Pastorelli, M., and Repetto, M. 1996. Computation and measurement of iron losses under PWM supply conditions. *IEEE Transactions on Magnetics*, vol. 32, no. 5, pp. 4302–4304.

Boglietti, A., Chiampi, M., Repetto, M., Bottauscio, O., and Chiarabaglio, D. 1998. Loss separation analysis in ferromagnetic sheets under PWM inverter supply. *IEEE Transactions on Magnetics*, vol. 34, no. 4, pp. 1240–1242.

Boglietti, A., Ferraris, P., Lazzari, M., and Profumo, F. 1991. Iron losses in magnetic materials with six-step and PWM inverter supply. *IEEE Transactions on Magnetics*, vol. 27, no. 6, pp. 5334–5336.

Bottauscio, O. and Chiampi, M. 2001. Laminated core modeling under rotational excitations including eddy currents and hysteresis. *Journal of Applied Physics*, vol. 89, no. 11, pp. 6728–6730.

Bottauscio, O. and Chiampi, M. 2002a. Analysis of laminated cores through a directly coupled 2-D/1-D electromagnetic field formulation. *IEEE Transactions on Magnetics*, vol. 38, no. 5, pp. 2358–2360.

Bottauscio, O., Canova, A., Chiampi, M., and Repetto, M. 2002b. Iron losses in electrical machines: influence of different material models. *IEEE Transactions on Magnetics*, vol. 38, no. 2, pp. 805–808.

Bottauscio, O., Canova, A., Chiampi, M., and Repetto, M. 2003. Rotational hysteresis and eddy current losses in electrical motor stators under non-conventional supply. *Journal of Magnetism and Magnetic Materials*, vols. 254–255, pp. 241–243.

Bottauscio, O., Chiampi, M., and Chiarabaglio, D. 2000a. Advanced model of laminated magnetic cores for two-dimensional field analysis. *IEEE Transactions on Magnetics*, vol. 36, no. 3, pp. 561–573.

Bottauscio, O., Chiampi, M., and Chiarabaglio, D. 2000b. Magnetic flux distribution and losses in narrow ferromagnetic strips. *Journal of Magnetism and Magnetic Materials*, vol. 215, pp. 46–48.

Cester, C., Kedous-Lebouc, A., and Cornut, B. 1997. Iron loss under practical working conditions of a PWM powered induction motor. *IEEE Transactions on Magnetics*, vol. 33, no. 5, pp. 3766–3768.

Chari, M. V. K. and Silvester, P. 1971. Finite-element analysis of magnetically saturated DC machines. *IEEE Transactions on Power Apparatus and Systems*, vol. 90, no. 5, pp. 2362–2372.

Chevalier, T., Kedous-Lebouc, A., and Cornut, B. 2000a. Influence of electrical sheet width on dynamic magnetic properties. *Journal of Magnetism and Magnetic Materials*, vols. 215–216, pp. 623–625.

Chevalier, T., Meunier, C., Kedous-Lebouc, A., and Cornut, B. 2000b. Numerical computation of the dynamic behavior of magnetic material considering magnetic diffusion and hysteresis. *IEEE Transactions on Magnetics*, vol. 36, no. 4, pp. 1218–1221.

Del Vecchio, R. D. 1980. An efficient procedure for modeling complex hysteresis processes in ferromagnetic materials. *IEEE Transactions on Magnetics*, vol. 16, no. 5, pp. 809–811.

Del Vecchio, R. M. 1982a. Computation of losses in nonoriented electrical steels from a classical viewpoint. *Journal of Applied Physics*, vol. 53, no. 11, pp. 8281–8286.

Del Vecchio, R. M. 1982b. The calculation of eddy current losses associated with rotating magnetic fields in thin laminations. *IEEE Transactions on Magnetics*, vol. 18, no. 6, pp. 1707–1709.

Dlala, E. 2008a. A Simplified Iron Loss Model for Laminated Magnetic Cores. *IEEE Transactions on Magnetics*, vol. 44, no. 11, pp. 3169–3172.

Dlala, E. 2008b. Magnetodynamic Vector Hysteresis Models for Steel Laminations of Rotating Electrical Machines. Ph.D. thesis, Helsinki University of Technology, Finland, 95 p., available online: http://lib.tkk.fi/Diss/2008/isbn9789512292776/

Dlala, E. 2009a. Comparison of Models for Estimating Magnetic Core Losses in Electrical Machines Using the Finite-Element Method. *IEEE Transactions on Magnetics*, vol. 45, no. 2, pt. 1, pp. 716–725.

Dlala, E. and Arkkio, A. 2009b. A General Model for Investigating the Effects of the Frequency Converter on the Magnetic Iron Losses of a Squirrel-Cage Induction Motor. *IEEE Transactions on Magnetics*, vol. 45, no. 9, pp. 3303–3315.

Dlala, E., Belahcen, A., and Arkkio, A. 2008c. Efficient magnetodynamic lamination model for two-dimensional field simulation of rotating electrical machines. *Journal of Magnetism and Magnetic Materials*, vol. 320, no. 20, pp. e1006–e1010.

Dlala, E., Belahcen, A., and Arkkio, A. 2008d. Magnetodynamic vector hysteresis model of ferromagnetic steel laminations. *Physica B: Condensed Matter*, vol. 403, nos. 2–3, pp. 428–432.

Dlala, E., Belahcen, A., Pippuri, J., and Arkkio, A. 2010. Interdependence of Hysteresis and Eddy-Current Losses in Laminated Magnetic Cores of Electrical Machines. *IEEE Transactions on Magnetics*, vol. 46, no. 2, pp. 306–309.

Domeki, H., Ishihara, Y., Kaido, C., Kawase, Y., Kitamura, S., Shimomura, T., Takahashi, N., Yamada, T., and Yamazaki, K. 2004. Investigation of benchmark model for estimating iron loss in rotating machine. *IEEE Transactions on Magnetics*, vol. 40, no. 2, pp. 794–797.

Dular, P., Gyselinck, J., Geuzaine, C., Sadowski, N., and Bastos, J. P. A. 2003. A 3-D magnetic vector potential formulation taking eddy currents in lamination stacks into account. *IEEE Transactions on Magnetics*, vol. 39, no. 3, pp. 1424–1427.

Dupré, L. R., Bottauscio, O., Chiampi, M., Repetto, M., and Melkebeek, J. A. A. 1999. Modeling of electromagnetic phenomena in soft magnetic materials under unidirectional time periodic flux excitations. *IEEE Transactions on Magnetics*, vol. 35, no. 5, pp. 4171–4184.

Dupré, L. R., Van Keer, R., and Melkebeek, J. A. A. 1996. On a magnetodynamic model for the iron losses in non-oriented steel laminations. *Journal of Physics D: Applied Physics*, vol. 29, no. 3, pp. 855–861.

Dupré, L. R., Van Keer, R., and Melkebeek, J. A. A. 1997a. Modelling and identification of iron losses in nonoriented steel laminations using Preisach theory. *IET Electric Power Applications*, vol. 144, no. 4, pp. 227–234.

Dupré, L. R., van Keer, R., and Melkebeek, J. A. A. 1997b. An iron loss model for electrical machines using the Preisach theory. *IEEE Transactions on Magnetics*, vol. 33, no. 5, pp. 4158–4160.

Dupré, L., De Wulf, M., Makaveev, D., Permiakov, V., Pulnikov, A., and Melkebeek, J. 2003. Modelling of electromagnetic losses in asynchronous machines. *COMPEL: The International Journal for Computation and Mathematics in Electrical and Electronic Engineering*, vol. 22, no. 4 pp. 1051–1065.

Dupré, L.R., Bottauscio, O., Chiampi, M., Fiorillo, F., Lo Bue, M., Melkebeek, J., Repetto, M., and Von Rauch, M. 1998. Dynamic Preisach modelling of ferromagnetic laminations under distorted flux excitations. *IEEE Transactions on Magnetics*, vol. 34, no. 4, pp. 1231–1233.

Fiorillo, F. and novikov, A. 1990. An improved approach to power losses in magnetic laminations under nonsinusoidal induction waveform. *IEEE Transactions on Magnetics*, vol. 26, no. 5, pp. 2904–2910.

Fujiwara, K., Okamoto, Y., Kameari, A., and Ahagon, A. 2005. The Newton-Raphson method accelerated by using a line search - comparison between energy functional and residual minimization. *IEEE Transactions on Magnetics*, vol. 41, no. 5, pp. 1724–1727.

Gillott, D. H. and Calvert, J. F. 1965. Eddy current loss in saturated solid magnetic plates, rods, and conductors. *IEEE Transactions on Magnetics*, vol. 1, pp. 126–137.

Green, T. C., Hernandez-Aramburo, C. A., and Smith, A. C. 2003. Losses in grid and inverter supplied induction machine drives. *IEE Proceedings Electric Power Applications*, vol. 150, no. 6, pp. 712–724.

Gyselinck, J. and Dular, P. 2004. A time-domain homogenization technique for laminated iron cores in 3-D finite-element models. *IEEE Transactions on Magnetics*, vol. 40, no. 2, pp. 856–859.

Gyselinck, J. and Lopez-Fernandez, X. M. 2006. Frequency and time domain homogenization of laminated magnetic cores and windings in FE models of high-frequency electromagnetic devices. *COMPEL: The International Journal for Computation and Mathematics in Electrical and Electronic Engineering*, vol. 25, no. 4, pp. 779–791.

Gyselinck, J. J. C., Dupre, L. R. L., Vandevelde, L., and Melkebeek, J. A. A. 1998. Calculation of no-load induction motor core losses using the rate-dependent Preisach model. *IEEE Transactions on Magnetics*, vol. 34, no. 6, pp. 3876–3881.

Gyselinck, J. J. C., Vandevelde, L., Makaveev, D., and Melkebeek, J. A. A. 2000. Calculation of no load losses in an induction motor using an inverse vector Preisach model and an eddy current loss model. *IEEE Transactions on Magnetics*, vol. 36, no. 4, pp. 856–860.

Gyselinck, J., Sabariego, R. V., and Dular, P. 2006. A nonlinear time-domain homogenization technique for laminated iron cores in three-dimensional finite-element models. *IEEE Transactions on Magnetics*, vol. 42, no. 4, pp. 763–766.

Gyselinck, J., Vandevelde, L., Melkebeek, J., Dular, P., Henrotte, F., and Legros, W. 1999. Calculation of eddy currents and associated losses in electrical steel laminations. *IEEE Transactions on Magnetics*, vol. 35, no. 3, pp. 1191–1194.

Henrotte, F., Nicolet, A., Delince, F., Genon, A., and Legros, P. W. 1992. Modeling of ferromagnetic materials in 2D finite element problems using Preisach's model. *IEEE Transactions on Magnetics*, vol. 28, no. 5, pt. 2, pp. 2614–2616.

Hildebrand, E. N. and Roehrdanz, H. 2001. Losses in three-phase induction machines fed by PWM converter. *IEEE Transactions on Energy Conversion*, vol. 16, no. 3, pp. 228–233.

Hollaus, K. and Biro, O. 2000. A FEM formulation to treat 3D eddy currents in laminations. *IEEE Transactions on Magnetics*, vol. 36, no. 4, pp. 1289–1292.

Hollaus, K. and Biro, O. 2002. Derivation of a complex permeability from the Preisach model. *IEEE Transactions on Magnetics*, vol. 38, no. 2, pp. 905–908.

IEEE standard test procedure for polyphase induction motors and generators. IEEE Std 112-1996.

Islam, M. J. 2010. Finite-element analysis of eddy currents in the form-wound multiconductor windings of electrical machines. Ph.D. thesis, Aalto University, School of Science and Technology, Finland, 70 p., available online:
http://lib.tkk.fi/Diss/2010/isbn9789522482556/

Jagiela, M., Bumby, J., and Spooner, E. 2010. Time-domain and frequency-domain finite element models of a solid-rotor induction/hysteresis motor. *IET Electric Power Applications*, vol. 4, no. 3, pp. 185–197.

Janicke, L. and Kost, A. 1998. Convergence Properties of the Newton-Raphson Method for Nonlinear Problems. *IEEE Transactions on Magnetics*, vol. 34, no. 5, pp. 2505–2508.

Jiles, D. C. 1994. Modelling the effects of eddy current losses on frequency dependent hysteresis in electrically conducting media. *IEEE Transactions on Magnetics*, vol. 30, no. 6, pp. 4326–4328.

Jiles, D. C. and Atherton, D. 1984. Theory of ferromagnetic hysteresis. *Journal of Applied Physics*, vol. 55, no. 6, pp.2115–2120.

Kanerva, S. 2005. Simulation of Electrical Machines, Circuits and Control Systems Using Finite Element Method and System Simulator. Ph.D. thesis, Helsinki University of Technology, Finland, 92 p., available online:
http://lib.tkk.fi/Diss/2005/isbn9512276100/

Kawase, Y., Yamaguchi, T., Sano, S., Igata, M., Ida, K., and Yamagiwa, A. 2003. 3-D eddy current analysis in a silicon steel sheet of an interior permanent magnet motor. *IEEE Transactions on Magnetics*, vol. 39, no. 3, pp. 1448–1451.

Lammeraner, J. and Stafl, M. 1966. Eddy Currents. London, U.K., ILIFFE Books Ltd., 233 p.

Lee, J. J., Kim, Y. K., and Nam, H. 2004. Loss distribution of three-phase induction motor fed by pulsewidth-modulated inverter. *IEEE Transactions on Magnetics*, vol. 40, no. 2, pp. 762–765.

Leite, J. V., Benabou, A., Sadowski, N., Clenet, S., Bastos, J. P. A., and Piriou, F. 2008. Implementation of an Anisotropic Vector Hysteresis Model in a 3-D Finite-Element Code. *IEEE Transactions on Magnetics*, vol. 44, no. 6, pp. 918–921.

Leonard, P. J., Marketos, P., Moses, A. J., and Lu, M. 2006. Iron losses under PWM excitation using a dynamic hysteresis model and finite elements. *IEEE Transactions on Magnetics*, vol. 42, no. 4, pp. 907–910.

Luomi, J., Niemenmaa, A., and Arkkio, A. 1986. On the Use of Effective Reluctivities in Magnetic Field Analysis of Induction Motors fed from a Sinusoidal Voltage Source. *Proceedings of the International Conference on Electrical Machines*, München, Germany, vol. 2, pp. 706–709.

Marketos, P., Hall, J. P., and Zirka, S. E. 2008. Power Loss Measurement and Prediction of Soft Magnetic Powder Composites Magnetized Under Sinusoidal and Nonsinusoidal Excitation. *IEEE Transactions on Magnetics*, vol. 44, no. 11, pp. 3847–3850.

Matsuo, T., Osaka, Y., and Shimasaki, M. 2000. Eddy-current analysis using vector hysteresis models with play and stop hysterons. *IEEE Transactions on Magnetics*, vol. 36, no. 4, pp. 1172–1177.

Mayergoyz, I. 2003. Mathematical Models of Hysteresis and their Applications. Second Edition, USA, Academic Press, 498 p.

Mayergoyz, I. D. 1991. Mathematical Models of Hysteresis. New York, Springer-Verlag, 207 p.

Mayergoyz, I. D. 1998. On rotational eddy current losses in steel laminations. *IEEE Transactions on Magnetics*, vol. 34, no. 4, pp. 1228–1230.

Mayergoyz, I. D. and Abdel-Kader, F. M. 1984. The analytical calculation of eddy current losses in steel laminations subjected to rotating magnetic fields. *IEEE Transactions on Magnetics*, vol. MAG-20, no. 5, pp. 2007–2009.

Moses, A. J. and Shirkoohi, G. 1987. Iron loss in non-oriented electrical steels under distorted flux conditions. *IEEE Transactions on Magnetics*, vol. 23, no. 5, pp. 3217–3220.

Muramatsu, K., Okitsu, T., Fujitsu, H., and Shimanoe, F. 2004. Method of nonlinear magnetic field analysis taking into account eddy current in laminated core. *IEEE Transactions on Magnetics*, vol. 40, no. 2, pp. 896–899.

Niemenmaa, A. 1988. Complex reluctivity modelling of iron losses in induction machines. *Proceedings of the International Conference on Electrical Machines*, Pisa, Italy, vol. 1, pp. 633–636.

O'Kelly, D. 1972. Flux penetration in a ferromagnetic material including hysteresis and eddy-current effects. *Journal of Physics D: Applied Physics*, vol. 5, no. 1, pp. 203–213.

Philips, D. A. and Dupré, L. R. 1996. Macroscopic fields in ferromagnetic laminations taking into account hysteresis and eddy current effects. *Journal of Magnetism and Magnetic Materials*, vol. 160, pp. 5–10.

Philips, D. A., Dupré, L. R., and Melkebeek, J. A. A. 1994. Magneto-dynamic field computation using a rate-dependent Preisach model. *IEEE Transactions on Magnetics*, vol. 30, no. 6, pp. 4377–4379.

Pippuri, J. and Arkkio, A. 2008. Challenges in the segregation of losses in cage induction machines. *Proceedings of the 18th International Conference on Electrical Machines*, Vilamoura, Portugal.

Pippuri, J. and Arkkio, A. 2009. Time-harmonic induction-machine model including hysteresis and eddy currents in steel laminations. *IEEE Transactions on Magnetics*, vol. 45, no. 7, pp. 2981–2989.

Potter, R. and Schmulian, R. J. 1971. Self-consistently computed magnetization patterns in thin magnetic recording media. *Journal of Magnetism and Magnetic Material*, vol. MAG-11, no. 3, pp. 934–941.

Preis, K., Biro, O., and Ticar, I. 2005. FEM analysis of eddy current losses in nonlinear laminated iron cores. *IEEE Transactions on Magnetics*, vol. 41, no. 5, pp. 1412–1415.

Preisach, F. 1935. Über die magnetische nachwirkung. Zeitschrift für Physik, vol. 94, pp. 277–302.

Ragusa, C. and Repetto, M. 2000. Accurate analysis of magnetic devices with anisotropic vector hysteresis. *Physica B: Condensed Matter*, vol. 275, nos. 1–3, pp. 92–98.

Rasilo, P. and Arkkio, A. 2010. Modeling the effect of inverter supply on eddy-current losses in synchronous machines. *Proceedings of the 20th International Symposium on Power Electronics Electrical Drives Automation and Motion (SPEEDAM)*, pp. 861–865.

Repo, A.-K. and Arkkio, A. 2006. Numerical impulse response test to estimate circuit-model parameters for induction machines. *IEE Proceedings Electric Power Applications*, vol. 153, no. 6, pp. 883–890.

Righi, L. A., Sadowski, N., Carlson, R., Bastos, J. P. A., and Batistela, N. J. 2001. A new approach for iron losses calculation in voltage fed time stepping finite elements. *IEEE Transactions on Magnetics*, vol. 37, no. 5, pp. 3353–3356.

Rouve, L.-L., Ossart, F., Waeckerle, T., and Kedous-Lebouc, A. 1996. Magnetic flux and losses computation in electrical laminations. *IEEE Transactions on Magnetics*, vol. 32, no. 5, pp. 4219–4221.

Sadowski, N., Batistela, N. J., Bastos, J. P. A., and Lajoie-Mazenc, M. 2002. An inverse Jiles-Atherton model to take into account hysteresis in time-stepping finite-element calculations. *IEEE Transactions on Magnetics*, vol. 38, no. 2, pp. 797–800.

Sadowski, N., Lajoie-Mazenc, M., Bastos, J. P. A., Ferreira da Luz, M. V., and Kuo-Peng, P. 2000. Evaluation and analysis of iron losses in electrical machines using the rain-flow method. *IEEE Transactions on Magnetics*, vol. 36, no. 4, pp. 1923–1926.

Sagarduy, J., Moses, A. J., and Anayi, F. J. 2006. Current losses in electrical steels subjected to matrix and classical PWM excitation waveforms. *IEEE Transactions on Magnetics*, vol. 42, no. 10, pp. 2818–2820.

Saitz, J. 2001. Magnetic Field Analysis of Electric Machines Taking Ferromagnetic Hysteresis into Account. Ph.D. thesis, Helsinki University of Technology, Finland, 123 p., available online: http://lib.tkk.fi/Diss/2001/isbn9512256908/

Serpico, C., Visone, C., Mayergoyz, I. D., Basso, V., and Miano, G. 2000. Eddy current losses in ferromagnetic laminations. *Journal of Applied Physics*, vol. 87, no. 9, pp. 6923–6925.

Silva, V. C., Meunier, G., and Foggia, A. 1995. A 3-D finite-element computation of eddy currents and losses in laminated iron cores allowing for electric and magnetic anisotropy. *IEEE Transactions on Magnetics*, vol. 31, no. 3, pp. 2139–2141.

Stewart, K. H. 1950. Losses in electrical sheet steel. *Proceedings of the IEE - Part II: Power Engineering*, vol. 97, no. 56, pp. 121–125.

Stillesjö, F., Engdahl, G., and Bergqvist, A. 1998. A design technique for magnetostrictive actuators with laminated active material. *IEEE Transactions on Magnetics*, vol. 34, no. 4, pp. 2141–2143.

Štumberger, B., Gorican, V., Štumberger, G., Hamler, A., Trlep, M., and Jesenik, M. 2003. Accuracy of iron loss calculation in electrical machines by using different iron loss models. *Journal of Magnetism and Magnetic Materials*, vols. 254–255, pp. 269–271.

Tsukerman, I. 1995. A stability paradox for time-stepping schemes in coupled field-circuit problems. *IEEE Transactions on Magnetics*, vol. 31, no. 3, pp. 1857–1860.

Tumanski, S. 2003. Investigations of the anisotropic behaviour of SiFe steel. *Journal of Magnetism and Magnetic Materials*, vols. 254–255, pp. 50–53.

Vogt, K. 1983. Elektrische Maschinen. 3rd Edition, Berlin, VEB Verlag Technik, 500 p. (in German)

Yamazaki, K. 2001a. Efficiency analysis of induction motor considering rotor and stator surface loss caused by rotor movement. *Proceedings of the 10th International Symposium on Applied Electromagnetics and Machines*, pp. 107–108.

Yamazaki, K. 2001b. Harmonic copper and iron losses calculation of induction motor using nonlinear time-stepping finite element method. *IEEE International Electric Machines and Drives Conference, 2001*, pp. 551–553.

Yamazaki, K. and Fukushima, N. 2010. Iron loss model for rotating machines using direct eddy current analysis in electrical steel sheets. *IEEE Transactions on Energy Conversion*, vol. PP, no. 99, pp. 1–9.

Yamazaki, K. and Seto, Y. 2006. Iron loss analysis of interior permanent-magnet synchronous motors-variation of main loss factors due to driving condition. *IEEE Transactions on Industry Applications*, vol. 42, no. 4, pp. 1045–1052.

Zirka, S. E. and Moroz, Y. I. 1999. Hysteresis Modeling Based on Similarity. *IEEE Transactions on Magnetics*, vol. 35, no. 4, pp. 2090–2096.

Zirka, S. E., Moroz, Y. I., Marketos, P., and Moses, A. J. 2002. Modelling losses in electrical steel laminations. *IEE Proceedings Science, Measurement and Technology*, vol. 149, no. 5, pp. 218–221.

Zirka, S. E., Moroz, Y. I., Marketos, P., and Moses, A. J. 2004. Dynamic hysteresis modeling. *Physica B: Condensed Matter*, vol. 343, nos. 1–4, pp. 90–95.

Zirka, S. E., Moroz, Y. I., Marketos, P., and Moses, A. J. 2005. A viscous-type dynamic hysteresis model as a tool for loss separation in conducting ferromagnetic laminations. *IEEE Transactions on Magnetics*, vol. 41 no. 3, pp. 1109–1111.

Zirka, S. E., Moroz, Y. I., Marketos, P., and Moses, A. J. 2006. Viscosity-based magnetodynamic model of soft magnetic materials. *IEEE Transactions on Magnetics*, vol. 42, no. 9, pp. 2121–2132.

Zirka, S. E., Moroz, Y. I., Marketos, P., and Moses, A. J. 2010. Loss Separation in Nonoriented Electrical Steels. *IEEE Transactions on Magnetics*, vol. 46, no. 2, pp. 286–289.

Zirka, S. E., Moroz, Y. I., Marketos, P., Moses, A. J., and Jiles, D. C. 2008b. Viscous Behavior of Ferromagnets in the Voltage and Current Driven Regimes. *IEEE Transactions on Magnetics*, vol. 44, no. 11, pp. 3189–3192.

Zirka, S. E., Moroz, Y. I., Marketos, P., Moses, A. J., Jiles, D. C., and Matsuo, T. 2008a. Generalization of the classical method for calculating dynamic hysteresis loops in grain-oriented electrical steels. *IEEE Transactions on Magnetics*, vol. 44, no. 9, pp. 2113–2126.

ISBN 978-952-60-3425-6
ISBN 978-952-60-3426-3 (PDF)
ISSN 1795-2239
ISSN 1795-4584 (PDF)